High-Redshift Blazars Observed by the International LOFAR Telescope

Dissertation zur Erlangung des
naturwissenschaftlichen Doktorgrades
der Julius-Maximilians-Universität Würzburg

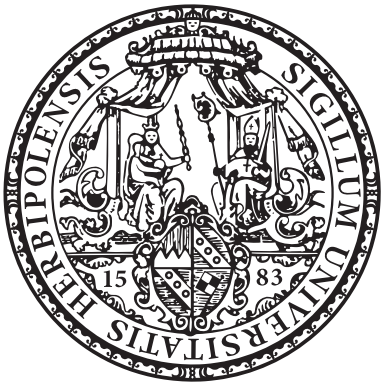

vorgelegt von

Alexander Kappes

aus Alma-Ata

Würzburg, 2023

Eingereicht am: 05.09.2023
bei der Fakultät für Physik und Astronomie

1. Gutachter: Prof. Dr. Matthias Kadler
2. Gutachter: Prof. Dr. Marcus Brüggen
der Dissertation.

Vorsitzende(r): Prof. Dr. Vladimir Dyakonov

1. Prüfer: Prof. Dr. Matthias Kadler
2. Prüfer: Prof. Dr. Marcus Brüggen
3. Prüfer: Prof. Dr. Raimund Ströhmer
im Promotionskolloquium.

Tag des Promotionskolloquiums: 08.05.2024
Doktorurkunde ausgehändigt am:

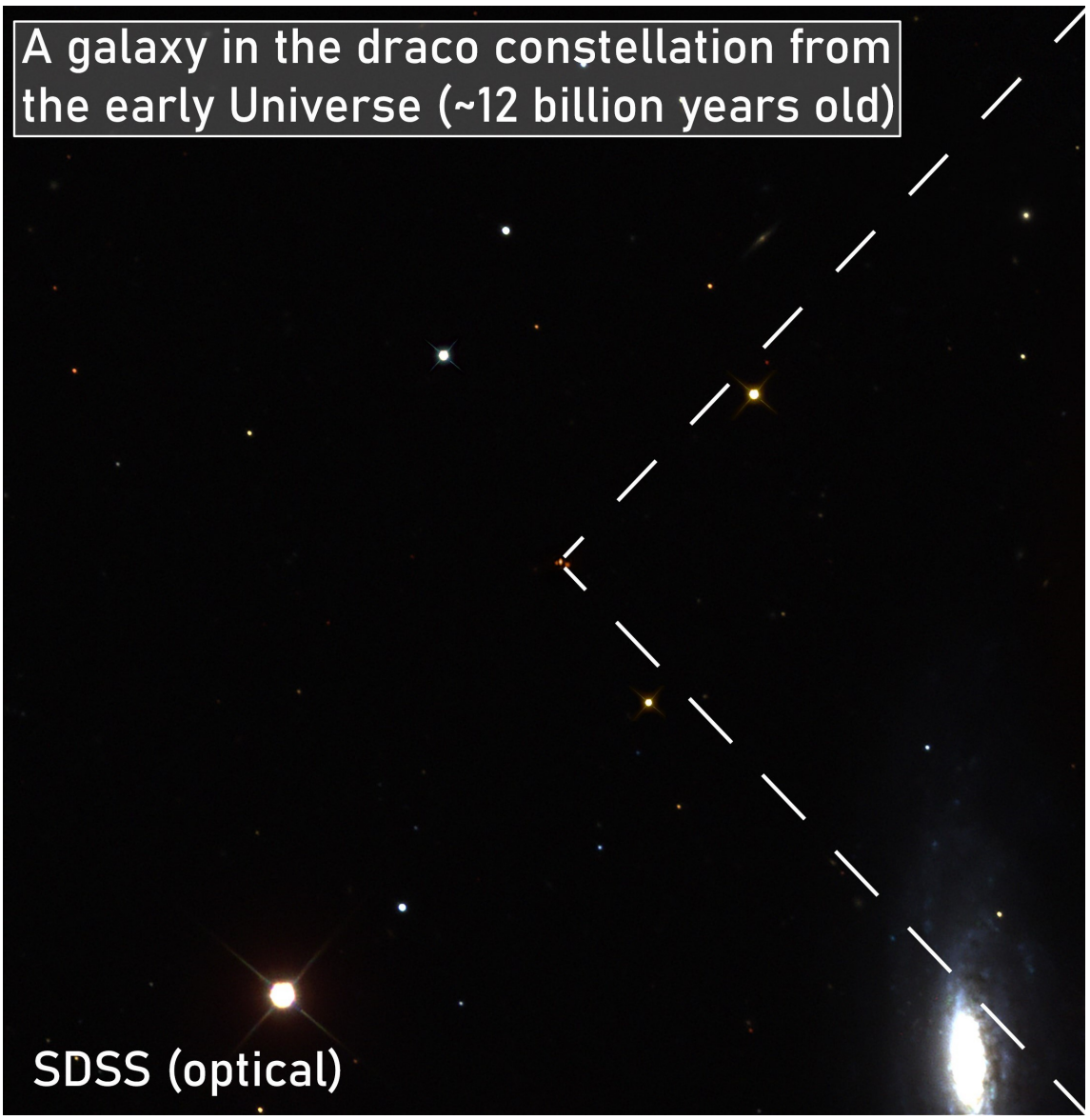

Figure 0.1

On the left, Figure 0.1 shows the relative size and position of the **I**nternational **L**OFAR **T**elescope (ILT) observation of the high redshift blazar GB 1508+5714 with respect to the high resolution **S**loan **D**igital **S**ky **S**urvey (SDSS) image obtained in the optical regime. The data (Kappes et al. 2022) of the ILT observation is shown on the right, in figure 0.2 at a suitable scale. This montage demonstrates the impressive resolution capabilities of the ILT, despite observations performed at long wavelengths.

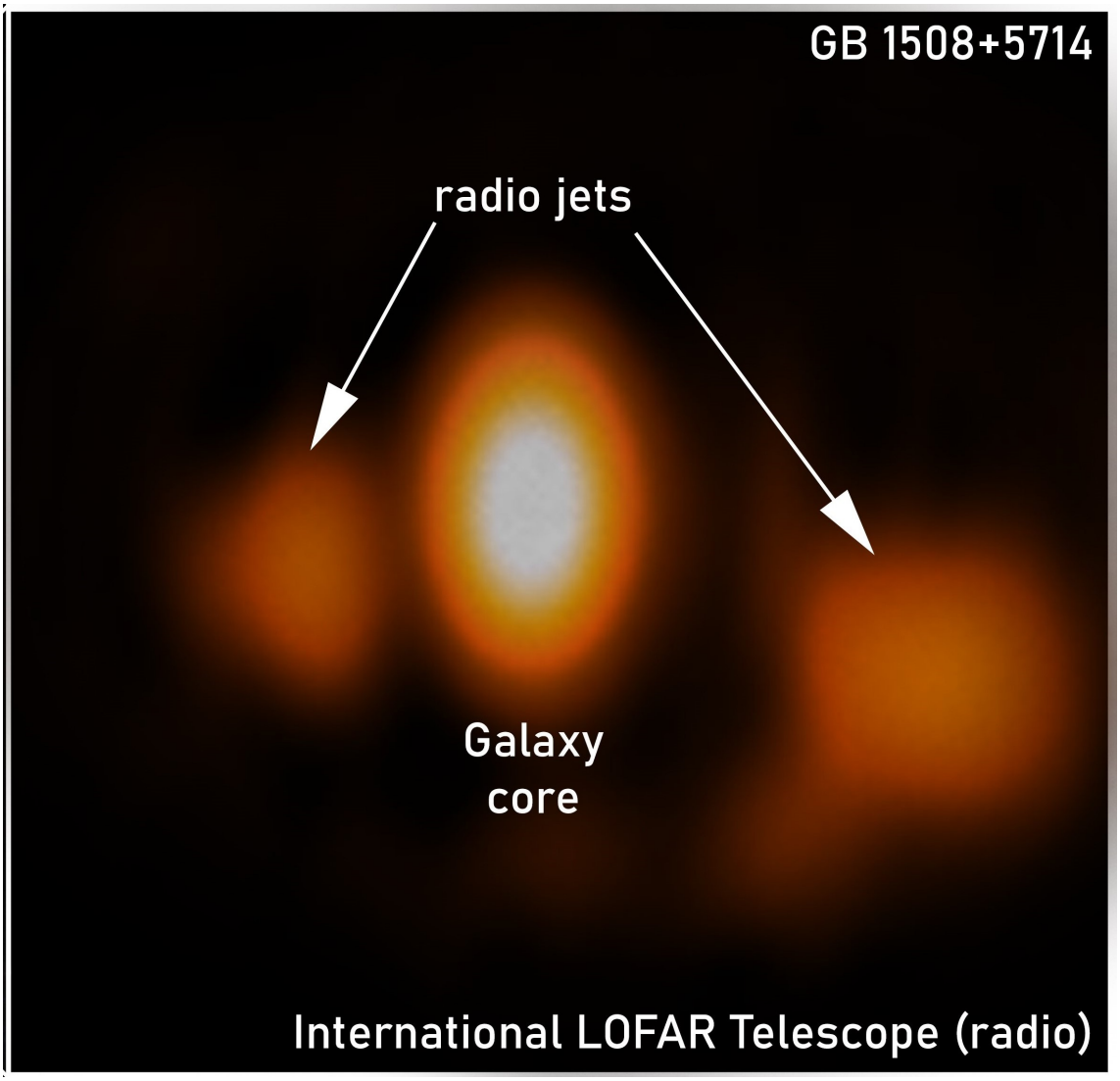
GB 1508+5714
radio jets
Galaxy
core
International LOFAR Telescope (radio)

Figure 0.2

”Look around.
Look at what we have. Beauty is everywhere
– you only have to look to see it.”

Bob Ross, American painter and creator of The Joy of Painting

Abstract

This work presents the first ILT observations of high redshift blazars and their study in terms of jet evolution, morphology, and interaction with the surrounding medium. Each of these represents a highly topical area of astronomy with a large number of open questions. To better understand **A**ctive **G**alactic **N**uclei (AGN) and their fundamental inner workings, new techniques are needed to exploit the full potential of the next generation of radio interferometers. Some of these tools are presented here and applied to one of the latest generation of software radio telescopes. A major focus of the studies presented is on the unification model, where the observed blazars are discussed for their properties to be rotated counterparts of **F**anaroff-**R**iley Class II (FR-II) radio galaxies, when classified as **F**lat **S**pectrum **R**adio **Q**uasars (FSRQs). In addition, multi-wavelength information has been included in the analysis. Both studies are feasibility studies that will serve as a basis for future similar studies. The characteristics discussed and their interpretation do not allow conclusions to be drawn for their respective populations. However, by applying them to a larger number of targets, population studies will be possible.

The first chapters introduce the necessary topics, AGN, principles of radio observations and ILT, in the necessary depth to provide the reader with a solid knowledge base. They are particularly important for understanding the current limits and influences of uncertainties in the observation, calibration and imaging process. But they also shed light on realistic future improvements. A particular focus is on the development and evolution of the **LO**w-**F**requency **AR**ray (LOFAR)-**V**ery **L**ong **B**aseline **I**nterferometry (VLBI) pipeline.

With the tools at hand, the first study addresses the high redshift blazar S5 0836+710 (z=2.218), which has been observed at various wavelengths and resolutions. It has a disrupted one-sided jet with an associated extended region further out. Despite the excellent wavelength coverage, only the additional ILT observations provided a complete picture of the source. With the data, the extended region could be classified as a hotspot moving at slightly relativistic speeds. With the ILT data it was also possible to extract the flux of the core region of the AGN, and in projection to reveal the mixed counter-hotspot behind it. This also allowed constraints on jet parameters and

environmental properties to be modelled, which were previously inconclusive. Technically, this study shows that the ILT can be used as an effective VLBI array for compact sources with small angular scales. However, the detection of faint components beyond redshifts of $z = 2$ may require the capabilities of the **S**quare **K**ilometre **A**rray (SKA) to provide a significant number of detections to enable statistical conclusions.
The second study uses a much improved calibration pipeline to analyse the high redshift blazar GB 1508+5714 (z=4.30). The ILT data revealed a previously unseen component in the eastern direction. A spectral index map was generated from the Karl G. Jansky **V**ery **L**arge **A**rray (VLA) data, showing spectral index values of $-1.2^{+0.4}_{-0.2}$ for the western component, steeper than -1.1 for the eastern region, and 0.023 ± 0.007 for the core. Using the information provided by the ILT observation, as well as multi-wavelength information from other observations ranging from the long radio wavelengths to the γ regime, four models were developed to interpret the observed flux with different emission origins. This also allowed to test a proposed interaction channel of the electrons provided by the jet, to cool off via inverse compton scattering with the **C**osmic **M**icrowave **B**ackground (CMB) photons, rather than by the usual synchrotron emission. This is referred to as cmb quenching in the literature, which could be shown in the study, to be necessary in any case. Finally, one of the four models was considered in which the hotspots in the detected components are unresolved and mixed by the lobe emission, with the X-ray emission coming from the lobes and partially mixed by the bright core region. The results of this preferred model are consistent with hotspots in a state of equipartition and lobes almost so. The study shows that high redshift blazars can be studied with the ILT, and expanding the sample of high redshift blazars resolved at multiple frequencies will allow a statistical study of the population.
Finally, this work successfully demonstrates the powerful capabilities of the ILT to address questions that were previously inaccessible. The current state of the LOFAR-VLBI pipeline, when properly executed, allows work on the most challenging objects and will only improve in the future. In particular, this gives a glimpse of the possibilities that SKA will bring to astronomy.

Zusammenfassung

In dieser Arbeit werden die ersten Beobachtungen von Blazaren mit hoher Rotverschiebung, sowie ihre Untersuchung im Hinblick auf die Jet-Entwicklung, die Morphologie und die Wechselwirkung mit dem umgebenden Medium vorgestellt. Jeder dieser Bereiche stellt ein hochaktuelles Gebiet der Astronomie, mit einer großen Anzahl offener Fragen, dar. Um **A**ctive **G**alactic **N**uclei (AGN) und ihr fundamentales Innenleben besser zu verstehen, sind neue Techniken erforderlich, um das volle Potenzial der nächsten Generation von Radiointerferometern auszuschöpfen. Einige dieser Werkzeuge werden hier vorgestellt und auf ein Teleskop der neuesten Generation von Software-Radioteleskopen angewandt. Ein Hauptaugenmerk der vorgestellten Studien liegt auf dem "Unification Model", bei dem die beobachteten Blazare auf ihre Eigenschaften als rotierte Gegenstücke von **F**anaroff-**R**iley Class II (FR-II)-Radiogalaxien untersucht werden, wenn sie als **F**lat **S**pectrum **R**adio **Q**uasars (FSRQs) klassifiziert werden. Darüber hinaus wurden Informationen über mehrere Wellenlängen in die Analyse einbezogen. Bei beiden Studien handelt es sich um Machbarkeitsstudien, die als Grundlage für künftige ähnliche Studien dienen werden. Die erörterten Merkmale und ihre Interpretation lassen keine Schlussfolgerungen für die jeweiligen Populationen zu. Erst durch die Anwendung auf eine größere Anzahl von Objekten werden Populationsstudien möglich sein.

Die ersten Kapitel führen in die notwendigen Themen, AGN, Prinzipien der Radiobeobachtung und das **I**nternational **L**OFAR **T**elescope (ILT), in der notwendigen Tiefe ein, um dem Leser eine solide Wissensbasis zu vermitteln. Sie sind besonders wichtig, um die aktuellen Grenzen und Einflüsse von Unsicherheiten im Beobachtungs-, Kalibrierungs- und Abbildungsprozess zu verstehen. Sie geben aber auch Aufschluss über realistische zukünftige Verbesserungen. Ein besonderer Schwerpunkt liegt auf der Entwicklung und Weiterentwicklung der **LO**w-**F**requency **AR**ray (LOFAR)-**V**ery **L**ong **B**aseline **I**nterferometry (VLBI)-Pipeline.

Mit den zur Verfügung stehenden Werkzeugen befasst sich die erste Studie mit dem hochrotverschobenen Blazar S5 0836+710 (z=2.218), der bei verschiedenen Wellenlängen und Auflösungen beobachtet wurde. Er hat einen unterbrochenen einseitigen Jet mit einer damit verbundenen ausgedehnten Region weiter außen. Trotz der hervorragenden Wellenlängenabdeckung ermöglichten erst die zusätzlichen Beobachtungen durch das ILT ein vollständiges Bild der Quelle. Mit den Daten konnte die ausgedehnte

Region als Hotspot klassifiziert werden, der sich mit leicht relativistischen Geschwindigkeiten bewegt. Mit den ILT-Daten war es auch möglich, den Fluss der Kernregion des AGN zu extrahieren und in der Projektion den Hotspot des gegenläufigen Jets dahinter aufzudecken. Dies ermöglichte auch die Modellierung von Jet-Parametern und Umgebungseigenschaften, die zuvor nicht zugänglich waren. Technisch gesehen zeigt diese Studie insbesondere, dass das ILT als VLBI-Array für kompakte Quellen mit kleinen Winkelskalen effektiv verwendet werden kann. Die Entdeckung schwacher Komponenten jenseits von Rotverschiebungen von $z = 2$ könnte jedoch das **S**quare **K**ilometre **A**rray (SKA) erfordern, um eine signifikante Anzahl von Entdeckungen zu liefern, welche statistische Schlussfolgerungen zulassen.
Die zweite Studie verwendet eine stark verbesserte Kalibrierungspipeline, um den hoch rotverschobenen Blazar GB 1508+5714 (z=4.30) zu analysieren. Die ILT-Daten enthüllten eine bisher nicht gesehene Komponente in östlicher Richtung. Mit den Karl G. Jansky **V**ery **L**arge **A**rray (VLA)-Daten wurde eine Spektralindexkarte erstellt, die Spektralindexwerte von $-1,2^{+0,4}_{-0,2}$ für die westliche Komponente, steiler als $-1,1$ für die östliche Region und $0,023 \pm 0,007$ für den Kern zeigt. Anhand der von der ILT-Beobachtung gelieferten Informationen sowie von Multi-Wellenlängen-Informationen aus anderen Beobachtungen, die von den langen Radiowellenlängen bis zum γ-Bereich reichen, wurden vier Modelle entwickelt, um den beobachteten Fluss mit unterschiedlichen Emissionsquellen zu interpretieren. Dies ermöglichte es auch, einen vorgeschlagenen Wechselwirkungskanal der Elektronen, welche durch den Jet bereitgestellt werden, zu testen, um sich durch inverse Compton-Streuung mit den Photonen der kosmischen Hintergrundstrahlung abzukühlen, anstatt durch die übliche Synchrotronemission. Dies wird in der Literatur als "CMB- Quenching" bezeichnet, welches in der Studie, als in jedem Fall notwendig, nachgewiesen werden konnte. Schließlich wurde eines der vier Modelle in Betracht gezogen, bei dem die Hotspots in den nachgewiesenen Komponenten unaufgelöst sind und durch die Lobe-Emission vermischt werden, wobei die Röntgenemission von den Lobes stammt und teilweise durch die helle Kernregion vermischt wird. Die Ergebnisse dieses bevorzugten Modells zeigen, dass sich die Hotspots und Lobes nahezu in einem Zustand der Äquipartition befinden. Die Studie zeigt somit, dass Blazare mit hoher Rotverschiebung mit dem ILT untersucht werden können, und die Hinzunahme von weiteren Blazaren mit hoher Rotverschiebung, die mit mehreren Frequenzen aufgelöst wurden, eine statistische Untersuchung der Population ermöglichen werden.
Schließlich demonstriert diese Arbeit erfolgreich die leistungsstarken Fähigkeiten des ILT, um Fragen anzugehen, die zuvor unzugänglich waren. Der derzeitige Stand der LOFAR-VLBI-Pipeline ermöglicht bei ordnungsgemäßer Ausführung die Arbeit an den

anspruchsvollsten Objekten und wird sich in Zukunft noch weiter verbessern. Dies gibt insbesondere einen Einblick in die Möglichkeiten, die das SKA der Astronomie bieten wird.

Contents

Abstract I

Zusammenfassung III

1 Scientific Background 1

1.1 The AGN Unification Model . . . 2
1.2 Distant (Radio) Galaxies . . . 7
1.2.1 Relativistic Doppler Boosting . . . 7
1.2.2 Differential Relativistic Doppler Boosting . . . 9
1.2.3 Depression of Distant Radio Galaxies . . . 9
1.3 CMB Quenching Mechanism . . . 10
1.3.1 Emission Models . . . 11
1.3.2 Model Example: GB 1508+5714 . . . 14

2 Principles of Radio Observations 17

2.1 Photon Fluxes . . . 17
2.2 Antenna Temperature . . . 18
2.3 Single Dish Radio Telescopes . . . 18
2.4 Multi Dish Radio Arrays . . . 23
2.4.1 Fourier Optics . . . 23
2.4.2 Interferometry . . . 30
2.4.3 Aperture Synthesis by Radio Interferometric Arrays . . . 43
2.4.4 Image Reconstruction . . . 57
2.4.5 Digital Beamforming . . . 64

3 The International LOFAR Telescope 73

3.1 The Low Band Antenna . . . 75
3.2 The High Band Antenna . . . 78
3.3 Low Frequency Challenges with LOFAR . . . 79
3.4 Big Data Challenges . . . 82
3.4.1 Data Acquisition . . . 83
3.4.2 Data Storage . . . 83

3.4.3 Data Processing 84
3.5 LOFAR-VLBI Data Calibration and Processing 85
3.5.1 Calibration Strategy for LOFAR-VLBI 86
3.5.2 LOFAR-VLBI Pre-Processing 88
3.5.3 LOFAR-VLBI Pipeline 90
3.5.4 Post-Pipeline Steps 94
3.5.5 Future Work 94

4 Resulting First Studies by the ILT **97**
4.1 Studies of S5 0836+710 97
4.1.1 Scientific Interest 98
4.1.2 Previous Studies 99
4.1.3 Observation and Data Reduction 100
4.1.4 Results 102
4.1.5 Discussion 104
4.1.6 Conclusion 112
4.2 Studies of GB 1508+5714 113
4.2.1 Scientific Interest 113
4.2.2 Previous Studies 114
4.2.3 Observation and Data Reduction 115
4.2.4 Results 118
4.2.5 Discussion 124
4.2.6 Conclusion 132

5 Final Remarks and Outlook **135**

Bibliography **145**

6 Appendix **147**
6.1 Refereed Publications 147
6.2 List of Acronyms 151
6.3 Acknowledgements/Danksagung 155

1 Scientific Background

Blazars are a subclass of **A**ctive **G**alactic **N**uclei (AGN) characterised by strong and variable mostly non-thermal emission across the electromagnetic spectrum. They are thought to be powered by accretion onto **S**uper-**M**assive **B**lack **H**oles (SMBHs), with relativistic jets aligned close to our line of sight. In particular, high-redshift blazars are of great interest to astrophysics, as they provide a unique opportunity to study the early universe and the evolution of AGN.

The **I**nternational **L**OFAR **T**elescope (ILT) is a powerful tool for studying high-redshift blazars in the radio regime. **LO**w-**F**requency **AR**ray (LOFAR) is a radio interferometer that operates at low frequencies (10-240 MHz) and has a high angular resolution, making it well suited for studying faint and distant objects. The ILT is an extension of the original LOFAR telescope, which is located in the Netherlands, and consists of additional stations in various European countries.

In this dissertation I will focus on high redshift blazars observed at long wavelengths in the radio regime with the ILT. I present the results of two studies of individually selected high-redshift blazars, including their radio properties, such as their flux densities, spectra, and so on. I also investigate the relationship between these properties and the redshifts of the blazars, and examine any correlations with other properties such as their optical and X-ray properties. The studies aim to provide new insights into the nature and evolution of high-redshift blazars, and to contribute to our understanding of the early universe and the growth of supermassive black holes. More importantly, this work demonstrates the feasibility of such studies, which can now be carried out in much larger numbers and are therefore statistically robust.

In addition, this thesis will also discuss the data analysis techniques and methods used to study the high redshift blazars with the ILT. The use of high-resolution radio interferometry with the ILT allows detailed imaging of the radio structures of blazars, which can provide valuable information about the properties of their jets, as well as any diffuse structures and the physical processes taking place within them. This work also dis-

cusses the use of long-wavelength observations to probe the properties of the blazars' environment, such as their host galaxies and the surrounding intergalactic medium.

Finally, the potential of using high-redshift blazars as probes of the early universe will be explored. High-redshift blazars are among the most distant objects known, and their study can shed light on the early stages of galaxy formation and the growth of SMBHs.

In summary, this dissertation aims to present the feasibility of comprehensive studies of high-redshift blazars observed in the radio regime at long wavelengths with the ILT. The results of the presented studies provide new insights into the nature and evolution of the selected blazars, and will contribute to our understanding of the early universe. The high-resolution, long-wavelength capabilities of the ILT will allow many more detailed studies of the properties of such objects and their environments, following the blueprint, presented in this work.

Ultimately, the quest to understand high-redshift blazars through the eyes of the ILT is another step towards unravelling the mysteries of the universe and especially supermassive black holes, which are feeding a sheer bottomless hunger for everything. The results of studies, as presented in this work, allow us to understand the intricate nature and evolutionary patterns of these celestial wonders and their surroundings. Efforts like this are part of a quest that might eventually reveal the grand design of the cosmos and inspire future endeavors to unlock the secrets of the universe.

1.1 The AGN Unification Model

AGN represent a class of objects which are among the most energetic particle accelerators in the universe. They are located (as the name implies) in active galaxies, more precisely in the central region of such active galaxies. In general, galaxies are classified as active when their SMBH, located in this central region, accretes mass and, as a result, emits photons across the electromagnetic spectrum as well as other energetic particles. This region is astonishingly small (on the order of our solar system) compared to the immense size of a galaxy, yet capable of outshining the entire rest of the host galaxy. The excess of high-energy particles also suggests AGN to be the most likely candidate for high-energy neutrinos (Kadler et al. 2016). Luminosities observed from AGN typically are between $10^{42} \leq {}^{L}/_{\mathrm{erg\,s^{-1}}} \leq 10^{47}$ which is made possible by the accretion process of SMBHs (Shakura & Sunyaev 1973). By this process, the mass of the SMBHs correlates to the luminosity and thus indicates SMBH masses from $10^{7} \leq {}^{M}/_{M_{\odot}} \leq 10^{10}$

(Vestergaard & Peterson 2006; Peterson et al. 2004).

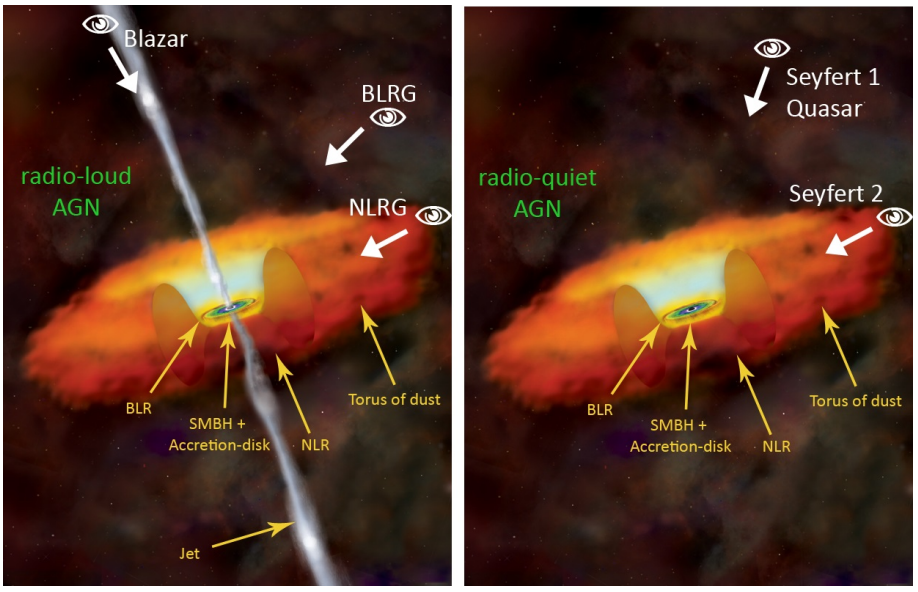

Figure 1.1: Schematic summary of the unification model based on Urry & Padovani (1995). The SMBH in the center is surrounded by the accretion disk and the dust torus. On the left are the radio-loud AGN and on the right the radio-quiet AGN. Different angles for the line of sight result in the respective object class, as indicated by the white arrows. Credit: NASA/CXC/M.Weiss; edited by Jonas Trüstedt.

AGN can launch collimated jets of magnetized relativistic plasma, traversing into space often way further out than the host galaxy is in size (Schoenmakers et al. 2000; de Vries et al. 2006). These jets originate from the SMBH and are generally oriented perpendicular to the accretion disk, which is surrounded by an optically thick torus (see Fig. 1.1). The jets' flow of plasma is fed by the accretion process. While most of the material falls into the black hole, a fraction of it is redirected to form the jets. The nature of the exact process is currently unclear. The jets' emission typically ranges from low-frequency radio to γ-rays (Blandford et al. 2019). Historically, different types of AGN were found and categorized, following different criteria, for example by their *radio loudness* (Kellermann & Pauliny-Toth 1969). With the calculated ratio from the flux in the radio (F_R) at 6 cm wavelength and optical regime (F_O) at 4400 Å, the AGN is classified to be:

$$R = \frac{F_R}{F_O} = \begin{cases} \gtrsim 10 & \rightarrow \text{radio loud} \\ < 1 & \rightarrow \text{radio quiet} \end{cases} . \tag{1.1}$$

The ratio between the values 1 and 10 is considered to be an intermediate loudness. It is worth noting that radio loudness is a first indicator of whether thermal or non-thermal emissions are the dominant processes taking place in an object. The radio emission

usually comes from synchrotron radiation (non-thermal), while the optical emission usually comes from thermal emission.

Radio quiet AGN do not show any radio morphology (compare Fig. 1.1 right side) or a jet and are therefore further categorized based on their luminosity and their optical spectrum. If they exhibit high luminosities, they are referred to as a **Q**uasi **S**tellar **O**bject (QSO), regardless of line widths in the spectrum. Low luminosity objects are designated Seyfert 2 if they have only a spectrum with narrow emission lines and Seyfert 1 if narrow and broad emission lines are found in the spectrum. This work will not highlight radio quiet objects, this is why no further details are necessary at this point. Weedman (1977) and Peterson (1997) provide more information on radio quiet objects.

In contrary to radio quiet AGN, radio loud AGN do show radio morphology (compare Fig. 1.1 left side), powered by the jet. Two favored mechanisms can potentially explain the formation of the jets. One considers the extraction of electromagnetic energy from the rotation energy of the SMBH (Blandford & Znajek 1977), the other describes particle winds from the accretion disc, able to form, contrary to the collimated jets by the first model, broad jets (Blandford & Payne 1982). The jets, while transporting plasma out of the host galaxy, lose energy on the way, mostly due to radiation and expansion. The very frontal region of the jets is impacting the intergalactic medium. While usually extremely thin, shock regions can be observed on larger scales. The morphology can be either classified as a **F**anaroff-**R**iley Class I (FR-I) or **F**anaroff-**R**iley Class II (FR-II), introduced by Fanaroff & Riley (1974). Fig. 1.2 shows Karl G. Jansky **V**ery **L**arge **A**rray; Thompson et al. 1980 (VLA) observations of FR-I and FR-II type radio galaxies, demonstrating the morphological differences.

The FR-I AGN show a broad and bright jet ending in diffuse plumes. The jets are thought to interact with their surroundings quite early after their formation and therefore continuously lose significant amounts of their original energy as they flow into the plumes. For the usual FR-I objects, the radio luminosity in the extended[1] regions is usually below $\log(L^{ext}_{178MHz}[\mathrm{W\,Hz^{-1}}]) \lesssim 25$ (Fanaroff & Riley 1974).
In contrast, FR-II AGN have rather narrow jets that do not dominate the overall luminosity of the object as much as FR-I do. They appear to barely interact with the surrounding medium for a very long distance until they eventually terminate in a reverse jet shock called a hotspot, feeding the surrounding lobe with energetic

[1] Extended in this context means any emission from the source excluding the innermost central region (the core).

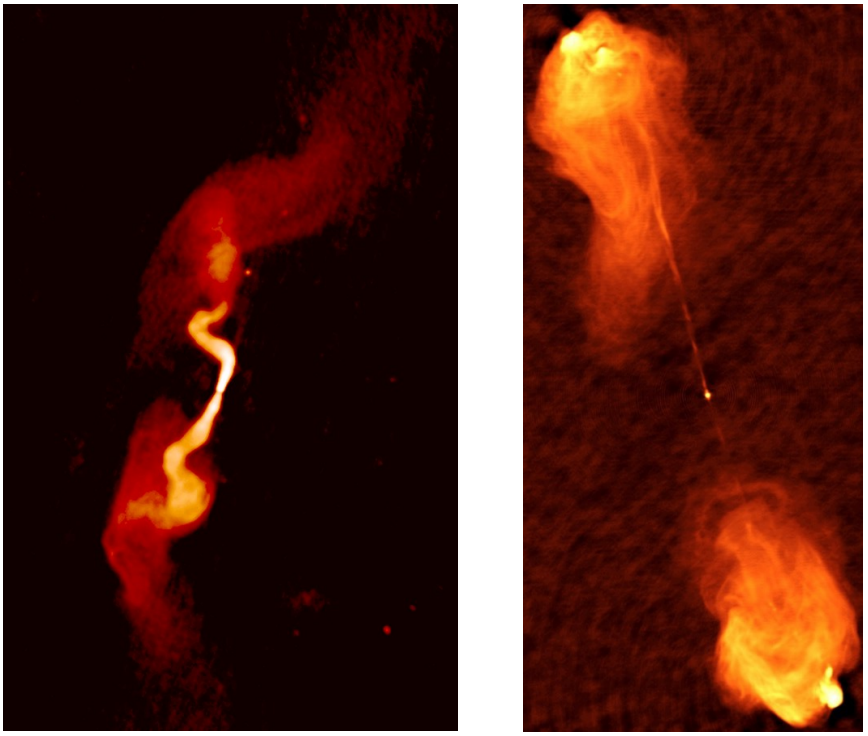

(a) **(b)**

Figure 1.2: VLA observations of the FR-I radio galaxy 3C 31 (a) at 1.4 GHz and the FR-II radio galaxy Cygnus A (b) at 6 GHz. While 3C 31 has the typical bright jet terminating in plumes, Cygnus A has a highly collimated jet with a bright central core terminating in bright hotspots. These feed the surrounding lobes. Image from Lara et al. (1997) and Perley et al. (1984) with image courtesy of NRAO/AUI.

plasma. In general, their extended emission limits them to have luminosities at $\log(L^{ext}_{178MHz}[\mathrm{W\,Hz^{-1}}]) \gtrsim 26$ (Kharb et al. 2010; Cooper et al. 2007). It should be said, however, that there is no clear transition in morphology and intermediate AGN also exist.

Radio-loud AGN with only low inclination are called blazars. They are typically characterized by a compact radio morphology and a flat radio spectrum caused by radiated synchrotron emission. In the case where they are rather intrinsically bright and have strong emission lines, they are referred to as a **F**lat **S**pectrum **R**adio **Q**uasar (FSRQ). If the object is less luminous, has weak or no emission lines, and has a compact morphology, it is classified as a **BL Lac**ertae (BL Lac) object. Here, distance measurements by redshift is not possible due to the lack of spectral lines, so this information is often unavailable.

In accordance with synchrotron theory, electrons with a Lorentz factor γ emit at frequencies $\nu \sim 10^{-6}\gamma^2 B^2$ GHz (where B is measured in mG). Thus, high radio frequency observations are sensitive to emission from electrons with $\gamma > 1000$. The emission spectrum from large-scale AGN components, such as non-beamed lobe emission and

moderately beamed hotspot emission, follows a power law of the form $F_\nu \propto \nu^\alpha$, where the spectral index α typically ranges from -0.5 to -1. On the other hand, the emission from the central jet of blazars is highly beamed and has a flat spectral index of $\alpha \sim 0$. As a result, blazars have been well studied at high radio frequencies, where the jet emission dominates and **V**ery **L**ong **B**aseline **I**nterferometry; Readhead & Wilkinson 1978 (VLBI) techniques provide high angular resolution of the inner jet region (Zensus 1997). However, the low frequency properties of blazar lobe emission have received relatively little attention in recent decades.
Considering the spectra of radio galaxies, further classifications can be made. Some objects have only narrow spectral lines in their spectrum. These may have morphologies of FR-I or FR-II and are called **N**arrow **L**ine **R**adio **G**alaxies (NLRG). If they also emit broad spectral lines and do not have compact but FR-I or FR-II morphologies, they are referred to as **B**road **L**ine **R**adio **G**alaxies (BLRG). An overview with the described properties with respect to the AGN class is presented in Table 1.1

Table 1.1: AGN classes and their properties.

	Type	Emission Lines	Luminosity	Jet	Radio Morphology
Radio quiet	Seyfert 1	broad+narrow	low	none	none
	Seyfert 2	narrow	low	none	none
	QSO	broad+narrow	high	none	none
	QSO	narrow	high	none	none
Radio loud	BLRG	broad+narrow	low	yes	FR-I
	BLRG	broad+narrow	high	yes	FR-II
	NLRG	narrow	low	yes	FR-I
	NLRG	narrow	high	yes	FR-II
	BL Lac	none	low	yes	compact or rotated FR-I
	FSRQ	broad+narrow	high	yes	compact or rotated FR-II

Blue entries indicate rotated versions, according to the AGN unification theory. Credit: Matthias Kadler and edited by Alexander Kappes

According to the AGN unification theory (Antonucci 1993; Urry & Padovani 1995), FSRQs are considered to be the beamed versions of FR-II radio galaxies; whereas BL Lacs are the beamed versions of FR-I radio galaxies as indicated in blue in Table 1.1. Further general information about the AGN unification model and AGN subclasses is provided

in Krolik (1999), Osterbrock & Ferland (2006), Schneider (2008) and Blandford et al. (2019).

1.2 Distant (Radio) Galaxies

As described above, BLRG and NLRG are radio galaxies, that show a radio morphology, categorized as FR-I or FR-II type, depending on their luminosity. Rotating these objects, such that their jet axis is aligned to the line of sight to the observer, their morphology changes, which lets them appear point-like. With a small inclination angle between the line of sight to the observer and the jet axis, the relativistic Doppler boosting has to be accounted for, which increases the observed flux, emitted by highly relativistic plasma moving towards the observer. Thus, the central region (core) of such a point-like structure becomes much brighter in comparison to the surrounding lobe or plume structure around the jet axis, which rather radiates isotropically without significant boosting effects. This effect allows to observe AGN with a small inclination angle even at extreme redshifts.

1.2.1 Relativistic Doppler Boosting

Assuming a simple model of a radio loud AGN with two jets, that are launched from the central region in opposite directions (see Fig. 1.3). Powerful jets will terminate eventually in a hotspot (HS) - from the jet traveling towards the observer - and a counter-hotspots (CHS) - from the jet traveling away from the observer. Note, that the visible length D_{chs} of the counter jet is shorter than the visible length of the jet D_{hs}, oriented towards the observer, because of the different light travel times of photons originating from either the hotspot or counter-hotspot (see Fig. 1.3). The length of the visible counter-jet can be calculated, when assuming similar jet advance speeds for jet and counter-jet. The advance speed of the jet can also be measured by the advance speed of the hotspots $v_{\mathrm{hs}} \simeq v_{\mathrm{chs}}$, as the very tip of the jet. Assuming a constant advance speed over the lifetime (which in reality is not correct, mainly due to penetrating different environments - but nevertheless order of magnitude correct), we can calculate the age of the hotspots, and counter-hotspots as:

$$t_{\mathrm{hs}} \simeq \frac{D_{\mathrm{hs}}}{v_{\mathrm{hs}}};\ t_{\mathrm{chs}} \simeq \frac{D_{\mathrm{chs}}}{v_{\mathrm{hs}}} \tag{1.2}$$

The jet can be seen at an inclination angle θ to the observer. For a perfectly symmetric counter-jet, the inclination angle for the counter-jet would be $180° + \theta$, but when inspecting FR-II-like radio galaxies, commonly there is an asymmetry in orientation,

described by the angle φ, which corrects the inclination angle of the counter-jet to be $180° + \theta - \varphi$. These misalignment angles are known in 3C sources to reach values of up to 12° or more (Leahy & Williams 1984).

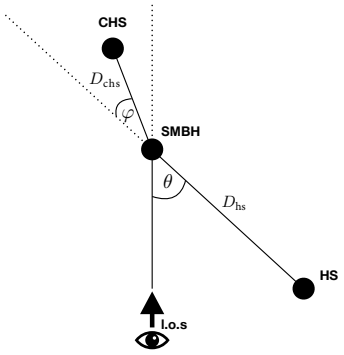

Figure 1.3: Model of a radio loud AGN with asymmetrically oriented linear jets terminating We consider an observation at a small inclination angle θ. HS denotes the hotspots region closer to the observer, and CHS denotes the counter-hotspots region. The different arm lengths are due to the different light travel times. The two jets are misaligned by φ from a straight/symmetric jet/counterjet axis.

The light travel time towards the observer between the core region, hosting the SMBH and the hotspot differs by the time it takes the light to traverse the additional distance $D_{\mathrm{H}} \cdot \cos(\theta)$. But, because the angle $\theta \approx 0$ this reduces to simply D_{H}. The analogue case is true for the CHS. Due to this, the total distance, that needs to be travelled by the photons additionally, coming from the counter-hotspot is

$$D = D_{\mathrm{hs}} + D_{\mathrm{chs}}. \tag{1.3}$$

The visible younger age of the counter-hotspots can thus be calculated as

$$t_{\mathrm{chs}} = t_{\mathrm{hs}} - \frac{D}{c}. \tag{1.4}$$

Combining the equations (1.2), (1.3) and (1.4), we get:

$$\frac{D_{\mathrm{chs}}}{v_{\mathrm{hs}}} = t_{\mathrm{hs}} - \frac{(D_{\mathrm{hs}} + D_{\mathrm{chs}})}{c}, \tag{1.5}$$

and thus for the observed length of the counter-jet:

$$D_{\mathrm{chs}} = \left(\frac{D_{\mathrm{hs}}}{v_{\mathrm{h}}} - \frac{D_{\mathrm{hs}}}{c}\right) \cdot \left(\frac{1}{v_{\mathrm{hs}}} - \frac{1}{c}\right)^{-1}. \tag{1.6}$$

As mentioned before, we observe relativistic plasma, moving with the speed of β (in c) towards us - and in the case of the counter-jet away from us. Here, we expect not only Doppler shifts to be present, but also the relativistic beaming effect or relativistic Doppler boosting. Assuming a moving region of plasma towards the observer, intrinsically having an isotropic radiation across the spectrum, with the flux F_i. The observer measures the flux F_o, coming from the approaching region, with the spectral index α, under the inclination angle θ. Thus the relativistic beaming is described as

$$F_\mathrm{o} = F_\mathrm{i} \cdot \left(\frac{1}{\gamma \cdot (1 - \beta \cos\theta)} \right)^{3-\alpha}, \tag{1.7}$$

with γ as the Lorentz factor

$$\gamma = \frac{1}{\sqrt{1-\beta^2}}. \tag{1.8}$$

The Doppler factor is given by

$$\delta = \frac{1}{\gamma \cdot \left(1 - \beta \cos\theta\right)}. \tag{1.9}$$

1.2.2 Differential Relativistic Doppler Boosting

With the relativistic Doppler boosting introduced in the above section, it is now trivial to formulate a scenario in which two equally bright plasma regions with similar velocities $\beta_1 \approx \beta_2 = \beta$ are ejected in opposite directions (one away from the observer and one toward the observer) at the inclination angle θ. Although they have intrinsically the same brightness, they nevertheless show a different brightness. The approaching region is observed brighter, while the distant region is observed fainter. In the case where the departing region was launched exactly opposite to the approaching region to satisfy conservation of momentum, but was deflected slightly further outward by, for example, a dense cloud, an asymmetry can be introduced described by the angle φ (see Fig. 1.3). This allows the observed flux ratio of the two regions to be formulated as

$$\frac{F_{\mathrm{o},1}}{F_{\mathrm{o},2}} = \left(\frac{1 + \beta \cos\theta}{1 - \beta \cos(\theta - \varphi)} \right)^{3-\alpha}. \tag{1.10}$$

1.2.3 Depression of Distant Radio Galaxies

Radio loud AGN observed at low inclination angles appear remarkably bright because of their Doppler boosting (Cohen et al. 2007b), so they can be observed even at extreme redshifts. The ability to study this population distributed over a wide range of redshifts, and thus over different ages of the universe, provides an observational

tool for cosmological principles (Wang et al. 2021). Their radiation, detectable over a wide range of the **E**lectro**M**agnetic (EM) spectrum, provides many observing windows for different types of telescopes and, as a result, a variety of data to support modeling efforts (multi-wavelength observations). While the depth of information is vast in the frequency regime, the brightness distribution provides usually only little information, because the morphology mostly appears as a point-like object. This emphasizes the importance of modeling attempts, like it is often done for the target's **S**pectral **E**nergy **D**istribution (SED). Here, the observed flux is used to display the product of the energy and spectral energy flux density versus the observed frequency (see e.g. Fig. 1.4). The ability to detect blazars at extreme distances across the EM spectrum provides a unique insight into cosmology, galaxy evolution and in particular the evolution of AGN. (Dunlop & Peacock 1990; Georgakakis et al. 2017). One should also consider the differences in the targets evolutionary stage, the environment in which they are embedded, and their interactions with that environment.

Unlike blazars, AGN with radio jets at a greater angle to the line of sight are more difficult to detect with increasing distance, since the effect of Doppler boosting is largely absent. So far, numerous radio surveys have been performed to study radio AGN populations, (e.g., Becker et al. 1995; Condon 1988; Cohen et al. 2007a; Intema et al. 2017) and most find self-consistent relative number ratios of radio galaxies and blazars up to a redshift of ~ 3 (Volonteri et al. 2011). For greater redshifts, uncertainties about density evolution and the formation of massive black holes in the early universe (Blundell et al. 1999; Shankar et al. 2008) complicate the matter. However, there seems to be a consensus that there is a relative lack of higher redshift radio galaxies, even when evolutionary effects and detection limits are taken into account (e.g., Wu et al. 2017; Hodges-Kluck et al. 2021, and references therein). The reason for this deficit is not yet fully understood.

1.3 CMB Quenching Mechanism

The currently favored explanation, which was discussed for quite some time (e.g., Celotti & Fabian 2004) and further explored by Ghisellini et al. (2014), describes the interaction of the electrons in the extended radio lobes with the **C**osmic **M**icrowave **B**ackground (CMB), attenuating the brightness of the extended radio lobes. In the proposed process, the CMB energy density U_{CMB}, which increases with the redshift $\left(U_{\mathrm{CMB}} \propto (1+z)^4\right)$, dominates over the magnetic energy density U_{B} at very high redshifts, so that the jet electrons interact with the CMB photons through **I**nverse

Compton (IC) scattering and cool, while the synchrotron radiation is suppressed, referred to as CMB quenching. Other studies, e.g., Morabito & Harwood (2018), show evidence that this model agrees by comparing simulations and observational data. If present as it is proposed, the synchrotron radiation is suppressed, but the steep-flanked isotropic radiation of the extended structures is nevertheless detectable by telescopes in the long-wavelength radio range. Radio observations of nearby radio galaxies, show that the luminosity of lobe or plume structures increases with lower frequencies. Depending on the redshift, the quenching by the CMB could easily affect higher frequencies more severely, because they already are less luminous, to begin with. Hence, suitable radio telescopes, providing the necessary resolution capabilities, sensitivity and long observational wavelengths, can test and guide the theoretical models.

1.3.1 Emission Models

This work studies results of ILT observations of high redshift blazars. The CMB quenching mechanism is tested for, following the model descriptions in Ghisellini & Tavecchio (2009); Ghisellini et al. (2014, 2015). For further in-depth information, consider these studies. The following sections will introduce important modeling considerations for the jet emission, the hotspots emission and the lobe emission, allowing to understand the results in this work.

Jet Emission

The total jet power for a relativistic jet is parameterized as (see, e.g., Perucho et al. 2017):

$$L_\mathrm{j} = \left(\rho_\mathrm{j} h_\mathrm{j} \Gamma_\mathrm{j}^2 + \frac{(B^\phi)^2}{4\pi}\right) v_\mathrm{j} A_\mathrm{j}, \tag{1.11}$$

where ρ_j is the jet rest mass density, $h_\mathrm{j} = c^2 + \frac{\gamma_\mathrm{j} P_j}{(\gamma_\mathrm{j}-1)\rho_\mathrm{j}}$ is the jet specific enthalpy, Γ_j is the jet Lorentz factor, B^ϕ is the toroidal field in the observer's frame, v_j is the jet velocity, A_j is the jet cross-section, c is the speed of light, γ_j is the ratio of specific heats of the jet gas, and P_j is the jet pressure. The first term in eq. (1.11) contains the contributions of kinetic energy, internal energy and residual mass energy, while the second term corresponds to the magnetic energy of the jet. For the non-relativistic case eq. (1.11) becomes

$$L_\mathrm{j} = \left(\frac{\gamma_\mathrm{j} P_\mathrm{j}}{\gamma_\mathrm{j} - 1} + \frac{1}{2}\rho_\mathrm{j} v_\mathrm{j}^2 + \frac{(B^\phi)^2}{4\pi}\right) v_\mathrm{j} A_\mathrm{j}. \tag{1.12}$$

The jet emission considers a simple, one-zone, leptonic model, as described in Ghisellini & Tavecchio (2009). In this model, most of the observed radiation is emitted in a single spherical region contained in a conical jet with a semi-opening angle of $\psi = 0.1$ rad. The spherical region is initially located at the distance $R_{\rm ini}$ from the black hole. The sphere is homogeneously filled with a tangled magnetic field B, moving with the velocity β (in c), with a bulk Lorentz factor γ, with the inclination angle θ and the Doppler factor δ. The sphere is fed by relativistic electrons with the constant rate $Q(E)$, with energies E (in $m_{\rm e} \cdot c^2$) with the total comoving power

$$P'_{\rm e} = V \cdot m_{\rm e} \cdot c^2 \int_{E_{\rm min}}^{E_{\rm max}} Q(E) \cdot E \, dE, \tag{1.13}$$

with V as the volume of the sphere and $\rm E_{min}$ and $\rm E_{max}$ as the minimum and maximum injection energies of the electrons, respectively. The electron energy distribution follows

$$Q(E) = Q(0) \frac{\left(\frac{E}{E_{\rm b}}\right)^{-s_1}}{1 + \left(\frac{E}{E_{\rm b}}\right)^{-s_1+s_2}} \ (\rm cm^{-3} s^{-1}), \tag{1.14}$$

with s_1 and s_2 as the power law slopes below and above the break energy $E_{\rm b}$, respectively. Furthermore, a standard, optically thick, geometrically thin accretion disc (Shakura & Sunyaev 1973) with a total luminosity of $L_{\rm d} = 10^{45} \rm erg\, s^{-1}$ is assumed. Additionally, the **B**road **L**ine **R**egion (BLR) is assumed to be re-processing (10 % of $L_{\rm d}$). Further out, a molecular torus intercepts and re-emits a fraction of $L_{\rm d}$ ($\sim 20 - 40$ %) in the infrared band. The model considers emission processes within the jet to be synchrotron, **S**ynchrotron **S**elf-**C**ompton (SSC) and IC of the relativistic electrons scattering off photons produced by the accretion disc, the BLR and the torus. The synchrotron radio emission from the compact source is self-absorbed for up to (observed) frequencies $\sim 10^3$ GHz and thus not accounted for in the modeling. The flat radio spectrum for blazars at lower frequencies is produced by the superposition of the emission from several moving parts of the jet. While this part is not modeled, figures showing modeled SEDs display dashed lines with expected slopes to guide the eye (e.g. see Fig. 1.4).

Hotspot Emission

The hotspots modeling follows Ghisellini et al. (2014). The previously introduced powerful jet, carrying highly relativistic particles into the intergalactic region, eventually depositing the particles' kinetic energy in a termination shock region, described as the hotspots. Those particles are feeding the extended lobe structure.

The emitting electrons experiencing a rather strong magnetic field in the hotspots, remain largely unaffected by the CMB, up to very high redshifts. This can be calculated by comparing the measured magnetic field, as shown for Cygnus A by Wilson et al. (2000) ($B \sim 1.5 \cdot 10^{-4}$ G), with the magnetic field B_{CMB} in equipartition with the CMB energy density U_{CMB} by

$$B_{\mathrm{CMB}} = \sqrt{8\pi U_{\mathrm{CMB}}}, \tag{1.15}$$

where the γ factor accounts for the region, that is moving relativistically and thus experiencing the CMB energy density amplified. The energy density of the CMB is calculated as

$$U_{\mathrm{CMB}} = 4.22 \cdot 10^{-13} (1+z)^4 \text{ erg cm}^{-3}. \tag{1.16}$$

Together with equation 1.15, we can write

$$B_{\mathrm{CMB}} = \sqrt{8\pi U_{\mathrm{CMB}}} = 3.24 \cdot 10^{-6} \gamma (1+z)^2 \text{ G}. \tag{1.17}$$

A non moving region at z=5 will therefore have $B_{\mathrm{CMB}} = 120$ μG, hence in the case of Cygnus A $B > B_{\mathrm{CMB}}$. Due to the large magnetic field of the hotspots, the radio emission from this region remains unaffected by the CMB at this distance, assuming the magnetic fields in hotspots to be independent of their redshift.
The hotspots experience adiabatic $\dot{\gamma}_{\mathrm{ad}}$ and radiative $\dot{\gamma}_{\mathrm{rad}}$ cooling rates described by

$$\dot{\gamma}_{\mathrm{ad}} = \frac{\gamma \, c \, \beta_{\mathrm{exp}}}{R}, \tag{1.18}$$

$$\dot{\gamma}_{\mathrm{rad}} = \frac{4 \, \sigma_{\mathrm{T}} \, \gamma^2}{3 \, m_{\mathrm{e}} \, c} \left(U_{\mathrm{B}} + U_{\mathrm{CMB}} + U_{\mathrm{S}} \right), \tag{1.19}$$

where β_{exp} is the expansion velocity in c, R is the radius of the expanded region, σ_{T} is the Stefan-Boltzmann constant, U_{B} is the energy density in equipartition with the magnetic field in the region, U_{CMB} is the energy density of the CMB and U_{S} is the energy density of the synchrotron radiation, where the electrons cool by the SSC mechanism. In the given scenario we can safely neglect the radiation losses via the SSC, since they are significantly smaller than those via the IC mechanism with CMB photons or the synchrotron losses. The power of the relativistic electrons $P_{\mathrm{e,jet}}$ fed by the jet, injected in the hotspots remaining to carry the power $P_{\mathrm{e,HS}} = 0.1 \cdot P_{\mathrm{e,jet}}$ (Nemmen et al. 2012; Ghisellini et al. 2014) and further into the lobe with the power $P_{\mathrm{e,lobe}}$ is assumed to be equal between the hotspots and the lobe ($P_{\mathrm{e,HS}} = P_{\mathrm{e,lobe}}$).

Lobe Emission

As with the hotspots, the model follows the description in Ghisellini et al. (2014). The lobe is assumed to be a spherical emitting region of radius $R_{\rm lobe}$, homogeneously filled with a magnetic field much weaker than that present in the hotspots. By that, the electrons in the lobes are interacting with the CMB such that the X-ray emission is enhanced, while the radio emission at frequencies $\lesssim 100\,$MHz is reduced in intensity, called quenched by the CMB. Lower energy electrons (corresponding to radio emission at lower frequencies), are less affected by CMB quenching, because the radiative cooling is ineffiecent at low enough energies, even considering the IC scattering with the CMB. This steepens the spectrum for low frequencies in the radio. A more detailed calculation can be found in Ghisellini et al. (2014).

1.3.2 Model Example: GB 1508+5714

With the introduced models for the jet, hotspots and lobe emission, this section displays one example with these models being applied to the target source GB 1508+5714, following Ghisellini et al. (2015). This target is also studied more in depth later on in Sect.4.2.

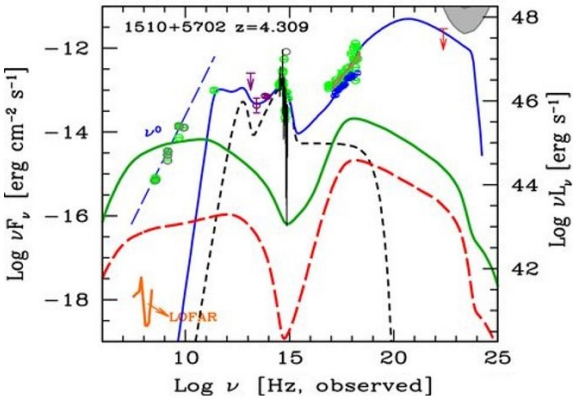

Figure 1.4: The modelled SED of blazar 1510+5702 (GB 1508+5714). The blue solid line is the model for the sum of the jet emission and thermal components. The black dashed line shows the thermal components, namely the accretion disk, the torus and the X-ray corona. For the hotspots plus the lobes contribution, two possible models are given: one with 0.1 $P_{\rm e,jet}$ (green lines) and the other with 0.01 $P_{\rm e,jet}$ (red lines). The dashed blue line is not a fit, but a line to guide the eye in the case of a flat spectrum in the low frequency radio range. The orange line indicates the sensitivity limit of LOFAR. The hatched gray area in the upper right corner shows the sensitivity of Fermi/LAT (5σ) after 5 years of observations (from Ghisellini et al. 2015).

The SED model (Fig. 1.4) was generated by Ghisellini et al. (2015), using the following parameters for **the jet**: redshift $z = 4.309$, distance of the dissipation region from the

black hole $R_{\rm diss} = 239 \cdot 10^{15}$ cm, the size of the BLR $R_{\rm BLR} = 636 \cdot 10^{15}$ cm, the power injected in the jet by relativistic electrons in the comoving frame $P'_{\rm e,jet} = 0.04 \cdot 10^{45}$ erg s^{-1}, the magnetic field $B = 2.6$ G, the bulk Lorentz factor $\gamma = 15$, the viewing angle $\theta = 3°$, the break Lorentz factor $\gamma_{\rm b} = 60$ and maximum Lorentz factor $\gamma_{\rm max} = 4 \cdot 10^3$ for the injected electron distribution, the slopes $s_1 = 0.5$ and $s_2 = 2.6$ for the injected electron distribution, the logarithm of the jet power in the form of radiation $\log(P_{\rm r}) = 46.4$ in erg s^{-1} and the logarithm of the total kinetic plus magnetic jet power $\log(P_{\rm jet}) = 47.5$ in erg s^{-1}.
The parameters used for **the hotspot and lobe** are for $P_{\rm HS,lobe}/P_{\rm jet} = 0.1$ and $P_{\rm HS,lobe}/P_{\rm jet} = 0.01$ respectively the following: The logarithm of the power injected throughout the hotspots and lobes by relativistic electrons $\log P_{\rm HS,lobe} = 46.5$ or $\log P_{\rm HS,lobe} = 45.5$ in erg s^{-1}, the magnetic field of the hotspot $B_{\rm HS} = 335$ μG or $B_{\rm HS} = 106$ μG, the logarithm of the energy in the magnetic field contained in the hotspots $\log E_{\rm B,HS} = 57.6$ or $\log E_{\rm B,HS} = 56.6$ in erg, the magnetic field of the lobe $B_{\rm lobe} = 26.8$ μG or $B_{\rm lobe} = 8.5$ μG and the logarithm of the energy in the magnetic field contained in the lobe $\log E_{\rm B,lobe} = 59.6$ or $\log E_{\rm B,lobe} = 58.6$ in erg. Also in both cases the radial size of the hotspots $R_{\rm HS} = 2$ kpc, the radial size of the lobe $R_{\rm lobe} = 50$ kpc, the break Lorentz factor $\gamma_{\rm b} = 10^3$ and maximum Lorentz factor $\gamma_{\rm max} = 10^6$ for the injected electron distribution, and slopes of the injected electron distribution $s_1 = -1$ and $s_2 = 2.7$.

The values of the powers and the energetics refer to one jet and one hotspot and lobe, while the lobe flux shown in the figures corresponds to two hotspots and lobes. This detailed tuning of the model allows to "turn on" or "turn off" the interaction of the electrons with the CMB at high redshifts, allowing to study the accuracy of the model with observations. This is shown in Sect. 4.2 on the basis of the high redshift blazar GB 1508+5714.

2 Principles of Radio Observations

Before diving into the studies, presented in this work, it is imperative to understand the workings and principles of radio observations, especially radio interferometry. This chapter will build an understanding not only for following the performed data acquisition and evaluation, but also the present challenges and limitations of the available instruments.

2.1 Photon Fluxes

The most common unit for flux density in radio astronomy is 1 Jansky, or 1 Jy (in memory of the protagonist of radio astronomy, Karl Guthe Jansky, e.g. Osterbrock & Ferland 2006):

$$\begin{aligned} 1\,\mathrm{Jy} &= 10^{-26}\,\mathrm{W\,m^{-2}\,Hz^{-1}} \\ &= 10^{-23}\,\mathrm{erg\,s^{-1}\,cm^{-2}\,Hz^{-1}} \end{aligned}$$

This unit was defined after the order of magnitude of the flux densities encountered in radio astronomy was established. Meanwhile, radio telescopes are sensitive enough to measure mJy (milli-Jy), μJy (micro-Jansky), and even the unit nJy (nano-Jy) has found its way into the relevant literature! Note that the term flux density, usually denoted by S_ν, means that it is a quantity defined per unit frequency or per unit bandwidth. In other words, flux density is the amount of energy acting on a unit area within a unit time per unit frequency. Integrating over the frequency, we get the flux S:

$$S = \int_0^\infty S_\nu \, \mathrm{d}\nu \tag{2.1}$$

While we want to draw conclusions from photon fluxes, usually radio telescopes measure the so-called antenna temperature, which is connected to the flux density depending on the effective antenna surface.

2.2 Antenna Temperature

The spectral power density P_ν received by an antenna is given by:

$$P_\nu = \frac{1}{2} A_{\text{eff}} \cdot S_\nu, \tag{2.2}$$

where A_{eff} is the effective antenna surface, while the factor $1/2$ results from polarization considerations.

2.3 Single Dish Radio Telescopes

Basic Concepts Generally (radio) telescopes collect incoming electromagnetic plane waves in their respective energy bands and convert them into spherical waves. This is not exactly the case for near-field conditions, but unless explicitly stated we assume far-field conditions. In order to understand the workings of telescopes, we must use geometric optics to calculate the required shape of the mirror (for a reflective telescope) or refractor (for a refractive telescope). In principle we want to collect as much power P as possible from a radiation emitting source with a flux density S_ν using the effective collecting area A_{eff} of the telescope:

$$P = \frac{1}{2} \cdot A_{\text{eff}} \cdot S_\nu \cdot \Delta\nu, \tag{2.3}$$

where $\Delta\nu$ is the bandwidth of the receiver equipment. It is important to note that this equation does not take further imperfections into account, e.g. other telescope properties, diffraction effects or "feed" (for radio telescopes horn or dipole) characteristics. These subsequent effects further reduce the received power calculated above, so this equation only provides a theoretical maximum value. Incoming electromagnetic waves propagate in free space, following the wave equation:

$$\vec{\nabla}^2 \vec{E} = \frac{1}{c^2} \frac{\partial^2 \vec{E}}{\partial t^2}, \tag{2.4}$$

with $\overrightarrow{E} \perp \overrightarrow{B}$. Because the wave can encounter plasma on its way to the observer (for example the Earth's ionosphere), a term describing current must be added:

$$\vec{\nabla}^2 \vec{E} = \frac{1}{c^2} \frac{\partial^2 \vec{E}}{\partial t^2} + \frac{4\pi}{c^2} \cdot \frac{\partial \vec{j}}{\partial t}. \tag{2.5}$$

This consideration is of great importance, especially for observations in the low frequency regime. However, for the sake of simplicity, we will only consider the case of free space, which means that the term describing the current can be neglected.

It is well known, that the given wave equation can be solved by plane waves of the form:

$$\vec{E}(z,t) = \vec{E}_0 \cdot e^{i(\omega t - k_z \cdot z + \Phi)}, \tag{2.6}$$

where $\vec{E}_0$ is the transverse wave in the (x,y)-plane propagating in the z-direction. i is the imaginary unit, ω is the angular frequency in radians per second, k_z is the wave vector in z-direction and Φ is the phase angle.

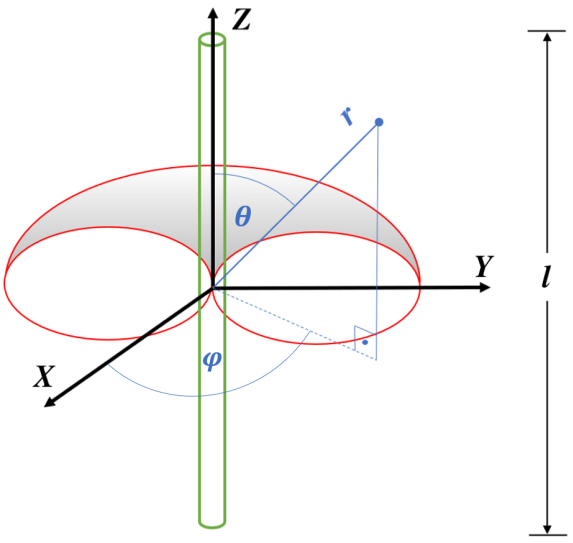

Figure 2.1: The Hertz dipole (green) of length l can emit electromagnetic waves with a given Poynting vector $\langle\vec{S}\rangle$. The flux $|\langle\vec{S}\rangle|$ depends on the angle θ. As indicated by the red torus, $\langle\vec{S}\rangle|$ is strongest in the (x,y)-plane and zero along the axis of the dipole.

Hertz Dipole The optical path in the mathematical description does not favor any time direction. Therefore, the description for emitting components and receiving components are mathematically the same. Because of this we can describe a dipole's sensitivity pattern by its radiation pattern. The components for the electric and magnetic field in spherical coordinates are given by:

$$H_\varphi = i \cdot \frac{I \cdot l}{4\pi} \cdot \frac{\sin\theta}{r} \cdot e^{-ikr} \cdot k \tag{2.7}$$

$$E_\theta = i \cdot \frac{I \cdot l}{4\pi} \cdot \frac{\sin\theta}{r} \cdot e^{-ikr} \cdot \omega\mu. \tag{2.8}$$

The electric field is only oriented in θ direction, and the magnetic field only in φ direction, hence perpendicular to each other. I is the electric current in the dipole, μ is the electromagnetic permeability. Note that the intrinsic impedance η of the medium is given by:

$$\frac{E_\theta}{H_\varphi} = \frac{\omega\mu}{k} = \sqrt{\frac{\mu}{\epsilon}} = \eta, \tag{2.9}$$

where ϵ is the permittivity.

The Poynting flux is defined by:

$$|\langle\vec{S}\rangle| = \frac{1}{2}\cdot|\Re(\vec{E}\times\vec{H}^\star)| = \frac{1}{2}\frac{\vec{r}}{r}\eta\cdot|H_\varphi|^2 = \frac{1}{2}\frac{\vec{r}}{r}\eta\left(\frac{I\cdot l\cdot k}{4\pi r}\right)^2\cdot\sin^2\theta \tag{2.10}$$

Here we can see that the flux is inversely proportional to the distance squared (i.e. $|\langle\vec{S}\rangle| \propto \frac{1}{r^2}$).

We can also see the directional dependence of the dipole radiation from the $\sin^2\theta$ term. As shown in the diagram, this represents a toroidal regime perpendicular to the dipole axis. This arrangement is called Hertz Dipole. In such a configuration, the dipole is a great receiver for broadcasting, but a poor radio telescope, due to the radial symmetry perpendicular to the dipole axis. We will see later in this chapter how combining many dipoles using interferometry can create a much better radio telescope.

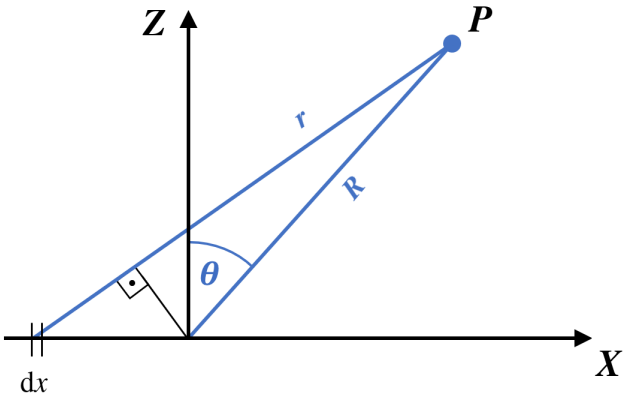

Figure 2.2: The aperture is in the (x, y)-plane and the point P is in its far field. The y-axis is perpendicular to the image plane. The infinitesimal element dx is at a distance x from the center of the coordinate system. Assuming that $R >> x$ and $r >> x$, we can conclude that $r \approx R + x\cdot\sin(\theta)$.

Aperture Field In order to connect aperture and the far field we assume a wave front coming from a certain point P at the angle θ, which is located at a distance R from the aperture along the y-axis with the extent a, as shown in Fig. 2.2. The electric field is made up of infinitesimal electric field contributions dE along that aperture. Summing

those up along the infinitesimal aperture elements dx leads to the evaluation of the signal coming from the point P. In the figure, the aperture extends in the y-direction, perpendicular to the image plane (x, z). With the considerations from the Hertz dipole, we can state:

$$\mathrm{d}E = -i \cdot \frac{E(x)}{2 \cdot \lambda \cdot R} \cdot e^{-ikr} \, \mathrm{d}x \, \mathrm{d}y. \tag{2.11}$$

Integrating this expression leads to:

$$E = -i \cdot \frac{a}{2 \cdot \lambda \cdot R} \cdot \int_{-\infty}^{+\infty} E(x) \cdot e^{-ikr} \, \mathrm{d}x, \tag{2.12}$$

with

$$a = \int_{-a/2}^{+a/2} \mathrm{d}y. \tag{2.13}$$

Further, if $R \gg x$ then

$$r \approx R + x \cdot \sin\theta. \tag{2.14}$$

Considering the above we can write:

$$E = -i \cdot \frac{a}{2 \cdot R} \cdot e^{-ikR} \cdot \int_{-\infty}^{+\infty} E\left(\frac{x}{\lambda}\right) \cdot e^{-i \cdot 2 \cdot \pi \cdot \left(\frac{x}{\lambda}\right) \cdot \sin\theta} \, \mathrm{d}\left(\frac{x}{\lambda}\right). \tag{2.15}$$

From here on we normalize all spatial dimensions by the wavelength λ. The terms on the left-hand side of the integral describe the behavior of the Poynting vector, i.e. $|\vec{S}| \sim |\vec{E}|$ and contains the wave propagation term e^{-ikr}. Neither of them is relevant for the far-field behavior, for which only the angular dependence of the electric field matters. During flux calibration of the received/transmitted signal, the term in front of the integral vanishes. Thus we introduce the electric field $\overline{E}$ preceding the integral as a multiplicative factor also containing the terms in front of the integral, which is normalized to dimensionless spatial coordinates by the wavelength:

$$\overline{E}(x_\lambda) = E(x_\lambda) \cdot \left(-\frac{i \cdot a}{2 \cdot R}\right) \cdot e^{-ikR}, \tag{2.16}$$

where $x_\lambda = x/\lambda$. By the substitution $\xi = \sin\vartheta$ we get a simple Fourier integral describing the relation between the aperture and far-field:

$$E(\xi) = \int_{-\infty}^{+\infty} \overline{E}(x_\lambda) \cdot e^{-i2\pi \cdot \xi \cdot x_\lambda} \, dx_\lambda \tag{2.17}$$

$$\overline{E}(x_\lambda) = \int_{-\infty}^{+\infty} \overline{E}(\xi) \cdot e^{-i2\pi \cdot \xi \cdot x_\lambda} \, d\xi. \tag{2.18}$$

Note that $E(\xi)$ is not directly describing properties of a (radio) telescope. For that we need the power pattern (antenna diagram)

$$F(\xi) = |E(\xi)|^2, \tag{2.19}$$

which determines the directivity of a telescope, i.e. its response to a source located at the far field distance.

2.4 Multi Dish Radio Arrays

Applying our knowledge from the previous chapters together with the knowledge about Fourier optics presented in this chapter it is possible to combine multiple dishes to an array and by this enhance the resolution capabilities of the instrument. This technique is being used since 1946 in radio astronomy, firstly applied by Ryle & Vonberg (1946) and since then more commonly used in the field of radio astronomy. This technique also finds application in the field of geophysics since small relative positional changes of the individual dishes impact the observation process and need to be corrected for a successful observation. Vice versa it is possible to use this corrections to determine movements between the dishes, e.g. continental plate movements.

2.4.1 Fourier Optics

Convolution

The concept of convolution is an important process to be understood by any astronomer. Convolution happens in every data taking process, especially in observations with telescopes. Here, the brightness distribution in the sky is convolved with the telescope's antenna pattern (also called "point spread function") while observing. But also, further processing of the collected data introduces effects of convolution (e.g., analogue-digital-conversion, data compression, filtering). Hence, we need to discuss convolution in the mathematical scope.

We assume a function $h(x)$, which is the convolution of $f(x)$ with another function $g(x)$. This is defined via the convolution integral

$$h(x) = \int_{-\infty}^{+\infty} f(u) \cdot g(x-u)\,\mathrm{d}u = f(x) \star g(x). \tag{2.20}$$

As an example of a convolution (see Fig. 2.3), consider a (one-dimensional) brightness distribution $f(x)$ observed with a radio telescope. The

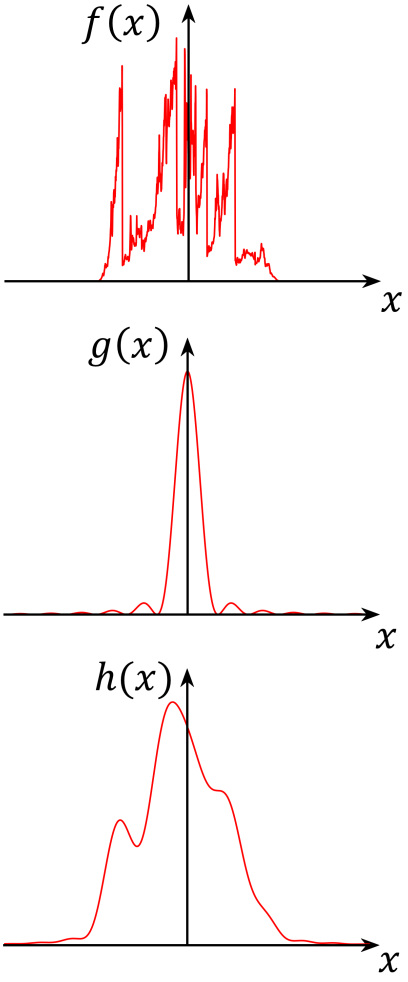

Figure 2.3: $h(x)$ is the convolution of the distributions $f(x)$ and $g(x)$. A single peak convolution smooths a signal like $h(x)$ so that broad features remain while narrow features disappear. The narrower the peak of $g(x)$, the more features of $f(x)$ remain in $h(x)$.

received signal $h(x)$ is the convolution of the brightness distribution $f(x)$ and the telescope antenna pattern $g(x)$. The main effect of this process is to "smooth" the original brightness distribution, that is, to remove small-scale details.

If we think of acoustics or electronic signals, convolution means suppression of high-frequency components, i.e. it acts like a low-pass filter. This process can be easily understood with the help of the convolution theorem. Below are some properties of convolution, the mathematical proofs of which are trivial:

- commutative, i.e. $f \star g = g \star f$
- associative, i.e. $f \star (g \star h) = (f \star g) \star h$
- distributive, i.e. $f \star (g + h) = f \star g + f \star h$

Auto- and Cross-Correlation

As the name implies, the auto-correlation function is the convolution of a function with itself:

$$R(x) = \int_{-\infty}^{+\infty} f(u) \cdot f(u - x)\, \mathrm{d}u, \tag{2.21}$$

or if normalized

$$\rho = \frac{\int_{-\infty}^{+\infty} f(u) \cdot f(u - x)\, \mathrm{d}u}{\int_{-\infty}^{+\infty} |f(u)|^2\, \mathrm{d}u}, \tag{2.22}$$

such that $\rho(0) = 1$. If the auto-correlation function is an even function and has its maximum at the origin then f is a real function, i.e.

$$\left.\begin{array}{ll} R(x) & = R(-x) \\ R(0) & \geq R(x) \end{array}\right\} \Rightarrow f \text{ real.} \tag{2.23}$$

Introducing a simple example, if $f(x) = \sin x$, then $\rho(x) = \cos x$. This already displays the following properties: if $f(x)$ is periodic, so are $R(x)$ and $\rho(x)$, with a cosinusoidal (or symmetric) behaviour. It is noteworthy that $R(x)$ loses any phase information. However, it is often easier in physics to measure the auto-correlation function! Consider the case where a function of interest is aperiodic and contains random components (e.g., noise); then its auto-correlation function will quickly drop to zero.
Analogous to the auto-correlation function, the cross-correlation of the two functions f and g is defined by:

$$h_{fg} = \int_{-\infty}^{+\infty} f(u-x) \cdot g(u)\, \mathrm{d}u. \tag{2.24}$$

If f and g are complex:

$$h_{fg}(x) = \int_{-\infty}^{+\infty} f^{\star}(u-x) \cdot g(u)\, du = h^{\star}_{gf}(-x). \tag{2.25}$$

Cross-correlation functions are used in determining correlation between any two functions. While completely unrelated functions will yield zero for all x, related functions lead to non-zero values for x in intervals that show correlation. Bear in mind though that correlation between two functions does not imply a causal relationship between them.

Fourier Theorems

The Fourier transform plays a significant role in many fields of physics and engineering, reaching far beyond the scope of this work. To understand the concepts of interferometry, it is crucial to understand concepts and properties of Fourier transformation, and its theorems in place. These theorems allow for easy construction of Fourier transforms in multiple applications, like the u-v plane, aperture- and far-field.

The Fourier transform of a function $f(x)$ is defined by

$$F(s) = \int_{-\infty}^{+\infty} f(x) \cdot e^{-i2\pi \cdot x \cdot s}\, \mathrm{d}x \;=:\; \mathscr{FT}[f(x)]. \tag{2.26}$$

And thus, its inverse transform by

$$f(x) = \int_{-\infty}^{+\infty} F(s) \cdot e^{i2\pi \cdot x \cdot s}\, \mathrm{d}s \;=:\; \mathscr{FT}^{-1}[F(s)]. \tag{2.27}$$

Similarity Theorem Assuming $f(x)$ has the Fourier transform $F(s)$, then the Fourier transform of $f(a \cdot x)$ can be obtained by

$$\mathscr{FT}[f(a \cdot x)] = \frac{1}{|a|} \cdot F\left(\frac{s}{a}\right). \tag{2.28}$$

A real world application is the calculation of the telescope beam (or, the telescope's resolution capability) by the aperture - $\theta \sim \lambda / D$.

Duality Theorem Assuming $f(x)$ has the Fourier transform $F(s)$, then the Fourier transform of $F(x)$ can be obtained by

$$\mathscr{FT}[F(x)] = 2\pi \cdot f(-s). \tag{2.29}$$

With this we can use known Fourier transforms to solve for functions which are harder to integrate analytically.

Shift Theorem Assuming $f(x)$ has the Fourier transform $F(s)$, then the Fourier transform of $f(x-a)$ can be obtained by

$$\mathscr{FT}[f(x-a)] = e^{-2\pi\cdot i\cdot s\cdot a}\cdot F(s). \tag{2.30}$$

This theorem is used in the electronic steering of radio telescopes that one is unable to steer mechanically in one or any direction.

Convolution Theorem Assuming $f(x)$ has the Fourier transform $F(s)$ and $g(x)$ has the Fourier transform $G(s)$ then the convolution of the base functions can be Fourier transformed as:

$$\mathscr{FT}[f(x)\star g(x)] = F(s)\cdot G(s). \tag{2.31}$$

When realizing that all measurements of any kind are a convolution of the equipment with the observables, it can be understood that this theorem is broadly applicable. If the experiment performs a Fourier transformation on the data e.g., analyzing frequencies in a signal, the frequency domain of the signal is multiplied by the filter properties in frequency domain. Assuming a rectangular filter where

$$F(\nu) = \begin{cases} 1, & \nu \in [0,s] \\ 0, & \nu \notin [0,s] \end{cases}. \tag{2.32}$$

Frequencies higher than s are filtered out and sharp discontinuities in the signal suffer overshoot effects (*Gibbs' phenomenon*, Hewitt & Hewitt 1979).

Auto-Correlation Theorem Assuming $f(x)$ has the Fourier transform $F(s)$ then the following auto-correlation applies:

$$\mathscr{FT}[R(x)] = |F(s)|^2, \tag{2.33}$$

with

$$R(x) = \int_{-\infty}^{+\infty} f(u)\cdot f(u-x)\,\mathrm{d}u. \tag{2.34}$$

The auto-correlation theorem itself is a special version of the convolution theorem. Highlighting this specific case is useful as it is frequently used in radio astronomy e.g. when calculating the power pattern of a field. Here $f(x)$ is the aperture field and therefore the above equation calculates the far-field pattern or antenna diagram.

Radio Telescopes as Spatial Filters

Any (radio) telescope, or even more broadly speaking, any sensory device that is build to collect data from an input source for further processing undergoes a convolution process. Here the input signal convolves with any intermediate influences to the signal (e.g. atmospheric absorption) as well as influences introduced from the observation device itself (e.g. sensitivity window, filters). These convolutions can be mathematically described with the help of the previously discussed theorems:

$$h(x) = \int_{-\infty}^{+\infty} f(u) \cdot g(x-u)\, du = f(x) \star g(x). \tag{2.35}$$

We use this description when observing a two-dimensional brightness distribution $B(\xi,\eta)$ with the antenna pattern $F(\xi,\eta)$, as displayed in Fig. 2.4:

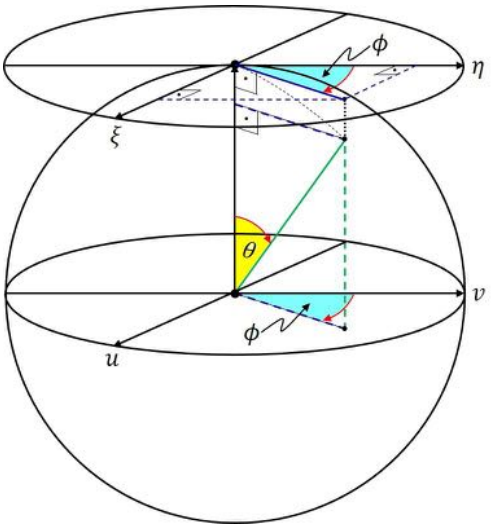

Figure 2.4: A telescope at the center of the (u,v)-plane observes a brightness distribution $B(\xi,\eta)$ in the sky (here represented by the ξ,η plane). Its recorded signal is the convolution of $B(\theta)$ and the antenna pattern of the telescope $F(\theta)$.

$$B_{\text{obs}}(\xi,\eta) = \iint_{4\pi} B(\xi',\eta') \cdot F(\xi-\xi',\eta-\eta')\, \mathrm{d}\Omega. \tag{2.36}$$

This function allows mathematically for a very broad field of alterations on the brightness distribution $B(\xi,\eta)$. For the real world application though, smoothing effects which remove high frequency components in the signal are limited.. Note that by "frequency", we do not refer here to observation frequencies. Following the Fourier theorems, this means a multiplication of the functions' Fourier transforms. We denote these relations as follows:

$$B_{\text{obs}}(\xi,\eta) = B(\xi,\eta) \star F(\xi,\eta) \tag{2.37}$$

and hence

$$\mathscr{FT}[B_{\text{obs}}](u,v) = \mathscr{FT}[B](u,v) \cdot \mathscr{FT}[F](u,v). \tag{2.38}$$

This equation formulates the so called spatial frequency filter. To visualize the process, follow it in Fig. 2.5. Note that, for simplicity, we only consider one dimension in the display ($v = 0$). As we consider the brightness distribution $B(\theta)$ being con-

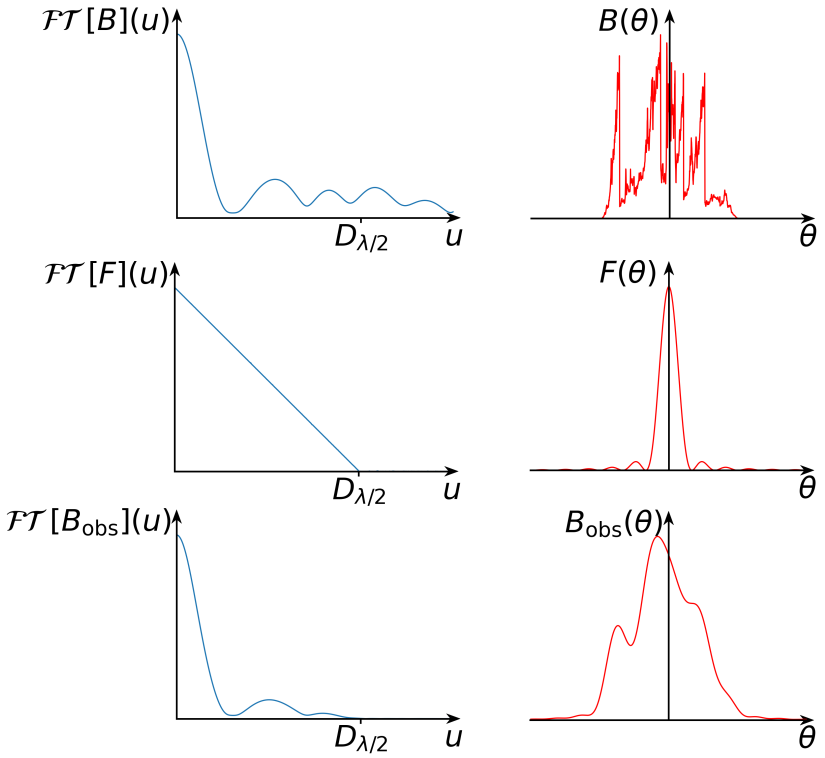

Figure 2.5: The plots on the right (red) are basically the same as those shown in Fig. 2.3. After calculating the Fourier transform on the left (blue) for the brightness function $B(\theta)$ and the response function $F(\theta)$, multiplying the Fourier transforms gives the same result as convolving the initial functions (right) and calculating the Fourier transform of the result $B_{\mathrm{obs}}(\theta)$.

volved (smoothed) with the antenna pattern $F(\theta)$ to the observed brightness distribution $B_{\mathrm{obs}}(\theta)$, their respective transforms act multiplicatively. Note that $\mathcal{FT}[F](u)$ for $u > D_{\lambda/2}$ is 0, which means that information here gets lost and this operation is non-reversible, where $D_{\lambda/2}$ is half the aperture size in units of the wavelength and is indirect proportional to the **H**alf **P**ower **B**eam **W**idth (HPBW). This cut-off for the higher u-values removes the higher-frequency components in the signal and therefore smooths it. This also means that the resolution capabilities of a telescope are defined by the size of it. For interferometry telescope arrays this is the distance between the furthest stations. Deconvolution processes are therefore always limited to the spatial frequency range $|u| \leq D_{\lambda/2}$ and deconvolved structures become less and less reliable beyond this limit. Follwoing the Rayleigh criterion (e.g., Bass et al. (2001)) the angular resolution can be approximated by:

$$\sin(\alpha) \approx 1.22\frac{\lambda}{D}. \tag{2.39}$$

Instrumental noise can create artefacts because the noise components are added after the convolution in the far-field. Also, because deconvolution is equivalent to dividing the observed brightness distribution by the reciprocal of the Fourier transform of the antenna pattern, the noise component is enhanced by this division in the aperture plane!

2.4.2 Interferometry

The Michelson Interferometer

Before diving into radio interferometers, we will first review the basic principles of interferometry by looking at the historic Michelson Interferometer experiment. Although this set up deals with optical wavelengths much shorter (around 500 nm) than we usually work with at radio wavelengths (mm to m), the same principles apply.

As shown in Fig. 2.6, consider two partial beams, originating from the emitting source (S). Upon arrival at the beam splitter (BS), some of the light passes through the BS to the first mirror M_1 and some is reflected toward the second mirror M_2. The split beams are reflected again by the mirrors and superposed at the beam splitter. The phase difference of the beams at the beam splitter δ depends on the path difference $(d_2 - d_1)$,

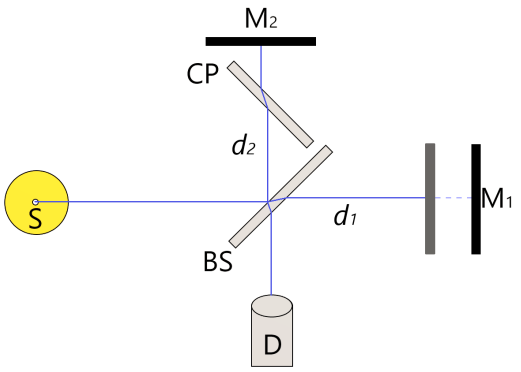

Figure 2.6: In this Michelson interferometer, a light source is positioned at point S. The emitted light reaches the beam splitter, where half of the intensity passes through and is reflected at the mirror M_1 after an adjustable distance d_1. The other half is reflected by 90°, passes a compensating plate CP before being reflected at the mirror M_2 at a fixed distance d_2. By setting $d_1 = d_2$, a constructive interference can be measured at the detector D.

$$\delta = \frac{4\pi}{\lambda}(d_2 - d_1). \tag{2.40}$$

By adjusting the mirror M_1 and thereby changing the value of d_2, the interferometer signal (or intensity) measured at point D is given by

$$I = \frac{1}{2} I_0 \left[1 + \cos\left(\frac{4\pi}{\lambda}(d_2 - d_1)\right)\right], \tag{2.41}$$

where I_0 is the peak intensity at $\delta = 0$. This relationship is only valid when using a coherent light source e.g. a monochromatic laser. If one wanted to do interferometry with white light, the path difference $(d_2 - d_1)$ would have to be very small i.e. less than the coherence length of white light. Only one of the light beams passes through the beam splitter and its dispersion causes a strongly wavelength dependent path length difference. To correct for this, one can place a correction plate (CP, in some literature also called compensation plate) in the path of the other beam, made of the same material and thickness as the beam splitter.

Once we understand this set up, we can exchange the laboratory light source

with a distant object, e.g. a star a few lightyears away. The huge distance to the emitter means the incoming signal can be treated as a parallel wavefront being picked up at two mirrors m_1 and m_4, redirected by further mirrors m_2 and m_3 into a telescope tube, where the superposed optic wave can be collected with a charge-coupled device (CCD) for example (see Fig. 2.7). When sweeping over the star, hence changing the path difference Δ, we can detect a wave pattern in the signal. The wave patterns shown below are also called fringes.

If the star is a point source, i.e. if its angular size is small compared to the separation of the interference maxima, then the star's image is represented by alternating bright and dark bands. If the angular extent of the source is larger, the maxima resulting from different emitting regions of the brightness distribution are no longer coincident (see dashed line in Fig. 2.7). As a result, the amplitude of the fringes decreases, and completely disappears for very extended sources. In this simple example we can define a measure of the relative amplitude of the fringes as: This measure is also referred to as the visibility function (or simply visibility). Because this measure is dependent on the morphology of the source, in our example point-like or a disk with a certain radius, we achieve significantly improved resolution capabilities to measure the size of objects. This allowed for the first direct measurement of the diameter of a star with an optical telescope: Michelson and Pease were able to measure the diameter of Betelgeuse in December 1920 (Michelson & Pease 1921) to be around 380 million kilometers (about the size of the orbit of Mars).

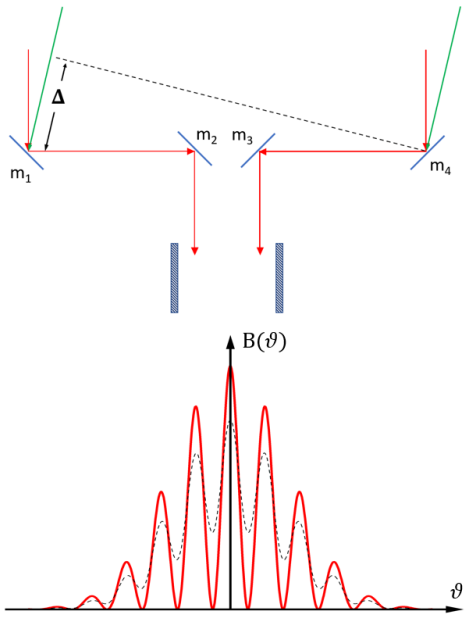

Figure 2.7: A telescope works like a Michelson interferometer. Depending on the position of the light source, there is a path difference Δ for the incoming parallel waves. Changing the orientation θ of the telescope also changes Δ. As with a Michelson interferometer, a fringe pattern $B(\theta)$ is produced (red = point source; dashed = small extended source).

This principle is used analogously in radio-astronomy. Disturbances of the plane wave between target and observer (telescope) need to be accounted for: in optical applications, these can include atmospheric turbulence, diffraction from the mirrors, and the finite bandwidth of incoming radiation. Radio telescopes utilizing interfer-

ometry techniques likewise have their disturbances. Observing in the cm regime, where the atmosphere is pretty much transparent, there are usually no atmospheric fluctuations needed to be accounted for. At longer wavelengths, the ionosphere becomes influential due to varying electron counts, leading to strong phase fluctuations. Moving to shorter wavelengths (mm and sub-mm regime), the troposphere becomes noticeable due to the water vapor content.

The Two-Element Interferometer

Observing in the radio regime with a twin-interferometer set up, some assumptions are used in order to simplify the mathematics of interferometry. The three most important assumptions are:

1. the distance d of the source is much larger than the separation D of any two telescopes of an interferometer,
2. the bandwidth $\Delta\nu$ is much smaller than the observing frequency ν and
3. the angular size Θ_S of the source is much smaller than the fringe width.

These assumptions simplify the following chapters dealing with the properties of an interferometer, in particular its spatial filtering property.

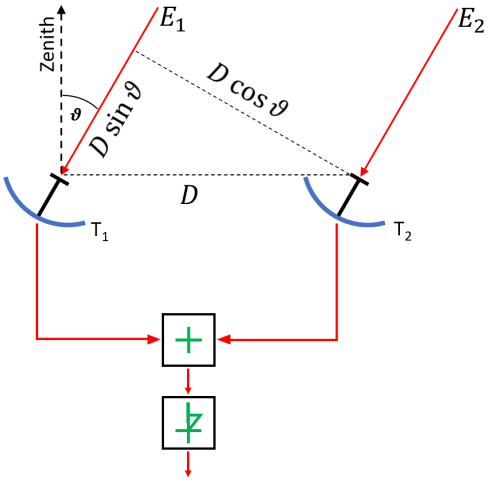

Figure 2.8: Two telescopes arranged as a simple adding interferometer. The recorded signals are added. To calculate the time difference $\tau_g = D/c\sin(\vartheta)$ the telescopes must be stationary in this configuration.

Adding Interferometer The first interferometer type we want to look at is the "adding interferometer" which simply adds the signals (voltages) received by two telescopes and passes on the added signal (see Fig. 2.8). We can use geometry to calculate the time delay to the second telescope with a longer travel distance for the signal as:

$$\tau_g = \frac{D}{c}\cdot\sin\vartheta. \tag{2.42}$$

In this set up we assume the telescopes to be stationary and non steerable. The far-field brightness distribution will however be shifted due to the Earth's rotation. This allows us to calculate the far-field signal (voltages) $E(\vartheta)$ of the interferometer. We calculate

the phase shift as $\Psi = 2\pi \cdot \nu \cdot \tau_g$, introduced by the time lag between the different paths of the signal, i.e.

$$\Psi = 2\pi \cdot \frac{D}{\lambda} \cdot \sin\vartheta = 2\pi D_\lambda \cdot \xi. \tag{2.43}$$

Assuming the signal is in the center of the baseline D of the interferometer, the received signals are phase-shifted with respect to the center by $\pm\Psi/2$ for the telescopes T_1 and T_2, leading to the following far-field signal (voltages) as the sum of the phase shifted individual signals with

$$E(\vartheta) = E_1(\vartheta) \cdot e^{i\frac{\Psi}{2}} + E_2(\vartheta) \cdot e^{-i\frac{\Psi}{2}}. \tag{2.44}$$

Assuming that the telescopes have the same properties, we expect the signals $E_1(\vartheta) = E_2(\vartheta) = E_0(\vartheta)$ so that

$$E(\vartheta) = E_0(\vartheta) \cdot (e^{i\frac{\Psi}{2}} + e^{-i\frac{\Psi}{2}}) = E_0(\vartheta) \cdot 2 \cdot \cos\left(\frac{\Psi}{2}\right). \tag{2.45}$$

Using the complex conjugate, the power pattern can be calculated as

$$P(\vartheta) = E_0 \cdot E_0^\star = 4 \cdot |E_0(\vartheta)|^2 \cdot \cos^2\left(\frac{\Psi}{2}\right) = 2 \cdot |E_0(\vartheta)|^2 \cdot (1 + \cos(\Psi)), \tag{2.46}$$

with * denoting the complex conjugate and $2 \cdot |E_0(\vartheta)|^2 = P_0(\vartheta)$ we thus obtain

$$P(\vartheta) = P_0(\vartheta) \cdot (1 + \cos(\Psi(\vartheta))). \tag{2.47}$$

The same result can be obtained by starting with the aperture distributions in combination with the auto-correlation theorem, which was covered in previous sections. The resulting antenna diagram is therefore a fringe pattern of $1 + \cos(\Psi)$, which is modulated by the power pattern $P_0(\vartheta)$ of the individual telescopes.
While very illustrative, this first radio interferometer has a substantial drawback: noise terms in the collected power have a very strong influence. If both telescopes produce the voltages V_1 and V_2 carrying the signal and have respective noise δV_1 and δV_2, then the measured power after summing and rectifying the signals yields:

$$P = \langle (V_1' + V_2')^2 \rangle = \langle V_1^2 \rangle + \langle V_2^2 \rangle + 2 \cdot \langle V_1 \cdot V_2 \rangle + \langle \delta V_1^2 \rangle + \langle \delta V_2^2 \rangle, \tag{2.48}$$

$$V_1' = V_1 + \delta V_1 \text{ and } V_2' = V_2 + \delta V_2, \tag{2.49}$$

where $\langle\rangle$ means a time average. Here we see that the noise terms appear quadratically in the final power, while they do not appear in the mixing product because they are

uncorrelated. Most (with a few exceptions) radio sources in the sky are rather weak in comparison to the noise introduced by the instrument. Improving the equipment quickly reaches engineering limits and therefore adding interferometers is only practical for smaller baselines ($D_{\max} \leq 200\,\mathrm{m}$). In order to solve this problem another approach was introduced.

Phase-Switched Interferometer The phase-switched interferometer, invented by Sir Martin Ryle (1952), is able to overcome the known noise issues for adding interferometers, especially with increasing baselines. As the name implies, a phase shift of 180° is added to the signal coming from one telescope before entering the adder. The sign of the signals is also synchronously changed by an operational amplifier after adding and rectification leading to a positive sum of the signal having the phase delay and the negative sum missing the phase lag. Picking up the far-field signals, derived above, we now have two: one in phase and another out of phase. These are given by:

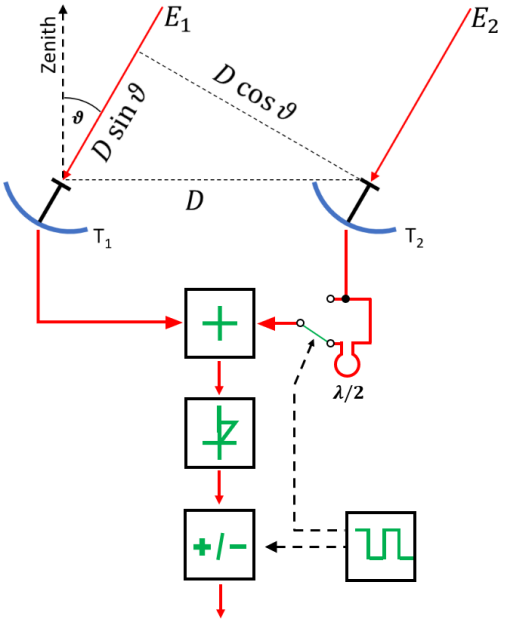

Figure 2.9: Two telescopes arranged as a phase-switched interferometer. One of the two signals is alternately switched by 180° with sign reversal. This allows the noise to be more accurately identified and removed. The final combined signal is further amplified.

$$E_+(\vartheta) = E_0(\vartheta) \cdot (e^{i\Psi/2} + e^{-i\Psi/2}) \tag{2.50}$$

$$E_-(\vartheta) = E_0(\vartheta) \cdot (e^{i\Psi/2} - e^{-i\Psi/2}). \tag{2.51}$$

Their corresponding powers are

$$P_+(\vartheta) = |E_0(\vartheta)|^2 \cdot (e^{i\Psi/2} + e^{-i\Psi/2}) \cdot (e^{i\Psi/2} + e^{-i\Psi/2})^\star \tag{2.52}$$

$$P_-(\vartheta) = |E_0(\vartheta)|^2 \cdot (e^{i\Psi/2} - e^{-i\Psi/2}) \cdot (e^{i\Psi/2} - e^{-i\Psi/2})^\star. \tag{2.53}$$

Calculating the difference of the powers to be $P(\vartheta) = P_+(\vartheta) - P_-(\vartheta)$ we can write

$$P(\vartheta) = 4 \cdot |E_0(\vartheta)|^2 \cdot [\cos^2(\Psi/2) - \sin^2(\Psi/2)] = 2 \cdot |E_0(\vartheta)|^2 \cdot \cos(\Psi), \tag{2.54}$$

or simply

$$P(\vartheta) = P_0(\vartheta) \cdot \cos(\Psi). \tag{2.55}$$

Considering the noise terms, as previously done for the adding interferometer, the voltages contribute to the power in the following way

$$P = \langle V_1' + V_2' \rangle^2 - \langle V_1' - V_2' \rangle^2, \tag{2.56}$$

which is the correlation of both voltages when integrated over some time constant T. The uncorrelated terms cancel out considering the measured voltages are the true signal plus the noise terms

$$V_1'(t) = V_1(t) + \delta V_{(t)}, \tag{2.57}$$

$$V_2'(t) = V_2(t) + \delta V_{(t)}. \tag{2.58}$$

To calculate the power using the integral, we find

$$P(\tau) = \frac{1}{2T} \int_{-T}^{+T} V_1'(t) \cdot V_2'(t+\tau)\, dt = \frac{1}{2T} \int_{-T}^{+T} V_1(t) \cdot V_2(t+\tau)\, dt. \tag{2.59}$$

Which gives

$$P = \langle V_1' + V_2' \rangle^2 - \langle V_1' - V_2' \rangle^2 = 4 \cdot \langle V_1 \cdot V_2 \rangle \tag{2.60}$$

As shown, we can get rid of the noise terms in this set up which allows us to go to higher frequencies and use much longer baselines than before because we can measure the complex visibilities much more precisely!

In today's radio interferometers we use so-called **correlation interferometers** instead, where the correlation (i.e. multiplication and time averaging) is accomplished digitally in a computer. Other than that the procedure is the same as just described.

The Visibility Function

Knowing the basics of how an interferometer transforms the emission of a radio point source, the next step is to mathematically define a general basis to describe the relationship between the interferometer response and the brightness distribution. The approach to do so is to convolve the brightness distribution $B(\theta, \phi)$ with the antenna diagram $F(\theta, \phi)$ or, equivalently, with its effective surface $A(\theta, \phi)$. With this approach we will see that the concept of visibility, or a visibility function, will appear quite naturally. Another, more basic mathematical approach is the so-called van-Citter-Zernike theorem, which is more extensive and therefore out of the scope of this work.
In contrast to the former set up, we now assume that the telescopes move to track the source of interest. The unit vector $\vec{s_0}$ points to the center of the region of observation,

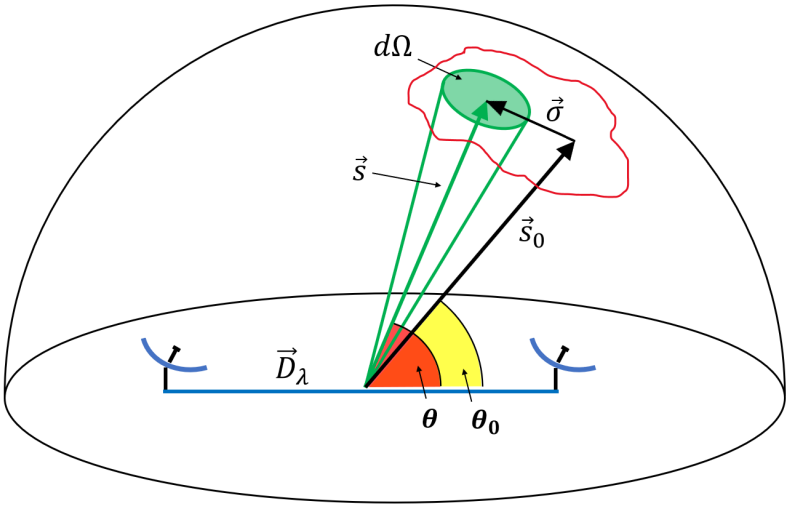

Figure 2.10: This schematic shows an interferometer with the baseline $\vec{D}_\lambda$ between the two elements along a phase center pointed at by $\vec{s}_0$. This set up can also give brightness information in the field of view at any position $\vec{s}$.

also referred to as the phase center. The solid-angle element $d\Omega$ at some arbitrary position in this field is defined by the vector $\vec{s} = \vec{s}_0 + \vec{\sigma}$ and contributes the power of

$$dP = A(\vec{\sigma}) \cdot B(\vec{\sigma}) \cdot d\Omega \cdot \Delta\nu, \tag{2.61}$$

where $A(\vec{\sigma})$ is the effective antenna area, $B(\vec{\sigma})$ the brightness distribution of the source, and $\Delta\nu$ the effective bandwidth of the receiver systems. The effective antenna area $A(\vec{\sigma})$ and the antenna diagram $F(\vec{\sigma})$ are related such that

$$A(\vec{\sigma}) = A(0) \cdot \frac{F(\vec{\sigma})}{F(0)} := A(0) \cdot A_{\mathrm{N}}(\vec{\sigma}). \tag{2.62}$$

As shown in the previous chapter, the correlated power must contain the fringe term, so that

$$dP = A(\vec{\sigma}) \cos(\Psi) \cdot B(\vec{\sigma}) \cdot d\Omega \cdot \Delta\nu, \tag{2.63}$$

where $\Psi = 2\pi \cdot \frac{\vec{D}}{\lambda}\vec{s}$ for the two dimensional case. Keep in mind that $\vec{D} \cdot \vec{s} = D \cdot \cos(\theta)$ which we have already seen before as $D \cdot \sin(\vartheta)$ and we can adjust it to the current notation via the geometric definition $\theta = 90° - \vartheta$.

With these relations we can construct the power received by the correlation interferometer by integrating over the source:

$$P(\vec{D}_\lambda, \vec{s}_0) = \Delta\nu \cdot \iint\limits_{\text{Source}} A(\vec{\sigma}) \cdot B(\vec{\sigma}) \cdot \cos[2\pi \cdot \vec{D}_\lambda \cdot (\vec{s}_0 + \vec{\sigma})] \, \mathrm{d}\Omega. \tag{2.64}$$

rewriting this with the trigonometric relation $\cos(\alpha+\beta) = \cos(\alpha)\cdot\cos(\beta) - \sin(\alpha)\cdot\sin(\beta)$ we obtain:

$$\begin{aligned} P(\vec{D}_\lambda, \vec{s}_0) = \Delta\nu \cdot \cos(2\pi \cdot \vec{D}_\lambda \cdot \vec{s}_0) \cdot \iint\limits_{\text{Source}} A(\vec{\sigma}) \cdot B(\vec{\sigma}) \cdot \cos(2\pi \cdot \vec{D}_\lambda \cdot \vec{\sigma})\, \mathrm{d}\Omega \\ -\Delta\nu \cdot \sin(2\pi \cdot \vec{D}_\lambda \cdot \vec{s}_0) \cdot \iint\limits_{\text{Source}} A(\vec{\sigma}) \cdot B(\vec{\sigma}) \cdot \sin(2\pi \cdot \vec{D}_\lambda \cdot \vec{\sigma})\, \mathrm{d}\Omega. \end{aligned} \tag{2.65}$$

Implementing the normalized antenna diagram $A_\mathrm{N}(\vec{\sigma})$ we can define a function, the complex visibility function V, such that

$$V = |V| \cdot e^{i\rho_\mathrm{v}} = \iint\limits_{\text{Source}} A_\mathrm{N}(\vec{\sigma}) \cdot B(\vec{\sigma}) \cdot e^{-i2\pi \cdot \vec{D}_\lambda \cdot \vec{\sigma}}\, \mathrm{d}\Omega, \tag{2.66}$$

with ρ_v as the visibility phase. Separating the real and imaginary parts, we obtain

$$|V| \cdot \cos(\rho_\mathrm{v}) = \iint\limits_{\text{Source}} A_\mathrm{N}(\vec{\sigma}) \cdot B(\vec{\sigma}) \cdot \cos(2\pi \cdot \vec{D}_\lambda \cdot \vec{\sigma}) \cdot d\Omega = \Re V \tag{2.67}$$

$$|V| \cdot \sin(\rho_\mathrm{v}) = -\iint\limits_{\text{Source}} A_\mathrm{N}(\vec{\sigma}) \cdot B(\vec{\sigma}) \cdot \sin(2\pi \cdot \vec{D}_\lambda \cdot \vec{\sigma}) \cdot d\Omega = \Im V \tag{2.68}$$

and hence for the power, defining $A_\mathrm{N}(\vec{\sigma}) = \frac{A(\vec{\sigma})}{A_0}$:

$$P(\vec{D}_\lambda, \vec{s}_0) = A_0 \cdot \Delta\nu \cdot |V| \cdot \cos(2\pi \cdot \vec{D}_\lambda \cdot \vec{s}_0 - \rho_\mathrm{v}). \tag{2.69}$$

This result describes the output of the correlator as a fringe pattern with a period corresponding to that of a hypothetical source at the position $\vec{s}_0$. The amplitude and phase of the fringe pattern are equal to those of the complex visibility function V, while the visibility phase ρ_v is measured relative to the hypothetical source at the position $\vec{s}_0$. The visibility amplitude $|V|$ has the units of spectral energy flux density (W m^{-2} Hz^{-1}), which is consistent with the definition of B and the Fourier transform relation. The identity of the visibility defined above is clearer when normalizing the complex visibility function to

$$V_N = \frac{S_\mathrm{max} - S_\mathrm{min}}{S_\mathrm{max} + S_\mathrm{min}}. \tag{2.70}$$

S_max is the maximum value in the fringe pattern at the center, while S_min is the value of the next minimum to the center (compare to $B(\vartheta)$ values in the fringe pattern in Fig. 2.7). As stated before, we assume small angular sizes for the sources, so we can set

$A_N(\vec{\sigma}) \approx A_N(0,0) = 1$ which leads to the simplification of the visibility function defined by the integral:

$$V = \iint_{\text{Source}} B(\vec{\sigma}) \cdot e^{-i2\pi \cdot \vec{D}_\lambda \cdot \vec{\sigma}} \, \mathrm{d}\Omega. \tag{2.71}$$

At this point one can see that the visibility is nothing but the Fourier spectrum of the brightness distribution as measured with an interferometer. Using orthogonal coordinates coordinates in the telescope system, to describe the baseline $\vec{D}_\lambda = (u, v)$ and the corresponding directional cosines $\vec{\sigma} = (\xi, \eta)$ at the sky, the simplified visibility function becomes

$$V = \iint B(\xi, \eta) \cdot e^{-i2\pi \cdot (u \cdot \xi + v \cdot \eta)} \, \mathrm{d}\xi \, \mathrm{d}\eta. \tag{2.72}$$

Ultimately our goal is to reconstruct the brightness distribution $B(\xi, \eta)$ which is why we need to Fourier invert this equation. By measuring the visibility for many different baselines $\vec{D}_\lambda$ we can retrieve the brightness distribution via $\mathcal{FT}^{-1}[V(u, v)]$, leading to

$$B(\xi, \eta) = \iint V(u, v) \cdot e^{i2\pi \cdot (u \cdot \xi + v \cdot \eta)} \, \mathrm{d}u \, \mathrm{d}v. \tag{2.73}$$

The Influence of Limited Bandwidth

In the previous sections we shed some light on principles of interferometry while mostly neglecting bandwidth effects. Given that correlation interferometers are currently the best interferometer set-up option, we want to take this as a basis for our analysis of bandwidth effects. Assuming the usual two antenna interferometer with distance D between them, each is equipped with amplifier A_1, A_2 respectively. Additionally we want to introduce the artificial time delay τ_i in one of the signal lines from the amplifier to the multiplier, that correlates the signal. The multiplier is followed by an integrator with an integration time of $2T$, i.e. the output of the multiplier is integrated for a duration of $2T$, passed on as a voltage, a current, or a coded signal pro-

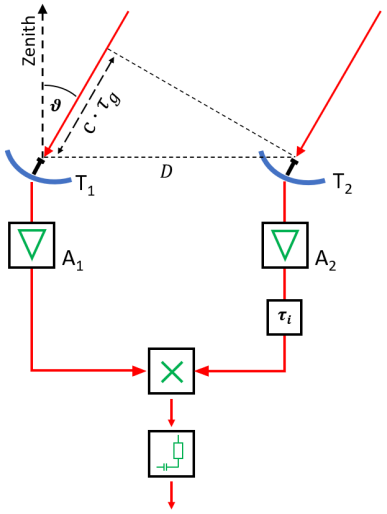

Figure 2.11: The signal from the two-telescope interferometer is amplified by the units A_1 and A_2. Due to the path difference, a time delay τ_i is introduced into one of the telescope signals. Finally, they are correlated and time integrated.

portional to the power (i.e. voltage squared).
Thus we can write mathematically:

$$P(\tau_g) = \lim_{T\to\infty} \frac{1}{2T} \int_{-T}^{+T} V_2(t) \cdot V_1(t-\tau_g)\, \mathrm{d}t, \tag{2.74}$$

which is similar to the cross-correlation function. It is necessary to choose the integration time $2T$ to be much larger than the reciprocal bandwidth. This ensures a sufficient signal length to be correlated. In this case $\Delta\nu$ is the bandwidth of the receiver and has to be smaller than the reciprocal of the fringe period. Having the time dependent correlation product in mind, its output voltage delivered by the multiplier is proportional to

$$F = 2 \cdot \sin(2\pi \cdot \nu \cdot t) \cdot \sin[2\pi \cdot \nu \cdot (t-\tau_g)] \tag{2.75}$$

$$= \cos(2\pi \cdot \nu \cdot \tau_g) - \cos(4\pi \cdot \nu \cdot t) \cdot \cos(2\pi \cdot \nu \cdot \tau_g) - \sin(4\pi \cdot \nu \cdot t) \cdot \sin(2\pi \cdot \nu \cdot \tau_g). \tag{2.76}$$

Usually ν is in the range of several 10...100 GHz. As previously shown, the geometric time delay τ_g is given by

$$\tau_g = \frac{D}{c} \cdot \sin\vartheta \Rightarrow \nu \cdot \tau_g = \frac{D}{\lambda} \cdot \sin\vartheta. \tag{2.77}$$

We want to have a general sense of the parameter values that we achieve when working with current interferometers. The fastest possible variation of ϑ is caused by the Earth's rotation ($\dot{\vartheta} = \omega_\mathrm{E} \approx 7 \cdot 10^{-5} \mathrm{rad\,s^{-1}}$). In such a set up we can expect the range of variations of $\nu \cdot t$ and $\nu \cdot \tau_g$:

$$\frac{d(\nu \cdot t)}{dt} = \nu = 300\ \mathrm{MHz\ (VLA)...20\ GHz\ (VLA)...230\ GHz\ (NOEMA)} \tag{2.78}$$

$$\frac{d(\tau_g \cdot \nu)}{dt} = \frac{D}{\lambda} \cdot \dot{\vartheta} = 7 \cdot 10^{-5} \cdot \mathrm{rad\,s^{-1}} \cdot \left(\frac{30\ \mathrm{km}}{1\ \mathrm{m}} ... \frac{30\ \mathrm{km}}{1.5\ \mathrm{cm}} ... \frac{600\ \mathrm{m}}{92\ \mathrm{cm}} \right) \tag{2.79}$$

$$= D_\lambda \cdot \omega_\mathrm{E} = 2.1\ \mathrm{Hz} \ldots 140\ \mathrm{Hz} \ldots 7\ \mathrm{Hz} \tag{2.80}$$

Moving to a more extreme interferometer set up, like a global VLBI array (e.g. the VLBA), where we usually observe in the cm wavelength regime, we obtain:

$$\frac{d(\tau_g \cdot \nu)}{dt} = \frac{D}{\lambda} \cdot \dot{\vartheta} = 7 \cdot 10^{-5} \cdot \mathrm{rad\,s^{-1}} \cdot \frac{8600\ \mathrm{km}}{1\ \mathrm{cm}} \approx 60\ \mathrm{kHz} \tag{2.81}$$

The maximum of terrestrial baselines is constrained by $D/\lambda \leq 10^9$, while the variation of $\nu \cdot \tau_g$ is at least five magnitues smaller than that of $\tau \cdot t$. This allows us to filter out the

fast variations in the multiplier output by time averaging $1/(2T)\int_{-T}^{+T} V(t)\cdot V(t-\tau_g)\,\mathrm{d}t$. Then, only variations of interest remain.

$$F = \cos\left(\frac{2\pi D}{\lambda}\cdot\sin\vartheta\right) = \cos\left(\frac{2\pi D}{\lambda}\cdot\xi\right). \tag{2.82}$$

With the aim of inspecting the effects of the finite bandwidth on the fringe pattern, we first need to simplify some things. We assume the target source to be a continuum source, i.e. the time-averaged amplitude of the radio signal is constant over the bandwidth $\Delta\nu$. From the Fourier theorems, especially the auto-correlation, the power spectrum of a signal is equal to the Fourier transform of the auto-correlation function of the signal. This allows us to completely characterize the constant spectrum by the bandpass properties. This implies that the correlator-output signal (as a function of τ_g) is the Fourier transform of the power spectrum, hence of the bandpass itself. Knowing this and the Fourier theorems, we can deduce the following relations between the correlator power output $P(\tau)$ and the power spectrum $|H(\nu)|^2$ as:

$$|H(\nu)|^2 = \int_{-\infty}^{+\infty} P(\tau)\cdot e^{-i2\pi\cdot\nu\cdot t}\,\mathrm{d}t \tag{2.83}$$

$$P(\tau) = \int_{-\infty}^{+\infty} |H(\nu)|^2\cdot e^{i2\pi\cdot\nu\cdot t}\,\mathrm{d}\nu \tag{2.84}$$

When considering different shapes of the bandpass, we already know that, e.g. a rectangular bandpass' transform leads to a sinc pattern with which $P(\tau)$ will be modulated (multiplied); a Gaussian bandpass results in a Gaussian modulation. The case of a rectangular bandpass is easily shown mathematically. We were already able to derive the output signal from the visibility function. Now assuming $\vec{D}_\lambda\cdot\vec{s}_0 = \nu\cdot\tau_g$ the power within an infinitesimally small spectral range $d\nu$ is given by

$$dP = A_0\cdot|V|\cdot\cos(2\pi\cdot\nu\cdot\tau_g - \varphi_\mathrm{v})\,\mathrm{d}\nu. \tag{2.85}$$

To receive the power for the whole whole bandwidth, we need to perform the following integration:

$$P = A_0\cdot|V|\cdot\int_{\nu_0-\frac{\Delta\nu}{2}}^{\nu_0+\frac{\Delta\nu}{2}} \cos(2\pi\cdot\nu\cdot\tau_g - \varphi_\mathrm{v})\,\mathrm{d}\nu. \tag{2.86}$$

We want to focus on the integral part as the values in front are just constants:

$$\int_{\nu_0-\frac{\Delta\nu}{2}}^{\nu_0+\frac{\Delta\nu}{2}} \cos(2\pi\cdot\nu\cdot\tau_g - \varphi_\mathrm{v})\,\mathrm{d}\nu = \frac{\sin(2\pi\cdot\nu\cdot\tau_g - \varphi_\mathrm{v})}{2\pi\cdot\tau_g}\Bigg|_{\nu_0-\frac{\Delta\nu}{2}}^{\nu_0+\frac{\Delta\nu}{2}} \tag{2.87}$$

$$= \frac{1}{2\pi \cdot \tau_g} \left\{ \sin\left[2\pi\left(\nu_0 + \frac{\Delta\nu}{2}\right)\cdot\tau_g - \varphi_\mathrm{v}\right] - \sin\left[2\pi\left(\nu_0 - \frac{\Delta\nu}{2}\right)\cdot\tau_g - \varphi_\mathrm{v}\right]\right\} \tag{2.88}$$

Here we can use the trigonometric relation $\sin\alpha - \sin\beta = 2\cos(\frac{\alpha+\beta}{2})\cdot\sin(\frac{\alpha-\beta}{2})$:

$$\begin{aligned} = \frac{1}{\pi \cdot \tau_g} \Bigg\{ &\cos\left[\frac{2\pi(\nu_0 + \frac{\Delta\nu}{2})\cdot\tau_g - \varphi_\mathrm{v} + 2\pi(\nu_0 - \frac{\Delta\nu}{2})\tau_g - \varphi_\mathrm{v}}{2}\right] \\ &\cdot \sin\left[\frac{2\pi(\nu_0 + \frac{\Delta\nu}{2})\cdot\tau_g - \varphi_\mathrm{v} - 2\pi(\nu_0 - \frac{\Delta\nu}{2})\tau_g + \varphi_\mathrm{v}}{2}\right]\Bigg\} \end{aligned} \tag{2.89}$$

$$= \frac{1}{\pi \cdot \tau_g} \cdot \cos(2\pi\nu_0 \cdot \tau_g - \varphi_\mathrm{v}) \cdot \sin(\pi \cdot \Delta\nu \cdot \tau_g) \tag{2.90}$$

$$= \Delta\nu \frac{\sin(\pi \cdot \Delta\nu \cdot \tau_g)}{\pi \cdot \Delta\nu \cdot \tau_g} \cdot \cos(2\pi \cdot \nu_0 \cdot \tau_g - \varphi_\mathrm{v}). \tag{2.91}$$

Having this solution we can rewrite the initial relation for a rectangular shaped bandpass output power as:

$$P = A_0 \cdot |V| \cdot \Delta\nu \frac{\sin(\pi \cdot \Delta\nu \cdot \tau_g)}{\pi \cdot \Delta\nu \cdot \tau_g} \cdot \cos(2\pi \cdot \nu_0 \cdot \tau_g - \varphi_\mathrm{v}). \tag{2.92}$$

When using a Gaussian bandpass, the same equation becomes:

$$P = A_0 \cdot |V| \cdot \Delta\nu \cdot e^{-3.65\cdot\tau_g^2\cdot\Delta\nu^2} \cdot \cos(2\pi \cdot \nu_0 \cdot \tau_g - \varphi_\mathrm{v}). \tag{2.93}$$

Comparing the influence of τ_g in both cases, we can see that the fringe pattern is more strongly attenuated for higher τ_g.

Depending on the bandpass shape, the attenuation follows a so-called delay pattern, or fringe-washing function. To receive the most power from the source, the observation should stay near the maximum of the function, which can be accomplished by the introduction of an artificial delay τ_i. Staying at the maximum via this technique is called delay tracking. We can calculate what is required if we want to stay within 1% of the fringe maximum:

$$\frac{\sin(\pi \cdot \Delta\nu \cdot \tau_g)}{\pi \cdot \Delta\nu \cdot \tau_g} \approx 1 - \frac{(\pi \cdot \Delta\nu \cdot \tau_g)^2}{6} \geq 0.99, \tag{2.94}$$

i.e.,

$$|\Delta\nu \cdot \tau_g| \leq 0.078. \tag{2.95}$$

We want to assume a bandpass $\Delta\nu = 50$ MHz and $\tau_g = D/c \cdot \sin\vartheta \approx D/c \cdot \vartheta$. For a baseline of $D = 1$ km the above condition is fulfilled for $|\vartheta| \leq 1.6'$. This already shows that if we want to ensure coherence over a larger hour-angle range, it is necessary to make use of delay tracking. We can calculate the necessary delay based on the speed of the Earth's rotation (observation performed at the equator). For any case, our aim is to stay within 1% of the fringe maximum, meaning $|\Delta\nu \cdot \tau_g| \leq 0.078$.

VLA (D-Configuration) The VLA in D-configuration has a maximum baseline of $D \approx 1$ km. We assume a bandwidth of $\Delta\nu = 50$ MHz, meaning the geometric delay is $\tau_g \leq 1.6$ ns, corresponding to an angle at the sky of $\vartheta \leq 1.6'$. With the Earth's rotation of $\omega_E = 7 \cdot 10^{-5}$ rad s^{-1} = 14.4″ s^{-1}, which implies that τ_i needs to be adjusted every 7 s.

VLA (A-Configuration) Repeating the same calculation for the VLA, just in A-configuration, only the biggest baseline changes to $D = 30$ km, and consequently $\vartheta \leq 3.2''$. This means that the artificial delay τ_i needs to be adjusted every 0.22 s.

VLBA In the case of a global interferometer, or VLBI, the given conditions will become more stringent, as one can imagine. Here we have $D = 8600$ km. We assume a bandwidth of $\Delta\nu = 2$ MHz, leading to $\tau_g \leq 39$ ns, corresponding to $\vartheta = 0.3''$. This requires an adjustment of the artificial delay τ_i every 0.021 s.

Spatial Frequencies in Interferometry

The spatial frequency is the reciprocal of a full wave period in a certain space. In interferometry we want to approach this value from a different perspective. We consider a target as usual at position ϑ, close to the reference position ϑ_0, thus the following is true:

$$\vartheta = \vartheta_0 - \vartheta', \tag{2.96}$$

where ϑ' is very small so that $\sin(\vartheta') \approx \vartheta'$. We are familiar with the proportionality to the received power for an antenna:

$$\cos(2\pi \cdot \nu_0 \cdot \tau) \approx \cos\left\{2\pi \cdot \nu_0 \cdot \left[\frac{D}{c} \cdot \big(\sin(\vartheta_0) - \vartheta' \cdot \cos(\vartheta_0)\big) - \tau_i\right]\right\}, \tag{2.97}$$

where $\tau = \tau_g - \tau_i$. Here we made use of the trigonometric relation $\sin(\alpha + \beta) = \sin(\alpha)\cos(\beta) + \cos(\alpha)\sin(\beta)$. From delay tracking we know that we need to adjust the artificial delay such that $\tau_i = \tau_g(\vartheta_0) = \frac{D}{c} \cdot \sin(\vartheta_0)$ so that $\tau = 0$ in the direction ϑ_0 (the reference position). We now define:

$$u = \nu_0 \cdot \frac{D}{c} \cdot \cos(\vartheta_0) = \frac{D}{\lambda_0} \cos(\vartheta_0). \tag{2.98}$$

The defined quantity u, we call the spatial frequency, normalized by the wavelength λ_0.

Further, putting

$$\xi' = \sin(\vartheta') \approx \vartheta' \tag{2.99}$$

we can write the fringe pattern (valid for close to $\tau = 0$) as

$$F(\xi') = \cos(2\pi \cdot u \cdot \xi'). \tag{2.100}$$

As we have learned from the convolution theorems, this fringe pattern becomes the response of an interferometer to a point source at position $\vartheta = \vartheta_0 - \vartheta'$, when the net delay is $\tau_g - \tau_i = 0$ (for $\vartheta = \vartheta_0$). Because ξ' is also measured in radians, the spatial frequency u is measured as the number of oscillations per radian (assumed ϑ' is small).

Here we see that the definition of the spatial frequency is analogous to the classic frequency that we know from acoustics or electronics,

$$\begin{aligned} F(t) &= \cos(2\pi \cdot \nu \cdot t) \qquad \nu = \text{frequency, oscillations per second} \\ F(\xi') &= \cos(2\pi \cdot u \cdot \xi') \qquad u = \text{spatial frequency, oscillations per radian.} \end{aligned} \tag{2.101}$$

2.4.3 Aperture Synthesis by Radio Interferometric Arrays

The Concept of (u, v)-Coverage

On multiple occasions in the previous chapters, we worked with the Fourier transforms. In particular, we learned that the Fourier transform of the brightness distribution $B(\xi, \eta)$ is the visibility function $V(u, v)$. This is of great importance in radio interferometry, because it allows us to obtain knowledge about the brightness distribution by the inverse Fourier transformation of $V(u, v)$

$$B(\xi, \eta) = \iint V(u, v) \cdot e^{-i2\pi \cdot (u \cdot \xi + v \cdot \eta)} \, \mathrm{d}u \, \mathrm{d}v. \tag{2.102}$$

With a sufficient number of baselines we can probe multiple visibilities for different (u, v)-positions to find out more about the brightness distribution $B(\xi, \eta)$. In our examples we use only two telescopes for illustrative purposes, but one can imagine that this process of collecting visibility measurements for various (u, v)-positions - hence varying baselines $\vec{D}_\lambda$ - can be very time consuming. Consequently, we

can only perform observations where the brightness distribution $B(\xi,\eta)$ of the target is constant with time i.e. there are no changes in morphology or flux levels.

At this point it should be clear that interferometers should consist of as many antennas as possible to cover a multitude of measurements within the (u,v)-space at once. We also know that the baseline vectors $\vec{D}_\lambda^{k,j}$, where k,j denotes the baseline between the antennas k and j, have their base at the (u,v)-space origin $(0,0)$. So we want to avoid having the same distance between different pairs of antennas, since they would cover the same position in (u,v)-space and will not contribute any further information. We will further emphasize this point in the following.

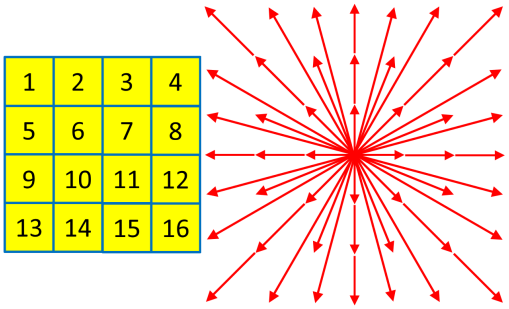

Figure 2.12: The left part of the image shows 16 antennas arranged in a strict grid. The right part of the image shows all possible connections between any two antennas in the grid. Many of them have the same orientation/length and therefore represent the same baseline (e.g. the baseline 2 -> 8 is identical to 5 -> 11).

(u,v) Plane and Redundancy Assume a perfectly equidistant gridded layout of 16 antennas. Measuring the aperture distribution of any two antennas power (which we know is the visibility) is the principle of aperture synthesis. The resulting baselines $\vec{D}_\lambda^{k,j}$ span a (u,v)-plane coverage which always is point-symmetric because any baseline vector between antenna k and j can also be represented by its antiparallel vector from antenna j to k.

It is obvious though that the visibilities for the baselines $\vec{D}_\lambda^{k,j}$ and $\vec{D}_\lambda^{j,k}$ carry the same information although having different points in the (u,v)-plane and therefore carry a redundancy that cannot be removed by placing the antennas in a certain pattern. This means that this redundancy is present in any interferometer and is therefore removed on the data level. We therefore want to ignore the point-symmetric counterparts from now on in our considerations. However, the usual depiction of the covered (u,v)-plane, also called (u,v)-plot, does show the redundant point symmetric counterparts!

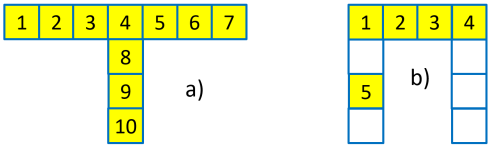

Figure 2.13: More advanced antenna configurations. With the arrangement in a), fewer antennas are needed to achieve the same number of baselines as in Fig. 2.12. If one of the antennas is movable, even fewer antennas are needed for the same coverage, as shown in b).

Calculating all possible combinations of baselines for an array with n elements, the number of baselines is normally $n \cdot (n-1)/2$. In our example of 16 antennas, this leads to 120 individual baselines (again, neglecting the point symmetric counterparts). This leads to 120 correlated powers of the form

$$P = \sum_{j=1}^{n-1} \sum_{k=j+1}^{n} E_j \cdot E_k \cdot \cos(\psi_j - \psi_k). \tag{2.103}$$

Checking the vector diagram in Fig. 2.12, we realize that 24 products are already sufficient to represent all produced baselines, when removing all aforementioned redundancies.

Being aware of the redundancies, we can optimize the setup to a T-configuration (see Fig. 2.13), shown in a) with only 10 antennas, instead of 16, to reproduce all baseline vectors as before. If we know that our source is not time-variable and we therefore have some time to move one antenna to a different position, we even can reduce the set up to only 5 antennas shown in b), where antenna 5 is movable to any of the blue square positions. M. Ryle and A. Hewish made use of this at Cambridge to carry out the first of the famous Cambridge surveys of radio sources, the 1C survey.

Baseline Changes During Observation The arrangement considerations were mostly carried out in a static context with no movement taking place between instrument and observation target. In reality this would not be the case. The interferometer array, mounted on the ground, will rotate with Earth's rotation with respect to the observation target, consequently changing the baseline vector in the rest frame of the target.

This rotation of the vector represents a track in the (u, v)-plane, drawn by the change of the vector. The longer the observation, the further around the (u, v)-space origin the track progresses. You can see a (u, v)-plot of a 4 hour observation performed by LOFAR with 64 antennas corresponding to 2016 unique tracks by various baselines. In the plot, we can also see the point-symmetric redundancies, giving 4032 tracks in total. In principle, any movement of the baseline vectors

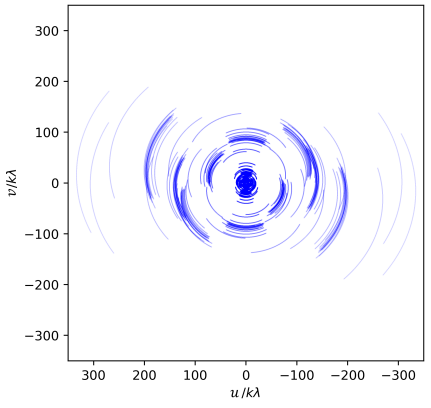

Figure 2.14: A (u, v)-plot shows individual visibility measurements as blue dots over the entire observation period. As the Earth rotates, these dots follow ellipses.

during observation does improve the (u, v)-coverage, but it is easier to make use of the Earth's rotation which we get for free. Knowing the redundancy issues present in such arrays, we can improve our interferometer measurements and achieve better (u, v)-coverage by:

- avoiding periodicities in the arrangements
- implementing as many antennas as possible
- observing for as long as possible (ideally >12 hours)
- repeating the measurements with another arrangement (rarely possible)

Simple Configurations and Transit Arrays

With what we have learned in previous sections, we can start to explore different interferometer configurations. We will start by looking at more simple, smaller scale arrays and then advance to studying more complex implementations on larger scales. We will discuss designs used in the past and more modern arrangements, along with their respective advantages and flaws.

Transit-Interferometers Different versions of transit interferometers were frequently used in the past (mainly in the 50's and 60's), for (comparatively) high resolution radio surveys. They observed the sky, as it was passing by due to Earth's rotation – hence the name "transit" interferometers. The flaw in this design came from its inability to observe the source for longer than its transit time across the visible sky; if more sensitive measurements were required then one would have to wait until the following night to observe again. Nonetheless, these arrays constituted a considerable contribution to the radio data collected at the time due to their widespread use and partial success.

Mills' Cross One early array designed by B.Y. Mills in 1954 consisted of two arrays of antennas arranged in a cross; one arm was oriented in a north-south direction and the other in the east-west direction. The resolution of each array was good in its direction of orientation but poor in the perpendicular direction, resembling a fan beam. When both signal outputs were combined, for example,

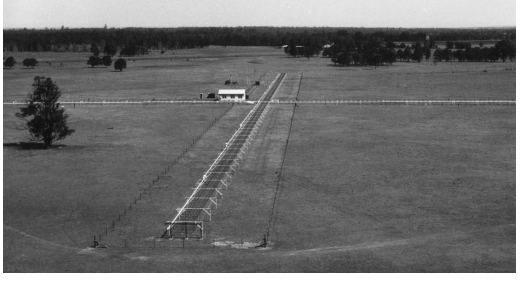

Figure 2.15: The Mills' Cross at the Fleurs field station in 1954. Credit: Courtesy of CSIRO Radio Astronomy.

in a multiplier, the resulting resolution capabilities could be described by a pencil beam. Note that the array elements, while being cross correlated, cannot be cross correlated in the central region because here the elements overlap geometrically. This leads to a depression in the beam center. Introducing phase shifts for each element in the array, a sweep across the meridian can be performed, called electronic steering.

T-Configurations As previously discussed in the (u, v)-coverage section, if we have an antenna arrangement such that symmetries are present, then some baseline vectors will become redundant. This is clearly the case for the Mills cross type. We can significantly increase (u, v)-coverage by shifting one arm of the cross so that we end up with a T-shape array. This conserves resolution capabilities (meaning the longest baselines remain the N-S and E-W arms), but reduces redundancy in the (u, v)-plane (fewer baseline vectors doubling). With the same number of array elements we attain a denser (u, v)-plane coverage, which is always beneficial in image reconstruction. However, these T-shaped arrangements, mainly used in the early 60's, were limited in capabilities compared to now. They were much more sensitive to phase inaccuracies than cross-type telescopes, even though cross-types had a higher degree of symmetry, simply because of the low quality phase switched receivers available at the time. The Cambridge One-Mile Telescope (1965) was a famous T-shaped interferometer, with three antennas fixed along an east-west baseline and a movable antenna in north-south. This interferometer carried out the famous 3C radio survey; the targets detected during this survey still have "3C" in their names. Because of the nature of the early interferometers used, if a target has a 3C association it is a definite indication that it is a bright radio source.

Linear Antenna Groups Another straightforward arrangement is a simple line of antennas. Assuming four antennas equally spaced in a line (see Fig. 2.17), connected via cables of same length to a voltage combiner, the voltage combiner adds the individual inputs such that the total output is given by

$$U = \langle (U_1 + U_2 + U_3 + ... + U_n)^2 \rangle \qquad (2.104)$$

where U_n is the voltage of the n-th element. We can describe the distance between array elements as l_λ in units of the observation

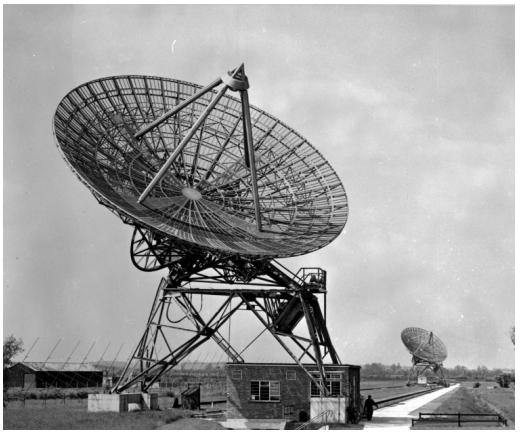

Figure 2.16: The One-Mile telescope in Cambridge in 1962, which recorded the data for the 3C catalog. Credit: CSIRO.

wavelength λ. Assuming a radiating distant object at position ϑ away from the zenith, the signal is in phase at any two elements when

$$\varphi = 2\pi \cdot l_\lambda \cdot \sin(\vartheta) = n' \cdot 2\pi \qquad n' = 0, 1, 2, 3, 4, \ldots \tag{2.105}$$

thus we can determine the location of the object with the maxima of the side lobes to be

$$\vartheta = \arcsin\left(\frac{n'}{l_\lambda}\right). \tag{2.106}$$

This arrangement is also known as a phased array and suffers from strong side lobes due to the symmetry of the elements. It is possible to move the interference maxima on the sky by adding phaseshifters to the elements and thus electronically steer it, which is another application of the shift theorem.

Considering all cross correlations of the antennas between the voltages $U_\mathrm{m} \cdot U_\mathrm{n}$ of all pairs, we receive all terms as in the voltage combinator given above, except for the quadratic ones where m = n. This represents the spatial frequencies in the origin of the (u, v)-plane and has therefore no influence on the directivity of such an antenna group. This demonstrates that measurements with correlated antenna groups are much faster than those with a phased array. An example of such a linear antenna group is the the One-Mile Telescope at Cambridge, which performed the 3C survey; it had two stationary antennas and one movable one (see Fig. 2.16).

Tracking Arrays and Earth-Rotation Synthesis

As we saw in the previous sections, transient arrays have inherent disadvantages in integration times during observations. If the array relies on the Earth's rotation to slew the target of interest across the antenna beam, the integration time of the source is fixed during a sidereal day. Longer exposure times to increase sensitivity can only be achieved by stacking data from multiple days where important time-dependent information could be lost. Shorter exposure times, which could be desirable for surveys to improve telescope performance, also cannot be implemented. These issues could be solved if the beam from the telescope could be steered to track targets. In the following, we will highlight this technical implementation in radio astronomy.

Earth-Rotation Synthesis When observing, the rotation of the Earth during the observation time must also be considered when tracking the target. Previously, we discussed the influence of baseline vectors on the (u, v)-plane and how it is tracing

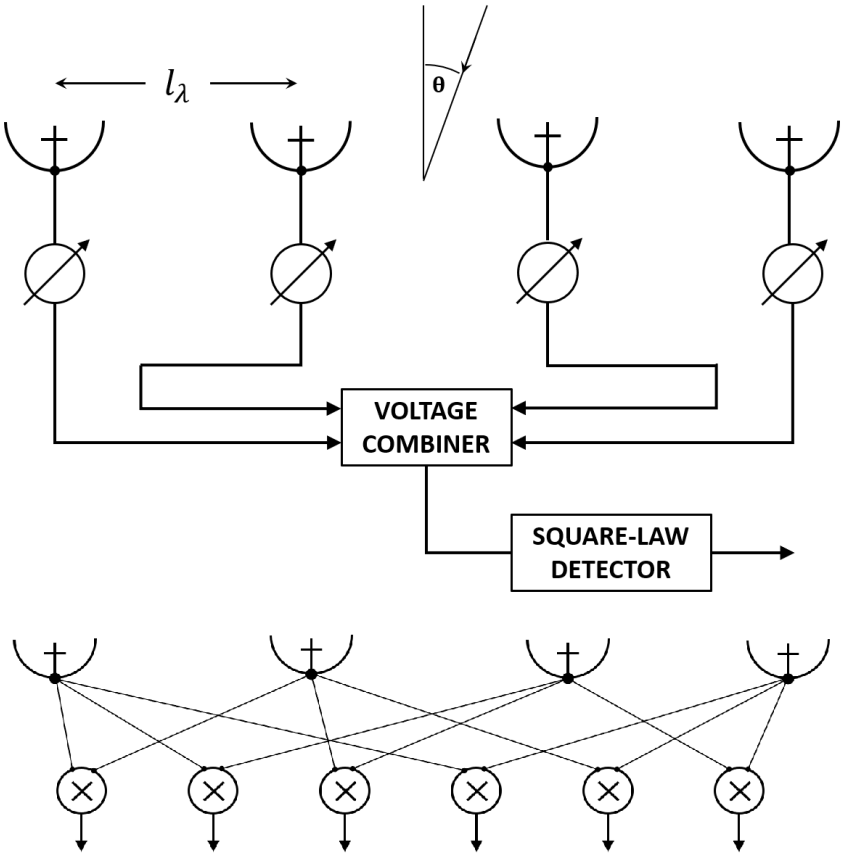

Figure 2.17: Four telescopes arranged along a simple line are called a phased array. They pick up a signal that is mixed in a voltage combiner. The cable connecting the telescopes to the analyser is all the same length.

ellipses in the (u, v)-plane. The underlying principle was first described by M. Ryle (1962); he was awarded the Nobel Prize for it in 1974. Today it is commonly known as "Earth rotation synthesis". To visualize this method, imagine a simple array consisting of two antennas arranged along an east-west baseline, with a target of interest located on the axis of Earth's rotation in the distance (see Fig. 2.18).

As the Earth rotates, the baseline vector $\vec{D}_\lambda$ also rotates with respect to the observation target. The Fourier transform of the baseline into the (u, v)-plane yields a circle around the origin with radius $r_{(u,v)} = |\vec{D}_\lambda|$. Comparing the figure, at an hour angle of −6 h the baseline vector shows only one component in the v direction, while at an hour angle of 0 h only the u direction shows the maximum value. It can also be seen that due to the two possible permutations of the two telescopes, only an observation time of 12 hours is needed to cover the entire track in the (u, v)-plane. While only half of the permutations are already sufficient to collect all available information. Thus,

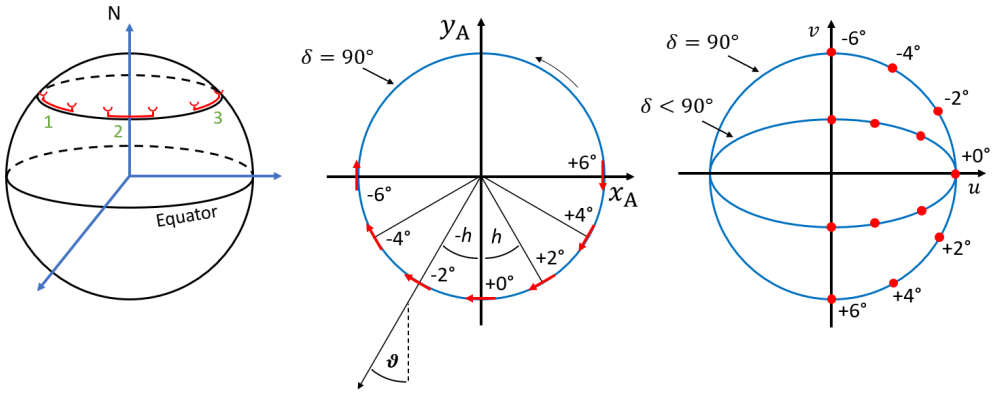

Figure 2.18: The two telescopes rotate together with the Earth, from position 1 to position 3 (left). Therefore, their baselines will rotate in a similar way. Within twelve hours the baseline occupies all possible orientations it can have in the x_A, y_A plane (center). Note that the direction of the baseline is arbitrary. During this time the track is completed in the (u, v)-plane. However, this orbit is only circular if both telescopes are at the equator ($\delta = 90°$). At any other declination the (u, v)-coverage will appear as an ellipse.

this relation shows a Hermitian property of the visibilities, i.e. $V(u,v) = V^\star(-u,-v)$.

Assuming that the target is not at the declination $\delta = 90°$ but at $\delta < 90°$, which is usually the case, the components of the baseline vector will show ellipses around the origin when Fourier transformed into the (u, v)-plane. These will be more extreme the farther the target is from the axis of rotation.

One-Dimensional Tracking Arrays After highlighting the properties of a two-element array while performing Earth-rotation synthesis, we want to consider a linear tracking array of arbitrary length. The individual N elements shall be equally spaced with separation d_λ, which are called grating interferometers. The total length can thus be calculated via $(N-1)\cdot d_\lambda$ for $N > 2$ (see Fig. 2.19). Via Fourier theorems and some basic Fourier transform pairs the following is true

$$\sum_{n=-N}^{+N} \delta(u - n\cdot d_\lambda) \quad \overset{\mathscr{F},\mathscr{F}^{-1}}{\Longleftrightarrow} \quad \frac{\sin[(2N+1)\cdot\pi\cdot d_\lambda\cdot\xi]}{\pi\cdot d_\lambda\cdot\xi} \star \sum_{m=-\infty}^{+\infty} \delta\left(\xi - \frac{m}{d_\lambda}\right), \tag{2.107}$$

where δ describes the delta function. On the left of the equation we see the delta functions which describe the spacings in the u domain, also interpreted as transfer- or spectral sensitivity function. The array is of discrete length but can be described mathematically as an infinite amount of delta functions multiplied with a box function to "cut" it to the appropriate size. This perspective makes it easier to understand the Fourier transform. On the right-hand side we see the beam pattern in which the Fourier transform of the box function is replicated by convolution with delta functions

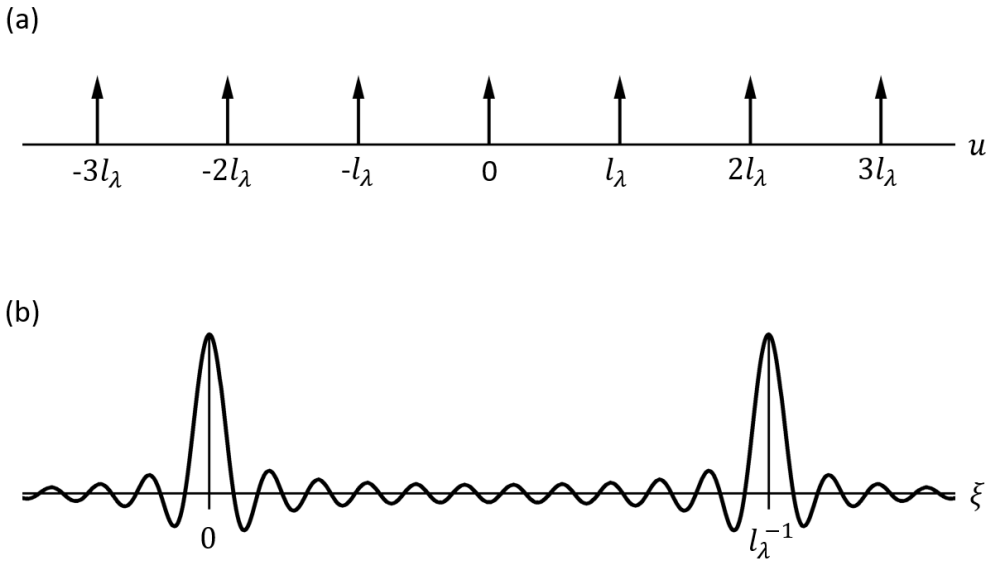

Figure 2.19: (a) shows multiple Dirac peaks along the u-axis, each with a distance l_λ to its neighbor. Their Fourier transform is shown in (b). The basic Fourier transform of a box function is the $sinc$ function. However, since the spacing between the peaks is identical, the Fourier transform has only two prominent $sinc$ peaks: at zero and at l_λ^{-1}. In practice, this arrangement of antennas would reduce the side lobes of the telescope array.

in the far field domain. Remember that Fourier-transformed series of delta functions are also a series of delta functions if those series are infinite. The Fourier transform of a box function is a sinc function. We can illustrate this visually in the following way, assuming that the aperture size is a box function. If the aperture size of each element increases, the sinc function of its Fourier transform approaches a delta function again. This means that side lobes (introduced by the sinc functions) can be reduced by increasing aperture sizes, but the side lobes will never disappear completely because of technical limitations. To do so mathematically, the aperture size must be equal to the distance between the elements. For obvious reasons, the distance between the elements is much bigger than the aperture size.

Minimum Redundancy As we have discussed in the previous chapters, symmetric arrays introduce redundancies because traces in the (u, v)-plane are covered multiple times without introducing additional information. This is not always disadvantageous, as there are uncertainties and sources of noise in the experiments, which means that multiple measurements of the same value leads to a more accurate result. But nowadays with more reliable electronics this benefit is of decreasing importance, so it is desirable to keep the redundancy to a minimum.

Figure 2.20: Schematic of the linear WSRT array. The first group of dishes (from left to right) are stationary, while dishes A, B, C and D are movable on tracks to create different baselines with desired properties.

Movable Antennas While one solution for decreasing redundancy in the array baselines and increasing (u, v)-coverage is to increase stationary elements at various, non-repetitive distances, a much cheaper approach is to have multiple stationary elements and one or more movable elements. The first interferometer implement this technique was the One-Mile Telescope at Cambridge.

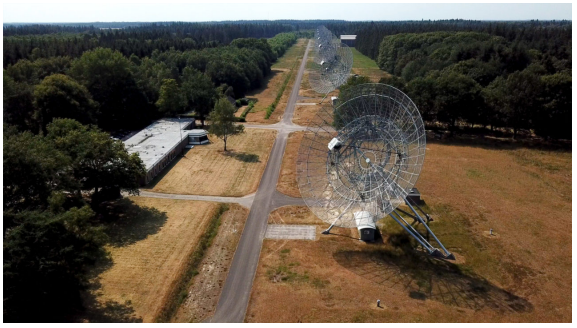

Figure 2.21: Aerial view of the WSRT in Westerbork. Credit: ASTRON

The Westerbork Synthesis Radio Telescope (WSRT) is another interferometer of a larger scale which uses this technique and is still in operation. It has 14 elements in total: ten stationary elements arranged in a straight, east-west line with inter-antenna spacings of 144 m and a further four elements that are movable. Two of the movable antennas are closer to the larger group and can move in a 300 m line and the other two are further away and can move in a 180 m line; see diagram in Fig. 2.20.

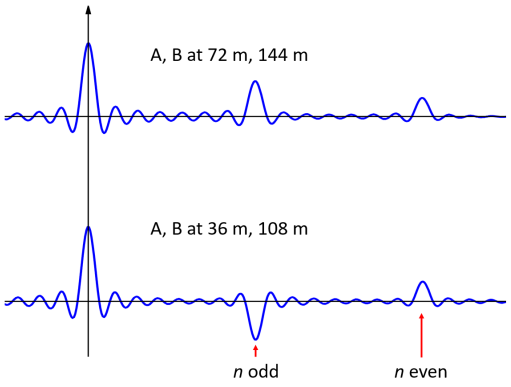

Figure 2.22: This graph shows the beam shape of a measurement with the WSRT in two different configurations. Changing the position of the four movable telescopes (A, B, C, D) changes the beam of the telescope array. By taking two measurements and adding the data together, some of the unwanted side lobes (the smaller peaks) are removed.

One way of using the movable arrays to our advantage is to place antennas A and B at positions 72 m and 144 m away from the stationary group for the first observation,

and then at positions 36m and 108m away for a second observation. In the second observation the odd numbered side lobes are inverted with respect to the first observation which allows us to easily remove them upon summation of both observations. An aerial footage photograph of the WSRT interferometer is shown above.

Two-Dimensional Tracking Arrays Up to this point we understand that an interferometer should be arranged two dimensionally to improve the (u, v)-coverage. To provide equally balanced capabilities in any direction, it is advisable to have both the north-south and east-west directions be of similar length and equally spaced. Geographically, it is optimal to place the array at medium latitudes, e.g., Europe, to have the best sky coverage. The equivalent is true for the southern hemisphere of course. Locations in Europe allow for observations down to declinations of $\delta = -30°$, which is roughly a factor 3 more in sky coverage than an interferometer that is purely east-west oriented. Unfortunately, calculating the optimum coverage of the (u, v)-plane with a given amount of elements is much more complicated than for one dimensional arrays. All array configurations are based on empirical solutions (simulations mostly). Taking two linear arrays and calculating the minimum redundancy for each of them and cross-correlating is not equivalent to a two dimensional array with minimum redundancy!

We want to highlight the "Karl G. Jansky Very Large Array" (VLA) in this scope, which is located in Socorro, New Mexico. It was built in 1980 and is still, to this day, an important instrument for the astronomical science community. The interferometer has 27 single-dished elements, each with a diameter of 25 m. About 40,000 correlators for the 351 simultaneous baselines are used, with the elements oriented in an upside-down "Y" configuration. The distance in each arm from one element to the other is never identical for any two pairs and can be calculated via the following equation

Figure 2.23: Aerial view of the VLA telescope in New Mexico (USA) in the most compact D-configuration. Credit: NRAO

$$R_n \propto n^{\alpha} \quad \text{with} \quad \alpha = 1.716 \quad \text{i.e.} \quad \frac{R_n}{R_m} = \left(\frac{n}{m}\right)^{1.716}, \tag{2.108}$$

where R_n is the distance from the array center to the n-th element. Furthermore, the upside-down "Y" configuration is rotated by 5° with respect to the north-south direc-

tion, to avoid pure east-west spacings between telescopes in the two southern arms. This would otherwise lead to poorer angular resolution for sources that have lower declinations δ in the sky. The individual elements can also be moved to different locations. There are four configurations designed for observation: configuration A, with 36,4 km; B, with 11.3 km; C, with 3.4 km and D, with 1.03 km with the shortest maximum baseline length.

VLBI Arrays

One important aim of designing different arrays is to improve resolution capabilities. Observations in the radio regime have poor resolution, despite usually having bigger apertures than optical instruments. The observation wavelength is the culprit here, as shown in previous chapters. Attempts to overcome these limitations have been described in terms of different interferometer designs, like two element arrays, phased up linear arrays, two dimensional arrays, etc. It is possible to build ground-based radio telescopes because of the "radio window" in Earh's atmosphere, and this is generally preferred as space-based telescope are orders of magnitude more expensive, and this technology has only been explored relatively recently. Taking this into account, we can assume that the biggest possible ground-based interferometer would have the size of the Earth, when the elements are distributed accordingly. This immediately raises concerns for the (u, v)-plane, because we are limited in location options for the individual elements. Huge parts of Earth's surface are covered in water, and therefore cannot be considered as station locations. Also, such elements could not be connected to each other via cable as smaller interferometer arrays are, so they would need to have precise atomic clock systems with extremely phase-stable oscillators. Apart from that, each element of the array would need to have sufficient sensitivity (collective area), hour angle and declination coverage during observations. Despite the seemingly insurmountable requirements, these types of interferometers have already been implemented. They are called Very Long Baseline Interferometry (VLBI) arrays. Although these arrays usually give rather sparse (u, v)-coverage, when done correctly they have unprecedented resolution capabilities. In the following table we show a few radio telescopes and compare their observation frequencies, aperture sizes and corresponding highest possible resolution capabilities (note that radio telescopes usually have a wide range of frequency coverage with multiple receiver systems):

As we see in Table 2.1, especially in comparison to the Hubble Space Telescope's resolution capabilities in the **U**ltra **V**iolet (UV) light, it is necessary to make use of interferometer arrays in radio when comparing results across different wavelengths. This is often an important approach to study natural phenomena via so called multi-

Table 2.1: A very short list of a few representative telescopes and telescope arrays to show the effect of size and observing frequency on resolution capabilities.

Telescope	ν	$D_{\lambda,\max}$	α_{res}
Effelsberg	86 GHz	100 m (diameter)	$8.8''$
Karl G. VLA	50 GHz	36 km	$0.049''$
LOFAR	150 MHz	2000 km	$0.25''$
VLBA	86 GHz	8600 km	$0.00010''$
HST (UV light)	30 PHz	2.4 m (diameter)	$0.0010''$

In addition to the radio regime, the well-known HST operating in the optical regime has been added to further highlight the immense differences with radio telescopes.

wavelength observations. While many results in the radio regime are noteworthy in their own right, they also contribute to more complete studies across the electromagnetic spectrum and even multi-messenger studies. (Note: "messenger" in this case means the medium from which the information comes, e.g., electro-magnetic radiation, neutrinos, gravitational waves...)

So far we have focused on ground-based interferometers, but this technique can also be combined with radio satellites called space VLBI, e.g., RadioAstron. Here we can achieve even longer baselines obviously, but it is extremely difficult to correlate the data because of the huge gaps in the (u,v)-plane. These kinds of observations are also extremely dependent on weather at all ground sites simultaneously.

Antenna Separations and Geometry

In order to calculate the traces on the (u,v)-plane of a given array of telescopes, we first need to define the orientation and the reference frame. To get the whole coverage of the full array, one needs to calculate the trace in the (u,v)-plane for every pair of participating telescopes. For our definition, we want to describe the baseline vector of any two elements in a cartesian system in the Earth's frame of reference. We define the X,Y,Z axes as follows:

X towards $h = \quad 0^h, \delta = 0°$

Y towards $h = -6^h, \delta = 0°$

Z towards $\delta = 90°$,

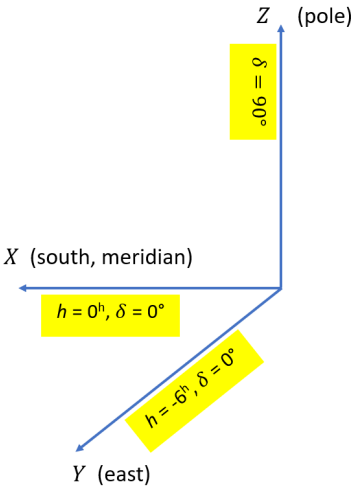

Figure 2.24: Coordinate system of the Earth. It is used to define the positions of the telescopes in relation to each other. Due to the rotation of the Earth, this coordinate system cannot be used to describe objects in the sky.

where h is the hour angle and δ is the declination of the phase-reference position of the baseline. This coordinate system is fixed to the Earth's sphere. Note that the coordinate system of (u, v, w) is fixed to the sky. The relative separation between any two elements (the baseline) at a geographic latitude ϕ can then be described in relation to the elevation E and the azimuth A as:

$$\begin{bmatrix} L_x \\ L_y \\ L_z \end{bmatrix} = D \cdot \begin{bmatrix} \cos\phi \cdot \sin E - \sin\phi \cdot \cos E \cdot \cos A \\ \cos E \cdot \sin A \\ \sin\phi \cdot \sin E + \cos\phi \cdot \cos E \cdot \cos A \end{bmatrix}. \tag{2.109}$$

With a new baseline, the values of E, A and D are determined by surveying techniques. Another useful relation is the separation of the elements from the declination δ_D and right ascension α_D that the baseline vector $\vec{D}_\lambda$ is pointing at:

$$\begin{bmatrix} L_x \\ L_y \\ L_z \end{bmatrix} = D \cdot \begin{bmatrix} \cos\delta_D \cdot \cos\alpha_D \\ -\cos\delta_D \cdot \sin\alpha_D \\ \sin\delta_D \end{bmatrix}. \tag{2.110}$$

The transformation between the cartesian system to the (u, v, w)-system can be calculated via:

$$\begin{bmatrix} u \\ v \\ w \end{bmatrix} = \frac{1}{\lambda} \cdot \begin{bmatrix} \sin h & \cos h & 0 \\ -\sin\delta \cdot \cos h & \sin\delta \cdot \sin h & \cos\delta \\ \cos\delta \cdot \cos h & -\cos\delta \cdot \sin h & \sin\delta \end{bmatrix} \cdot \begin{bmatrix} L_x \\ L_y \\ L_z \end{bmatrix}, \tag{2.111}$$

here the matrix elements are the directional cosines of the (u, v, w) with respect to the defined cartesian axes. In most cases the w direction in (u, v, w) space can be neglected due to the relatively small variation. Hence for u we obtain:

$$u = \frac{1}{\lambda} \cdot (\sin h \cdot L_x + \cos h \cdot L_y), \tag{2.112}$$

and similarly for v:

$$v = \frac{1}{\lambda} \cdot (-\sin\delta \cdot \cos h \cdot L_x + \sin\delta \cdot \sin h \cdot L_y + \cos\delta L_z), \tag{2.113}$$

which we can rewrite as

$$\frac{v - \cos\delta \cdot \frac{L_z}{\lambda}}{\sin\delta} = \frac{1}{\lambda} \cdot (\sin h \cdot L_y - \cos h \cdot L_x). \tag{2.114}$$

Squaring the equations for u and v, adding them, and using some trigonometric relations we obtain:

$$u^2 + \left[\frac{v - \left(\frac{L_z}{\lambda}\right) \cdot \cos\delta}{\sin\delta} \right]^2 = \frac{L_x^2 + L_y^2}{\lambda^2}. \tag{2.115}$$

In this equation we directly see the ellipse equations that are seen in the (u, v)-spaces drawn during observation due to Earth's rotation. Interestingly, we also see that if L_z is non-zero, there must be two ellipses in the (u, v)-plane.

2.4.4 Image Reconstruction

Receiver Response

Interferometer Sensitivity Before observation, for any telescope, it is important to know if the instrument is able to detect the target of interest at all for that the SNR needs to be calculated. Usually single dish radio telescopes, measure the signal of an object as the antenna temperature T_A, while the noise is given by the *radiometer equation*:

$$\Delta T = \frac{C \cdot T_\mathrm{sys}}{\sqrt{\Delta\nu \cdot \tau}}, \tag{2.116}$$

where C is a dimensionless constant (depending on the receiver system), T_sys is the system temperature, $\Delta\nu$ is the bandwidth and τ is the integration time. Radio interferomenters measure the signal of a target of interest via the brightness distribution $B(\xi, \eta)$ that contains the Fourier integral of the measured visibility $V(u, v)$:

$$B(\xi, \eta) = \int_{-\infty}^{\infty} \int_{-\infty}^{\infty} V(u, v) \cdot e^{i \cdot 2\pi \cdot (u \cdot \xi + v \cdot \eta)} \mathrm{d}u \, \mathrm{d}v. \tag{2.117}$$

Interferometers introduce noise by the uncertainty of the visibility function $V(u, v)$. In order to attribute a definite noise for the the SNR, it is important to understand the propagation of uncertainty introduced by the visiblity function to the brightness distribution $B(\xi, \eta)$. During observation, electronics, when measuring signals, sample the data such that the visibility function is not continuous, but discrete. This also means that the (u, v)-tracks are not continuous lines but rather points in the (u, v)-plane. With the integration time of individual samples, τ_a, the total integration time τ_0 and the total number of antennas n_a, we can calculate the number of measured visibilities n_d to be:

$$n_\mathrm{d} = n_\mathrm{p} \cdot \frac{\tau_0}{\tau_\mathrm{a}}, \tag{2.118}$$

with

$$n_\mathrm{p} = \frac{n_\mathrm{a} \cdot (n_\mathrm{a} - 1)}{2}. \tag{2.119}$$

n_p is the number of individual two-element interferometers in the whole array. While the whole coverage of the (u,v)-space would allow us to restore the true brightness distribution $B(\xi,\eta)$, it is impossible to realize this. Any measurement will only provide a certain coverage of the (u,v)-space. Because of the missing information, the restored brightness distribution $B^D(\xi,\eta)$ will have flaws and is therefore called "dirty image". With the coverage in the (u,v)-plane at discrete (u_k,v_k) locations, the brightness distribution is given by the discrete Fourier transform

$$B^D(\xi,\eta) = C \cdot \sum_{k=0}^{2\cdot n_d} V(u,v)\cdot S(u,v)\cdot e^{i\cdot 2\pi\cdot(u\cdot\xi+v\cdot\eta)}, \tag{2.120}$$

where $C = \dfrac{1}{2\cdot n_d+1}$ as a normalization constant and $S(u,v)$ as the sampling function as:

$$S(u,v) = \sum_{k=0}^{2\cdot n_d} \delta^2(u-u_k, v-v_k). \tag{2.121}$$

It acts like a mask, where visibility values at the (u,v)-position are multiplied by 1 if a measurement was made at that position in the (u,v)-space, otherwise the visibility is multiplied by 0.

Additionally, it is important to introduce the weighting functionality, which is used in the imaging procedure, to suppress side lobes of the beam. Furthermore, this is used to control differences introduced in heterogeneous arrays, where individual stations have different collecting areas A_{eff}, and different receivers with different system temperatures T_{sys}, integration times τ_a , and frequency bandwidths $\Delta\nu$. The weights can be written as:

$$W(u,v) = \sum_{k=0}^{2\cdot n_d} R_k\cdot T_k\cdot D_k\cdot\delta^2(u-u_k, v-v_k), \tag{2.122}$$

where R_k is a factor to represent differences in telescope properties, T_k is a taper to control the beam shape and D_k is a density weight of measured visibilities. Introducing these weights, equation (2.120) can be adjusted to be:

$$B^D(\xi,\eta) = C \cdot \sum_{k=0}^{2\cdot n_d} V(u,v)\cdot S(u,v)\cdot W(u,v)\cdot e^{i\cdot 2\pi\cdot(u\cdot\xi+v\cdot\eta)}. \tag{2.123}$$

This can be rewritten via:

$$\begin{aligned} V_k &= V(u,v)\cdot S(u,v) = \Re V_k + i\cdot\Im V_k \\ W_k &= W(u,v) \end{aligned} \tag{2.124}$$

and taking into account that no measurement at k = 0 can be made, such that any term for $B^{\mathrm{D}}(\xi,\eta)$ at the center in the (u,v)-plane vanishes, leading to:

$$\begin{aligned} B^{\mathrm{D}}(\xi,\eta) &= C \cdot \sum_{\mathrm{l}=1}^{2\cdot n_{\mathrm{d}}} V_{\mathrm{k}} \cdot W_{\mathrm{k}} \cdot e^{i\cdot 2\pi\cdot(u_{\mathrm{k}}\cdot\xi + v_{\mathrm{k}}\cdot\eta)} \\ &= 2\cdot C \cdot \sum_{\mathrm{l}=1}^{n_{\mathrm{d}}} W_{\mathrm{k}} \cdot [\Re V_{\mathrm{k}} \cdot \cos(2\pi\cdot(u_{\mathrm{k}}\cdot\xi + v_{\mathrm{k}}\cdot\eta)) - \Im V_{\mathrm{k}} \cdot \sin(2\pi\cdot(u_{\mathrm{k}}\cdot\xi + v_{\mathrm{k}}\cdot\eta))] \end{aligned} \tag{2.125}$$

Note that the two additional terms $\Re V_{\mathrm{k}} \cdot \sin[2\pi\cdot(u_{\mathrm{k}}\cdot\xi + v_{\mathrm{k}}\cdot\eta)]$ and $\Im V_{\mathrm{k}} \cdot \cos[2\pi\cdot(u_{\mathrm{k}}\cdot\xi + v_{\mathrm{k}}\cdot\eta)]$ vanish under the integral of $B(\xi,\eta)$ and can therefore also be neglected for the sum of $B^{\mathrm{D}}(\xi,\eta)$.

Positioning a point source in the phase center $(\xi = 0, \eta = 0)$ means a constant visibility value at any position in the (u,v)-plane. Any present noise can be determined easily by the variations to the constant value. With $\xi = \eta = 0$, the $\sin[2\pi\cdot(u_{\mathrm{k}}\cdot\xi + v_{\mathrm{k}}\cdot\eta)] = 0$ and $\cos[2\pi\cdot(u_{\mathrm{k}}\cdot\xi + v_{\mathrm{k}}\cdot\eta)] = 1$. With this, the dirty image in the phase center is given by:

$$\begin{aligned} B^{\mathrm{D}}(0,0) &= 2\cdot C \cdot \sum_{\mathrm{k}=1}^{n_{\mathrm{d}}} W_{\mathrm{k}} \cdot \Re V_{\mathrm{k}} \\ &= 2\cdot C \cdot \sum_{\mathrm{k}=1}^{n_{\mathrm{d}}} W_{\mathrm{k}} \cdot S_{\mathrm{k}} \\ &= 2\cdot C \cdot S \cdot \sum_{\mathrm{k}=1}^{n_{\mathrm{d}}} W_{\mathrm{k}}, \end{aligned} \tag{2.126}$$

with the total flux density $S = S_{\mathrm{k}} = \Re V_{\mathrm{k}} = \Re V$. Because the point source must be restored in the dirty image, the total flux density must be contained in the phase center here as well:

$$B^{\mathrm{D}}(0,0) = S, \tag{2.127}$$

which means that the normalization factor needs to be:

$$C = \frac{1}{2\cdot\sum_{\mathrm{k}=1}^{n_{\mathrm{d}}} W_{\mathrm{k}}} \tag{2.128}$$

Introducing the uncertainty for the flux density as $\Delta S_{\mathrm{k}} = \Delta S =$ **const.**, the noise in the dirty image is:

$$\Delta B^{\mathrm{D}} = 2\cdot C\cdot\Delta S\cdot\sqrt{\sum_{\mathrm{k}=1}^{n_{\mathrm{d}}} W_{\mathrm{k}}^2} \tag{2.129}$$

This can be further simplified when assuming an array of n_{a} identical telescopes ($R_{\mathrm{k}} = 1$) with naturally weighted visibilities ($D_{\mathrm{k}} = 1$) and an untapered beam ($T_{\mathrm{k}} = 1$) to:

$$\Delta B^{\mathrm{D}} = \frac{\Delta S}{\sqrt{n_{\mathrm{k}}}} \tag{2.130}$$

Since $S = \Re V = \Re V_{\mathrm{k}}$, the uncertainty of the flux density ΔS is given by the rms noise σ_{V} of the measured visibilities which is, based on the radiometer equation, given by

$$\sigma_{\mathrm{V}} = \frac{\sqrt{2} \cdot k_{\mathrm{B}} \cdot T_{\mathrm{sys}}}{A_{\mathrm{eff}} \cdot \eta_{\mathrm{Q}} \cdot \sqrt{\Delta\nu \cdot \tau_{\mathrm{a}}}}, \tag{2.131}$$

with k_{B} as the Boltzmann constant and the analog-digital quantization efficiency

$$\eta_{\mathrm{Q}} = \frac{\text{digital correlator sensitivity}}{\text{analogue correlator sensitivity}}. \tag{2.132}$$

Finally, this allows to construct the sensitivity of the synthesized image to be:

$$\Delta B^{\mathrm{D}} = \frac{\sqrt{2} \cdot k_{\mathrm{B}} \cdot T_{\mathrm{sys}}}{A_{\mathrm{eff}} \cdot \eta_{\mathrm{Q}} \cdot \sqrt{\frac{n_{\mathrm{a}} \cdot (n_{\mathrm{a}}-1)}{2} \cdot \Delta\nu \cdot \tau_0}}. \tag{2.133}$$

Sampling With the sampling of measured data, only discrete $(u_{\mathrm{k}}, v_{\mathrm{k}})$ locations in the (u,v)-plane can be obtained, which can mathematically be described as a multiplication of the visibility function with a sampling function, as shown in equation (2.120). Hence, the dirty image $B^{\mathrm{D}}(\xi,\eta)$ is the ngiven by the convolution of their Fourier transforms:

$$B^{\mathrm{D}}(\xi,\eta) = \mathscr{F}\mathscr{T}\left[V(u,v) \cdot S(u,v)\right] = \mathscr{F}\mathscr{T}\left[V(u,v)\right] \star\star \mathscr{F}\mathscr{T}\left[S(u,v)\right], \tag{2.134}$$

where the double-star $\star\star$ indicates a two-dimensional convolution.

Weighting Analogous to the sampling, we can write the dirty image brightness distribution $B^{\mathrm{D}}(\xi,\eta)$ as convolutions of Fourier transforms, of the weighting $W(u,v)$, the visibility function $V(u,v)$ and the sampling function $S(u,v)$ as:

$$\begin{aligned} B^{\mathrm{D}}(\xi,\eta) &= \mathscr{F}\mathscr{T}\left[W(u,v) \cdot V(u,v) \cdot S(u,v)\right] \\ &= \mathscr{F}\mathscr{T}\left[W(u,v)\right] \star\star (\mathscr{F}\mathscr{T}\left[V(u,v)\right] \star\star \mathscr{F}\mathscr{T}\left[S(u,v)\right]) \end{aligned} \tag{2.135}$$

This weighting function W consists of three individual factors:

- R_{k} accounts for different telescope properties within an array (e.g. different A_{eff}, T_{sys}, $\Delta\nu$ and τ_{a}),
- T_{k} is a taper that controls the beam shape,
- D_{k} weights the density of the measured visibilities.

The D_k-factor affects the angular resolution and sensitivity of the array. On the one hand side, the highest angular resolution can be achieved by weighting the visibilities as if they had been measured uniformly over the entire (u,v)-plane. Therefore, this weighting scheme is called uniform weighting. Since the density of the measured visibilities is higher at the center of the (u,v)-plane, the visibilities in the outer part are over-weighted leading to the highest angular resolution. On the other hand, the highest sensitivity is achieved if all measured visibilities are weighted by identical weights. This weighting scheme is called natural weighting. The main properties of both schemes are summarized in the following:

natural weighting:

- $D_\mathrm{k} = 1$
- broader synthesized beam
- highest sensitivity

uniform weighting:

- $D_\mathrm{k} = \frac{1}{n(\mathrm{k})}$, in which $n(\mathrm{k})$ is the number of visibilities occurring within an area of constant size around the weighted visibility
- highest resolution
- lowest sensitivity

CLEAN Imaging Algorithm

The brightness distribution $B(\xi,\eta)$ of an observed radio source is given by the Fourier transform of the complex visibility $V(u,v)$ measured by a radio-interferometry array. However, since this visibility is only measured at discrete locations, there are gaps in the (u,v)-plane, which gives rise to diffraction structures in the image domain. Therefore, the image that is obtained by Fourier-transforming the observed visibility, and hence contains the diffraction structures, is referred to as a dirty image. This dirty image is the convolution of the true brightness distribution with the so-called dirty beam which is given by the Fourier transform of the sampling function $S(u,v)$ (see equation (2.120)). Therefore, the dirty image has to be deconvolved to obtain the true brightness distribution of the observed source.

However, usually this map is convolved with a beam with a HPBW eventually for displaying the restored brightness distribution $B(\xi,\eta)$ with

$$HPBW \approx \frac{\lambda}{D_{\max}}, \tag{2.136}$$

with λ as the observing wavelength and $D_{\max}$ as the length of the maximum baseline. This is also representing the angular resolution of the array. In the following, the CLEAN algorithm is presented, because all of the images shown in this work were created by this approach. While there is also other algorithms that are in use, like the maximum entrophy method (Cornwell & Evans 1985), adaptive scale pixel decomposition (Bhatnagar & Cornwell 2004) or the most recent Bayesian extended emission imaging (Junklewitz et al. 2015), the CLEAN algorithm showed to be more robust overall and better controllable.

The CLEAN algorithm introduced by Högbom (1974) is one of the most widely used and most successful deconvolution methods. It is a numerical deconvolving process applied in the image (ξ, η) domain, which corresponds to filling the gaps in the (u, v)-plane in the visibility domain. The CLEAN algorithm works according to the following method:

1. Compute the dirty image $B^{\mathrm{D}}(\xi, \eta)$ and the dirty beam $F^{\mathrm{D}}(\xi, \eta)$ by Fourier transform of the weighted visibility $V^{\mathrm{W}}(u, v) = S(u, v) \cdot W(u, v) \cdot V(u, v)$ and the weighted sampling function $S^{\mathrm{W}}(u, v) = W(u, v) \cdot S(u, v)$, respectively. Here, the grid spacing $\Delta\xi, \Delta\eta$ in the image domain should not exceed about $\frac{1}{3}$ of the dirty beam-width.

2. Find the point of highest brightness in the dirty image and subtract $\gamma \cdot F^{\mathrm{D}}(\xi, \eta) \cdot B^{\mathrm{D}}_{\max}(\xi, \eta)$, in which γ is the loop gain that commonly has a value of a few tenths, i.e. $0 < \gamma \leq 1$. Then, store the position and amplitude of the removed component by inserting a δ-function of height $\gamma \cdot B^{\mathrm{D}}_{\max}(\xi, \eta)$ into a CLEAN model.

3. Repeat step 2 iteratively until all significant source structure has been removed from the dirty image; this is a user-defined condition for which there are several possible indicators, e.g., one can compare the peak brightness to the rms noise, or look at which iteration the rms noise does not decrease when a component is subtracted, or note when a significant number of negative components appears.

4. Convolve the δ-functions of the CLEAN model with an idealized CLEAN beam corresponding to a Gaussian with $HPBW \approx \frac{\lambda}{D_{\max}}$.

5. Add the convolved components of the CLEAN model to the residual map to obtain the final CLEAN image.

Using this method, the CLEAN algorithm models the true brightness distribution as an ensemble of point sources. The obtained CLEAN image represents the least-mean-squares fit of the Fourier transforms of the δ-function components to the observed visibility, if the number of the δ-function components is smaller than the number of independent visibility data. Using the FFT, the numbers of grid points in the (u,v)-plane are equal to those of the (ξ,η) plane, however not all (u,v)-grid points contain visibility data. Therefore, it is a common procedure to define limited areas, or windows, in the dirty image and apply the CLEAN algorithm in those windows only.

Self Calibration

Because of inaccuracies during data taking, or the lack of, or incorrect accounting of influences on the signal during the traverse of different media (e.g. the ionosphere) there are also random residual phase and amplitude errors, that can be removed by a method called self-calibration (Cornwell & Wilkinson 1981; Cornwell & Fomalont 1999; Thompson et al. 2001). For this method, the observation of a target radio source is corrected using either the phases and amplitudes of a strong point source that is located within the observed field, or using a bright and simple component of an extended source, e.g. a CLEAN component. The time-dependent visibilities $V_{ij}^{obs}(t)$ observed by the i-th and j-th telescopes of an array is given by

$$V_{ij}^{obs}(t) = g_i(t) \cdot g_j^{\star}(t) \cdot g_{ij}(t) \cdot V_{ij}^{true}(t) + \epsilon_{ij}(t)\,, \tag{2.137}$$

where $g_i(t)$ and $g_j(t)$ are the complex gain factors of the two telescopes, $g_{ij}(t)$ is a non-separable gain factor of the correlated power, and $\epsilon_{ij}(t)$ is the noise term. Because of the given "high-tech" hardware, $g_{ij}(t)$ can be assumed to be constant, so that one only has to deal with the perturbations of $g_i(t)$ and $g_j(t)$. Then the observed visibilities, on which self-calibration has to be applied, can be written as

$$V_{ij}^{obs}(t) = g_i(t) \cdot g_j^{\star}(t) \cdot V_{ij}^{true}(t) + \epsilon_{ij}(t)\,. \tag{2.138}$$

Now, the aim of self-calibration is to adjust the complex gain factors $g_i(t)$ and $g_j(t)$ such as to minimize the mean-squared-difference S between the observed visibilities $V_{ij}^{obs}(t)$ and the visibilities $V_{ij}^{model}(t)$ that are predicted by a model, e.g. a initial CLEAN model. This mean-squared-difference S is then given by

$$S = \sum_k \sum_{i,j;i\neq j} w_{ij}(t_k) \cdot \left| V_{ij}^{obs}(t_k) - g_i(t_k) \cdot g_j^{\star}(t_k) \cdot V_{ij}^{model}(t_k) \right|^2 , \tag{2.139}$$

in which $w_{ij}(t_k)$ are weights that should be inversely proportional to the variance of $\epsilon_{ij}(t_k)$, and t_k is a user-defined time interval. This expression for S can also be written as

$$S = \sum_k \sum_{i,j;i\neq j} w_{ij}(t_k) \cdot \left| V_{ij}^{\text{model}}(t_k) \right| \cdot \left| X_{ij}(t_k) - g_i(t_k) \cdot g_j^{\star}(t_k) \right|^2 , \tag{2.140}$$

in which

$$X_{ij}(t_k) = \frac{V_{ij}^{\text{obs}}(t_k)}{V_{ij}^{\text{model}}(t_k)} . \tag{2.141}$$

This quantity $X_{ij}(t_k)$ is proportional to the complex gain factors, if the model is correct, and therefore represents the response of the interferometer to a phase calibrator. Therefore, $X_{ij}(t_k)$ can be used to calculate these complex gain factors. However, the model visibilities $V_{ij}^{\text{model}}(t_k)$ that are used to determine $X_{ij}(t_k)$ are only approximations, meaning that $X_{ij}(t_k)$ has to be computed via an iterative procedure. In combination with the CLEAN algorithm self-calibration then works as follows:

1. Produce an initial CLEAN model.
2. Compute $X_{ij}(t_k)$ for each t_k.
3. Compute the gain factors $g_i(t)$ and $g_j(t)$ for each t_k.
4. Calibrate the observed visibilities $V_{ij}^{\text{obs}}(t_k)$ using these gain factors and Fourier-transform them to obtain a new dirty image.
5. Produce a new CLEAN image that is then used for the next model.
6. Check for convergence and go back to step 2 if necessary.

2.4.5 Digital Beamforming

Digital beamforming plays a crucial role in the successful operation of not only in radio astronomy, but also in state-of-the-art radio data transmission technologies, like 3/4/5G. From optics, we know that any optical path can be inverted and it is still valid. Meaning, a system designed as a receiver works exactly the same way as an emitter when inverting the time axis (Jackson 1975). This should already give an indication that any achievement in radio astronomy (where the devices act as receivers) reflects positively onto radio data transmission technologies and vice versa.

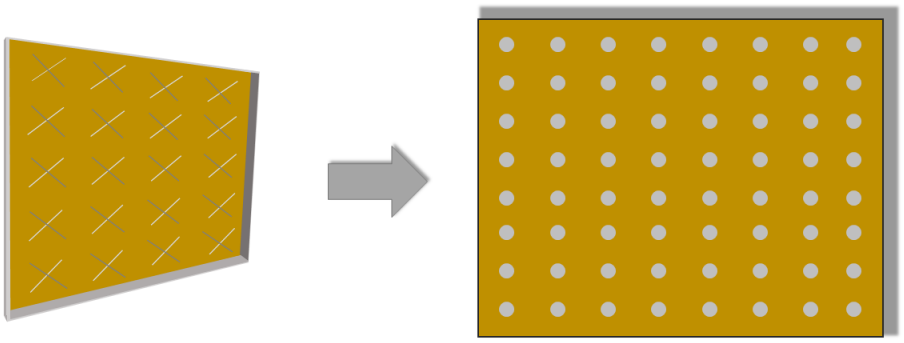

Figure 2.25: On the left is an array of cross-polarized dipoles. Crossed dipoles allow you to receive/transmit signals from/to any direction. For simplicity, we will represent these dipole arrays as a board, where each cross is represented by a dot (right).

3D Path Difference In order to build up an understanding and intuition for how beams are formed, adjusted, and steered, we will start with the basics. The easiest receiver system would be a dipole, but we know that a dipole is only able to detect the radio emission parallel to its orientation, and cannot measure the orthogonal contributions of the electric field. Therefore, we assume any antenna element to be two dipoles orthogonal to each other, aligned as a cross. This was made use of in radio data transmission to transfer two different data streams simultaneously, one for each polarization, which is called polarization multiplexing. We want to assume a two dimensional array of cross-polarized dipoles. These are used in mobile 5G technology, as well as in the LOFAR telescope. In the schemes we simplify the depiction of the cross dipoles as simple circles for clarity.

We define the grid-plane to be in the x-y-plane with regular separations d_x,d_y between the elements. The z-axis is therefore perpendicular to the array plane. We indicate the numeration of individual elements via (p,q) for a grid with the dimensions (M,N). So the grid element for $x=2, y=3$ would be $(2,3)$.

As we already covered in the previous chapters, path differences between individual elements will define if we can have constructive interference when adding the individual signals at the elements. This is the case for both two dimensional arrays and linear ones, but the math is a bit more difficult for 2D. We assume an emitter at a distant point P, far enough that we can assume the emitted radio waves to be

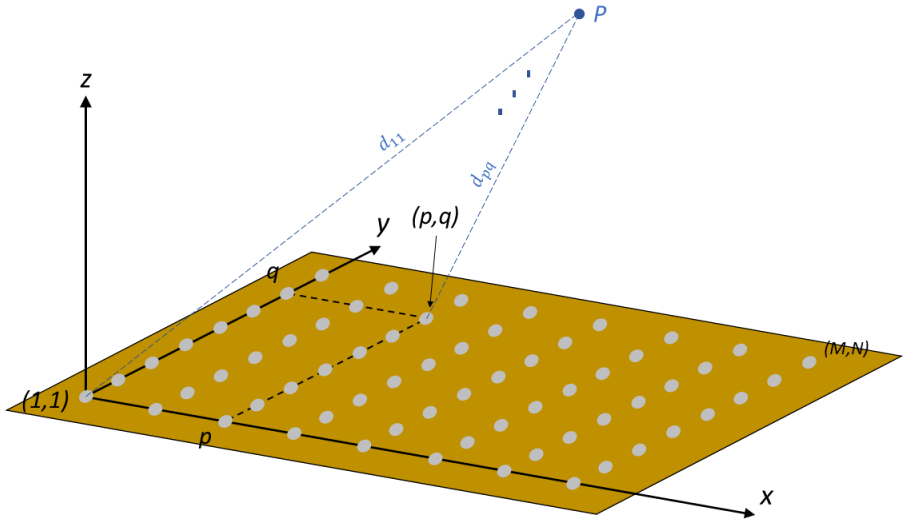

Figure 2.26: In a simple receiver array, the individual antennas are arranged in a grid. This Fig. shows an array of $M \times N$ elements in the x,y plane. A distant object P emits a wave that can be considered parallel when it reaches the antenna array. However, there is a time delay between the recordings of the same phase because d_{11} and d_{pq} are not identical.

considered parallel at our receiver system. We define the distances from each element to the emitter via $d_{p,q}$ and the time the signal takes to travel this distance $t_{p,q}$. This way we can calculate any time difference of the signal reaching the element (p,q) with respect to the signal reaching the element $(1,1)$ via $\tau = t_{1,1} - t_{p,q}$. Therefore the path difference would be $d = d_{1,1} - d_{p,q}$, with $t = \frac{d}{c}$, where c is the speed of light in the current medium.
The vector $\vec{r}$ is pointing from $(1,1)$ towards the point P with unit length. Thus it can be described by

$$\vec{r} = r_x \vec{u}_x + r_y \vec{u}_y + r_z \vec{u}_z \tag{2.142}$$

$$r_x = \sin\theta \cdot \cos\varphi \tag{2.143}$$

$$r_y = \sin\theta \cdot \sin\varphi \tag{2.144}$$

$$r_z = \cos\theta. \tag{2.145}$$

Here $\vec{u}_{x,y,z}$ are the unit vectors along the x, y, z axis. This description is also known as the polar coordinate system and is more helpful in our approach to describe the set up. A vector from $(1,1)$ to (p,q) is therefore:

$$\vec{r}_{p,q} = (p-1)d_x \vec{u}_x + (q-1)d_y \vec{u}_y. \tag{2.146}$$

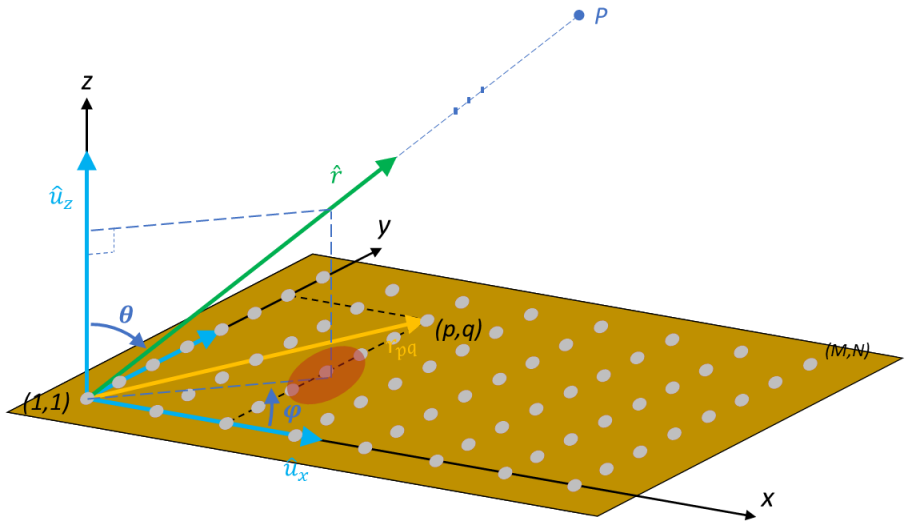

Figure 2.27: The observed source is in the direction $\vec{r}$. The baseline between the antenna at (1,1) and the one at (p,q) is r_{pq}. In spherical coordinates, the path difference between d_{11} and d_{pq} is given by $\Delta l_{p,q} = (p-1)\sin(\theta)\cos(\phi)\,d_x + (q-1)\sin(\theta)\sin(\phi)\,d_y$.

The path difference $\Delta l_{p,q}$ between $(1,1)$ and any element at (p,q) is therefore the scalar product:

$$\Delta l_{p,q} = \vec{r} \cdot \vec{r}_{p,q} \tag{2.147}$$

$$\Delta l_{p,q} = r_x(p-1)d_x + r_y(q-1)d_y. \tag{2.148}$$

Or in polar coordinates:

$$\Delta l_{p,q} = (p-1)\sin\theta\ \cos\varphi\ d_x + (q-1)\sin\theta\ \sin\varphi\ d_y. \tag{2.149}$$

Array Element Signal Any signal that is observed by the element $(1,1)$ can be described as:

$$s_{1,1}(t) = s_{11;0} \cdot \cos(\omega_0 \cdot t), \tag{2.150}$$

where $s_{11;0}$ is time independent in our case. This contains the amplitude defined by the radiating astrophysical source and is to be considered constant during the correlation time steps. In a more general approach, this value would be considered to be time dependent, like in the case of radio data transmission, where this would be the a modulation of the carrier signal and thus not time independent. In this situation the carrier frequency should be chosen to be much higher, so that the modulation frequency can

be considered as quasi constant again. Because any element (p,q) experiences a time delay with respect to the $(1,1)$ element, the signal at any element can be written as:

$$s_{p,q}(t) \cong s_{11;0} \cdot \cos(\omega_0 \cdot t + \omega_0 \cdot \tau_{p,q}). \tag{2.151}$$

Rewriting this into the Euler form:

$$s_{p,q}(t) \cong \Re[s_{11;0} \cdot e^{i\omega_0 \tau_{p,q}} e^{i\omega_0 t}]. \tag{2.152}$$

For ease of calculation, we take it for granted that $s_{p,q}(t)$ here is real, and drop the notation to express this explicitly. The expression $e^{i\omega_0 t}$ is multiplied at each element and thus not of any interest because it is to be treated like any multiplicative (time dependent) factor applied to every element uniformly. For consistency we thus assume the following: $m(t) = s_{11;0} \cdot e^{i\omega_0 t}$. This leads us to the following signal component for each element, also called complex envelope or phasor in the literature:

$$s_{p,q}(t) = m(t) \cdot e^{i\omega_0 \tau_{p,q}}. \tag{2.153}$$

Array Factor Since $\tau_{p,q} = \frac{\Delta l_{pq}}{c}$ and $\omega_0 = 2\pi \frac{c}{\lambda}$, we can write the phasor at any array element as:

$$s_{p,q}(t) = m(t) \cdot e^{i2\pi \frac{\Delta l_{p,q}}{\lambda}}. \tag{2.154}$$

In polar coordinates:

$$s_{p,q}(t) = m(t) \cdot e^{i\left[2\pi \frac{d_x}{\lambda}(p-1)\sin\theta\ \cos\varphi + 2\pi \frac{d_y}{\lambda}(q-1)\sin\theta\ \sin\varphi\right]} \tag{2.155}$$

After the correlator adds up all the elements' signals, the total phasor signal is:

$$s_{\text{tot}}(t) = m(t) \sum_{p=1}^{M} \sum_{q=1}^{N} e^{i\left[2\pi \frac{d_x}{\lambda}(p-1)\sin\theta\ \cos\varphi + 2\pi \frac{d_y}{\lambda}(q-1)\sin\theta\ \sin\varphi\right]} \tag{2.156}$$

In order to implement beamforming we need to introduce weights $w_{p,q}$ on each element (p,q). These are multiplicative complex factors to the signal, and can thus alter its amplitude and frequency. If such weights are used, the total phasor signal function has the form of:

$$s_{\text{tot}}(t) = m(t) \sum_{p=1}^{M} \sum_{q=1}^{N} w_{p,q} \cdot e^{i\left[2\pi \frac{d_x}{\lambda}(p-1)\sin\theta\ \cos\varphi + 2\pi \frac{d_y}{\lambda}(q-1)\sin\theta\ \sin\varphi\right]} \tag{2.157}$$

The doubled sum term is called the array factor. In real application, the array also has a device specific element factor $E_e(\theta,\varphi)$, which is multiplied with the phasor function. This factor needs to be determined in the laboratory with artificial sources in

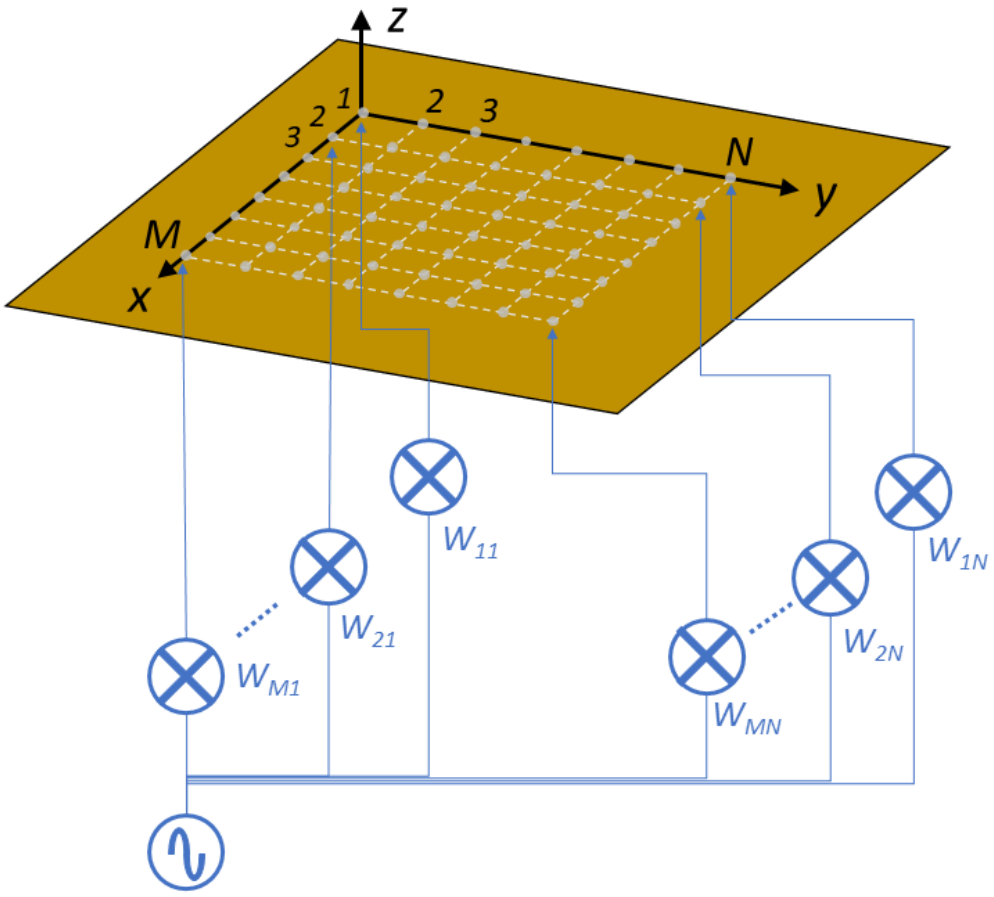

Figure 2.28: The beam of a telescope can be altered depending on how much each antenna contributes to the final signal. By applying weights $w_{p,q}$ you can easily influence and steer the telescope beam. They have a linear effect on the array factor $A(\theta,\phi)$.

various directions. For the LOFAR telescope these measurements were carried out by a drone flying over an array field with precisely measured positions above the array. For simplicity, we assume a perfect array with no direction dependency and therefore $E_e(\theta,\varphi) = 1$.

Beam Steering Our goal is to define the weights such that beam steering can be implemented. Approaching the process mathematically, we start with the array factor $A(\theta,\varphi)$, which we derived in the previous chapter from the phasor function, and define a substitution to simplify things:

$$A(\theta,\varphi) = \sum_{p=1}^{M}\sum_{q=1}^{N} w_{p,q}\cdot e^{i\left[2\pi\frac{d_x}{\lambda}(p-1)\cdot a + 2\pi\frac{d_y}{\lambda}(q-1)\cdot b\right]}, \tag{2.158}$$

with $a = \sin\theta\ \cos\varphi$ and $b = \sin\theta\ \sin\varphi$.

Here, the only variables depending on θ and φ are the substitutions a and b that we just defined. So with these new variables, a steering procedure would constitute a shift in these values described as:

$$A_s(\theta,\varphi) = \sum_{p=1}^{M}\sum_{q=1}^{N} w_{p,q}\cdot e^{i\left[2\pi\frac{d_x}{\lambda}(p-1)\cdot(a-a_s)+2\pi\frac{d_y}{\lambda}(q-1)\cdot(b-b_s)\right]}, \tag{2.159}$$

with $a_s = \sin\theta_s\ \cos\varphi_s$ and $b_s = \sin\theta_s\ \sin\varphi_s$ which point to the desired beam direction in polar coordinates (θ_s,φ_s). We already know that the weighting is multiplied within the array factor $s_{\text{tot}}(\theta,\varphi) = m(t)\sum_{p=1}^{M}\sum_{q=1}^{N} w_{p,q}\cdot e^{i\left[2\pi\frac{d_x}{\lambda}(p-1)\cdot a+2\pi\frac{d_y}{\lambda}(q-1)\cdot b\right]}$ in the total phasor function. This means that the weighting factor must be of the form:

$$w_{p,q} = e^{-i2\pi\frac{d_x}{\lambda}(p-1)\cdot a_s}\cdot e^{-i2\pi\frac{d_y}{\lambda}(q-1)\cdot b_s} \tag{2.160}$$

In this way, we can calculate all weightings necessary to point the beam of the array in the (θ,φ) direction.

By rewriting the total array factor with a shifted beam, we can see that the total array factor is actually a multiplication of the array factor in x and the array factor in y direction:

$$A_s(\theta,\varphi) = \sum_{p=1}^{M} e^{i2\pi(p-1)\frac{d_x}{\lambda}\cdot(a-a_s)}\cdot\sum_{q=1}^{N} e^{i2\pi(q-1)\frac{d_y}{\lambda}\cdot(b-b_s)} \tag{2.161}$$

$$A_s(\theta,\varphi) = A_{s,x}(\theta,\varphi)\cdot A_{s,y}(\theta,\varphi) \tag{2.162}$$

Here we actually see two geometric series. This is easier to see when we substitute $\Psi_x = 2\pi\frac{d_x}{\lambda}(a-a_s)$ which, for the array factor in x direction, leads to:

$$A_{s,x}(\theta,\varphi) = \sum_{p=1}^{M} e^{i(p-1)\Psi_x} \tag{2.163}$$

via geometric progression. We know this can be also written as:

$$A_{s,x}(\theta,\varphi) = \frac{1-e^{i\Psi_x M}}{1-e^{i\Psi_x}} = \frac{\sin\left(\frac{M\Psi_x}{2}\right)}{\sin\left(\frac{\Psi_x}{2}\right)} = \frac{\sin\left(\frac{M\cdot 2\pi x_\lambda(a-a_s)}{2}\right)}{\sin\left(\frac{2\pi x_\lambda(a-a_s)}{2}\right)}, \tag{2.164}$$

with $x_\lambda = \frac{d_x}{\lambda}$. In the same way for the y direction:

$$A_{s,y}(\theta,\varphi) = \frac{\sin\left(\frac{N\cdot 2\pi y_\lambda (b-b_s)}{2}\right)}{\sin\left(\frac{2\pi y_\lambda (b-b_s)}{2}\right)}, \tag{2.165}$$

with $y_\lambda = \frac{d_y}{\lambda}$. Note that we can easily create one dimensional arrays by setting either M or N to 1, which will also set the respective array factor to 1 and there won't be any contribution by the respective dimension. Calculating the array factor for a non-shifted 2×2 and 8×8 element grid, the calculations will result are plotted in Fig. 2.29. Note that a small shift of 1° is used because otherwise the simulation displays artefacts at the beginning and end of the mesh calculations along the sphere. However, the images shown are as representative to the eye as they would be without the shift.

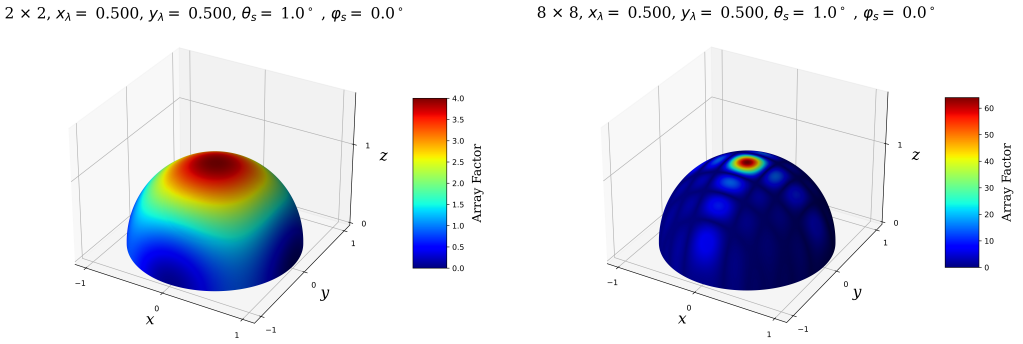

Figure 2.29: The coloring indicates the array factor distribution for a quadratic 4 and 64 element array. It is clear that the 64 element array produces a much more focused beam than the 4 element array.

Here we immediately see the more focused beam due to more elements (with constant distance between elements), thus a bigger array and a better resolution capability. We can also see nicely side lobes forming away from the primary beam. When steering is applied (Fig. 2.30), we can observe a deformation at low elevation angles, which is the primary reason, why such arrays should avoid observations at low elevations, because there the array's properties are significantly decreased in quality.

Using this procedure, we can also model the array factors of a commercial 5G antenna operating at $\nu = 3.5\,\text{GHz}$ (model: *Massive MIMO 64R64T*). This array has a regular grid architecture with 8×8 dipole antennas supporting both linear polarisation modes. The total array dimensions are 400 mm × 700 mm. Although the 5G array is a transmit and receive unit, the same characteristics apply as for receive only arrays. An example of a receive only array is the **LO**w-**F**requency **AR**ray; van Haarlem et al. 2013 (LOFAR) **H**igh **B**and **A**ntenna (HBA) international station (see Fig. 3.4). Here the dipole array is roughly 39×39. However, the HBA field is not a perfect rectangular grid, it is very close to one and gives a very good approximation. The observation frequency is about $\nu = 150\,\text{MHz}$, with array dimensions of about $56.5\,\text{m} \times 56.5\,\text{m}$. The resulting array factor

distribution for the 5G array and for the LOFAR international HBA field is shown in Fig. 2.31.

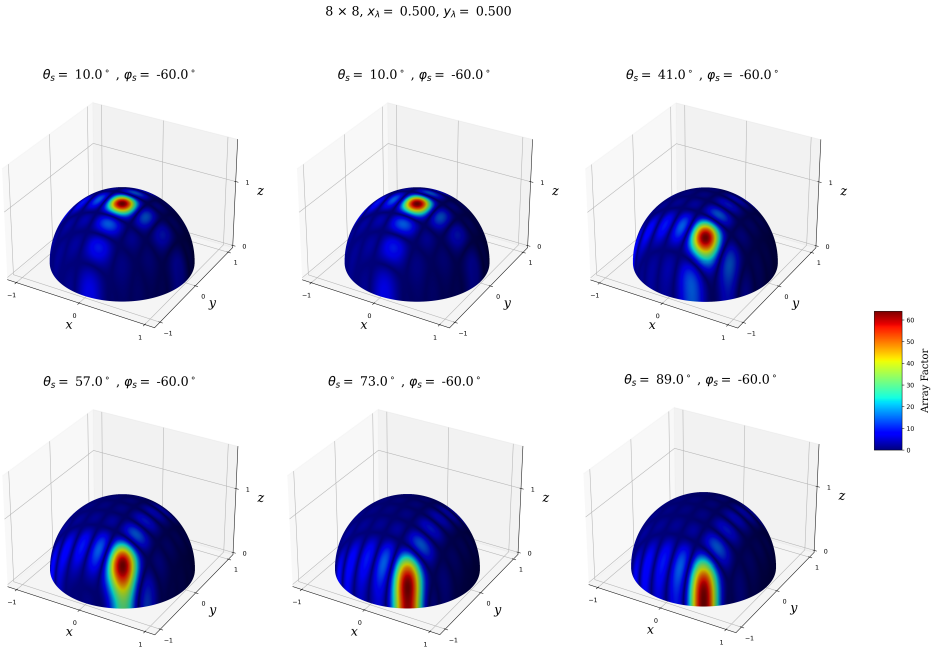

Figure 2.30: With steering applied, the array factor distribution shows a controllable beam (for a 64 element array in this case). It can also be seen that small declinations lead to beam deformation; this is a purely geometric consequence and cannot be mitigated.

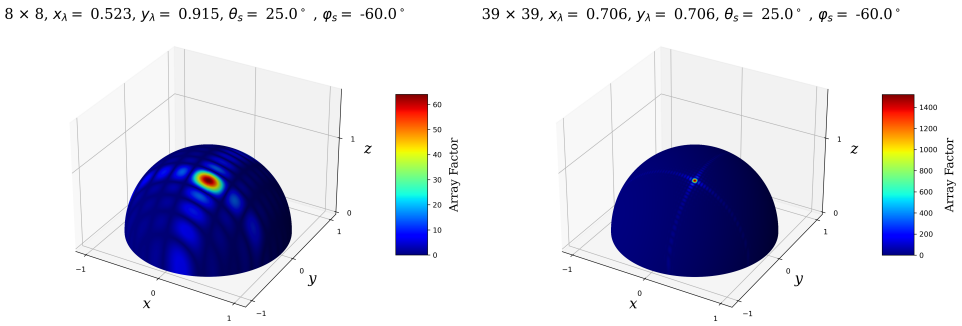

Figure 2.31: With steering applied, the left image shows the array factor distribution of a commercial 5G antenna at $\nu = 3.5\,\text{GHz}$. The right image shows the same steering applied, but for a LOFAR HBA international station operating at $\nu \approx 150\,\text{MHz}$.

3 The International LOFAR Telescope

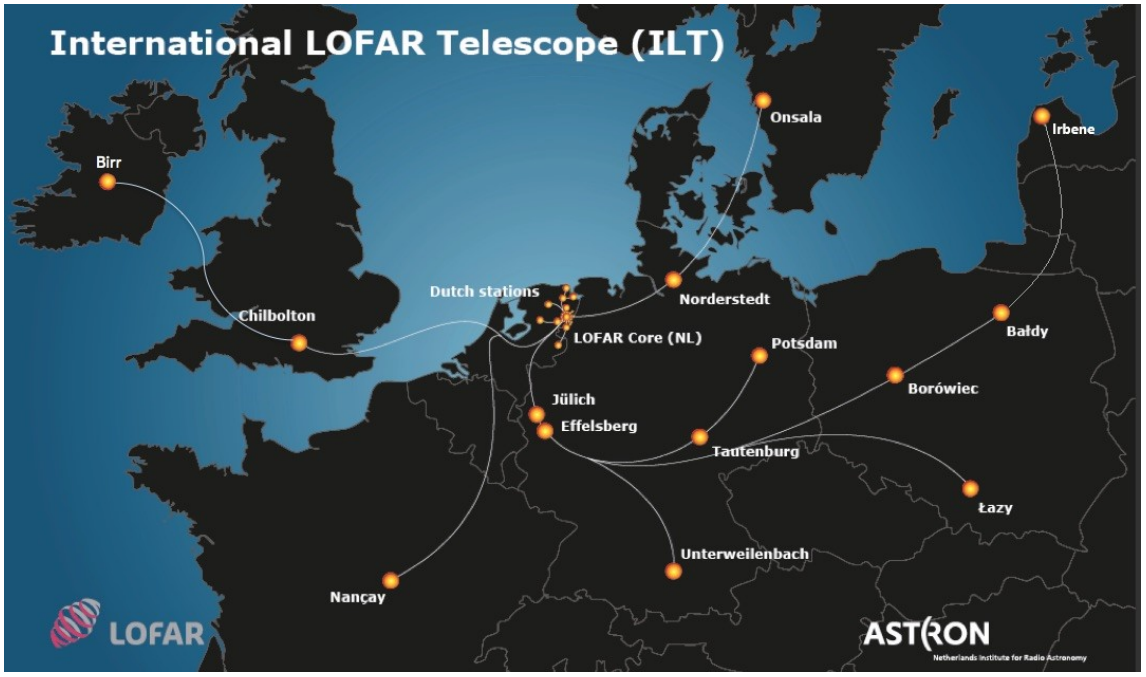

Figure 3.1: This map shows the locations of all ILT stations currently in operation (April 2022). Note that the data presented in this work were collected when the Polish, Irish and Latvian stations were not yet operational. Credit: ASTRON/LOFAR

The ILT is the the telescope, which was mainly used to acquire the results and perform the studies, described in this work. Because of that significant importance for the overall work, this chapter will introduce the instrument and the data processing pipeline used to achieve the findings, reported in this work.

The ILT is an interferometer of phased arrays, operational since 2012 in Europe. It has 38 stations located in the Netherlands and additional six stations in Germany, one station in France, one station in the United Kingdom, one station in Sweden, three stations in Poland, one station in Ireland and one station in Latvia. The stations outside of the Netherlands are referred to as *international stations* with a maximum

baseline of around 2,000 km (Ireland - Latvia). While the stations in the Netherlands are operated and maintained by **ASTR**onomisch **O**nderzoek in **N**ederland (ASTRON), international stations are maintained by the local station operators. Any data presented in this work made use of the full ILT array, excluding the polish, irish and latvian stations. At the time of observation these stations had not been added to the array, yet. Note, that sometimes papers and publications refer to the ILT by calling it LOFAR. To avoid confusion, it is recommended to refer to observations taken by the full array as ILT observations, and observations, only making use of the dutch stations, as LOFAR observations. The instrument has the greatest station density in the *Superterp* near Exloo (Fig. 3.2). It is made up of six stations (CS002, CS003, CS004, CS005, CS006, CS007), which are a subset of 24 *core stations*. The longest core-to-core baseline is ~ 4 km. *Core stations* are denoted with the prefix 'CS' in LOFAR metadata. The second subset of so-called Dutch stations are the *remote stations*, which carry the prefix 'RS' in the LOFAR metadata and have a longest remote-to-remote baseline length of ~ 120 km.

Figure 3.2: Aerial view of the Superterp, the densest array of stations in the ILT, located near Exloo in the Netherlands. The Superterp consists of six core stations with a maximum baseline of about 350 m. Credit: ASTRON/LOFAR

Each station consists of two phased arrays, each made up of a different type of antenna. The **L**ow **B**and **A**ntenna (LBA) operates between (10–90) MHz and the HBA covers (120–240) MHz, granting the ILT a total coverage of around (10–240) MHz. At the time of writing, only astronomers with significant expertise with LOFAR take observa-

tions using international LBA stations, mostly due to (software-)engineering hurdles which are expected to be solved eventually. For the average astronomer, the practically usable coverage of the ILT is (120–240) MHz.

The core and remote stations have 48 HBA's and 96 LBA's (Fig. 3.3). The antennas are connected to a total of 48 digital **ReC**eiver **U**nits (RCUs). The core stations' HBA fields are arranged in two 24-element arrays, each 30.8 m in diameter and a LBA field of 87 m in diameter. The two 24-element arrays can either be used as individual stations or combined into one station. The remote stations' HBA fields contain all 48 elements in a single arrangement of 41 m in diameter. The LBA fields between core and remote stations are similar in properties.

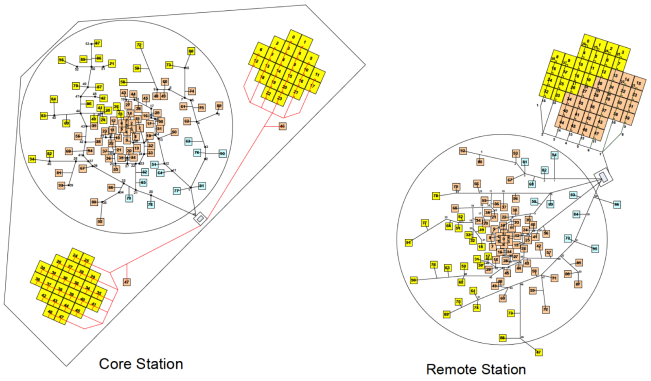

Figure 3.3: The core and remote stations have 48 HBA's and 96 LBA's. Core stations distribute the HBA elements over two fields, as opposed to the single field used in remote stations. Credit: ASTRON/LOFAR

The international stations have 96 HBAs and 96 LBAs (Fig. 3.4). The antennas are connected to a total of 96 digital RCUs. The HBA field is arranged in a diameter of 56.5 m. The LBA field is arranged in a diameter of 70 m. Because of local conditions, the HBA field of one german station (Effelsberg; DE601) has a slightly elongated arrangement compared to the standard international station layout. This station thus requires additional oversight in the form of the maintenance of dedicated calibration tables, a task performed by the radio observatory.

3.1 The Low Band Antenna

LBA antennas are sensitive to EM signals in the range of (10–90) MHz. As seen in Fig. 3.5, the element consists of a central **P**oly**V**inyl**C**hlorid (PVC) tube, that carries the signal cables to the top where a low noise amplifier is attached in a housing. Four

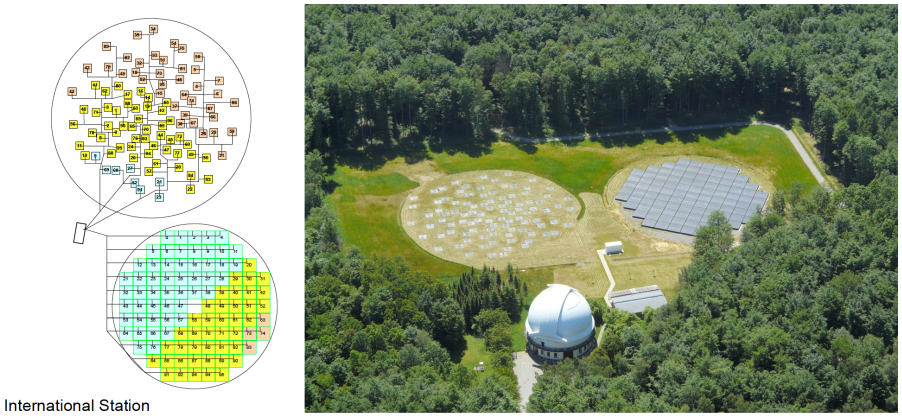

Figure 3.4: The international stations have 96 HBAs and 96 LBAs. On the left is the schematic arrangement of the antennas (Credit: ASTRON/LOFAR). On the right is a bird's eye view of the international station at the Thüringer Landessternwarte (Credit: M. Pluto/TLS).

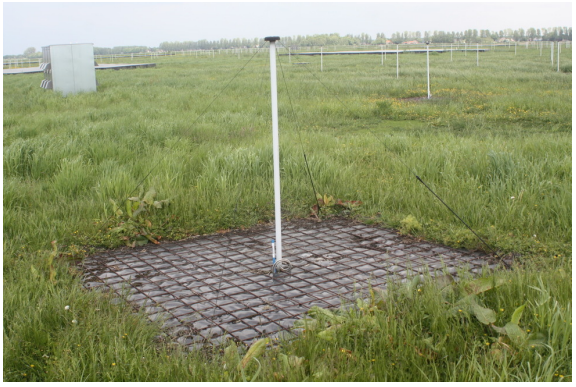

Figure 3.5: A single LBA element. The central PVC tube carries the cables to the top, where four dipoles are attached to the base edges at a 45° angle. There are 96 of these elements in a station. Credit: ASTRON/LOFAR

dipole cables connected to the base edges in a 45° angle can collect either X, Y polarized signals or a total flux with no polarization information. At the time of writing, the configuration of the Dutch stations prevents full polarisation observations (X and Y, simultaneously) with all antennas due to the number of receivers installed, while the international stations have enough receivers to allow full polarisation observations. To provide ILT polarisation measurements with the LBA, only half of the 96 LBA antennas can currently be used at the Dutch stations. With the currently undergoing LOFAR 2.0 upgrade, future observations will allow the collection of full array X and Y polarisation data. Observations with the LBAs offer the following modes for the user (compare Fig. 3.6):

- *LBAOUTER:* Selects the 48 outermost antennas in the field. This mode is preferred for observations below 40 MHz. Array width: 87 m.

- *LBAINNER:* Selects the 46 innermost antennas plus 2 outer ones as calibration antennas. This mode is preferred for observations above 40 MHz. Array width: 30 m.

- *LBASPARSE:* Selects the half of the innermost and half of the outermost antennas (48 in total). This mode is preferred for intra-station baselines or low resolution all-sky observations. Array width: 87 m.

- *LBAX:* All 96 antennas with X polarization (NE to SW).

- *LBAY:* All 96 antennas with Y polarization (NW to SE).

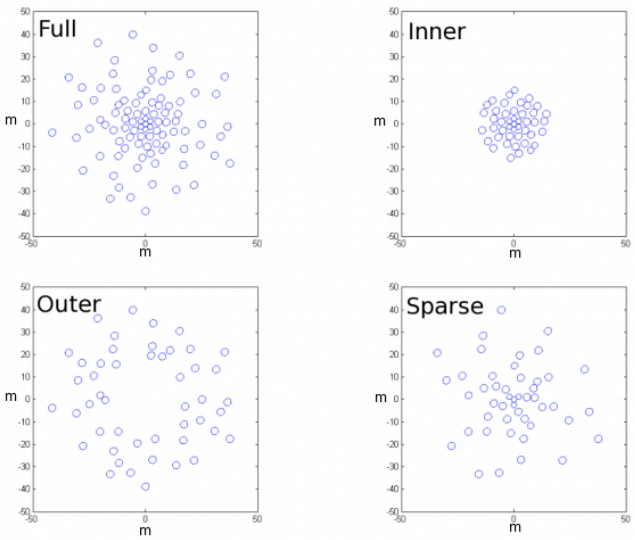

Figure 3.6: Available LBA configurations for observing modes. The blue circles indicate individual LBA antennas used for observations in each mode. Credit: ASTRON/LOFAR

It is very difficult to extract science-quality data from LBA observations made, using only Dutch LOFAR stations. The main reason for that is a lack of sky models comparable to the sensitivity and resolution, that LOFAR can achieve. Sky models of insufficient quality can thus dominate the error budget in final science images made with data from the instrument. Using the full ILT with all stations intensifies these issues further. Other issues are as well the exclusion of leakage from other bright sources in the vicinity, for example CygA or PerA, as well as ground based interference due to radio transmissions, devices and machines. Removing these parasite signals is non-trivial and thus creates additional challenges in the data processing. Future improvements in data processing and improved sky models will enable reliable LBA observations.

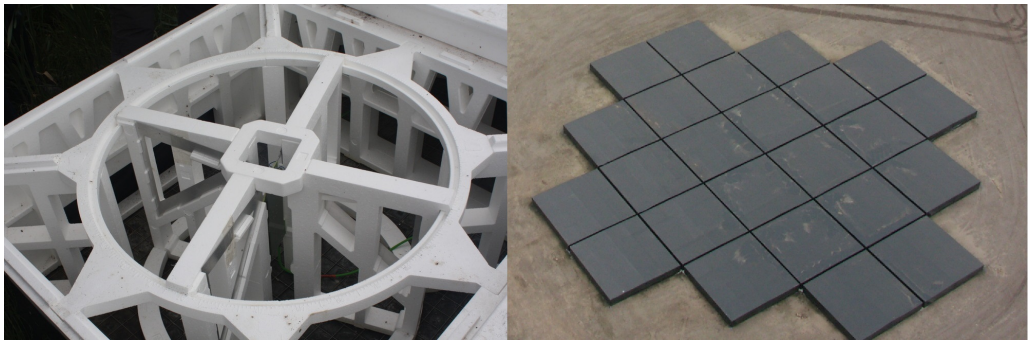

Figure 3.7: Left: An uncovered HBA element. 16 polystyrene boxes in each element, each containing four aluminum triangular dipoles angled at 45°. **right:** A HBA element (tile) consists of 4 × 4 polystyrene boxes covered by a black polypropylene sheet. With the 24 tiles in the image this arrangement provides 384 dipoles in X- and Y-polarization, each. Credit: ASTRON/LOFAR

3.2 The High Band Antenna

Observations with the HBA offer a frequency coverage of (120–240) MHz. One HBA element is made of 16 Styrofoam-cube housings (Fig. 3.7) that hold each four aluminum triangles operating as dipoles, hold in place at a 45° angle to the ground. These 16 cases are placed in a 4 × 4 configuration as one element (tile), covered in a black polypropylene sheet, as a protection from environmental influences. Core and remote stations have 48 HBA elements which are arranged in a single field in remote stations, and split into two 24 element fields in core stations. International stations have 96 elements arranged in a single field. Note that the Effelsberg station (DE601) has a slightly elongated arrangement of the tile field due to geographic constraints. Observations with the HBA offer the following modes for the user:

- *HBAzero/HBAone:* Uses only one of the core station tile fields (field zero or field one).
- *HBAdual:* Each tile field is treated as an individual station in the correlator. This provides many more short baselines.
- *HBAjoined:* Each core stations' tile fields are firstly correlated together before transmitted to further processing. This results in a non-uniform shape of the beam.
- *HBA[zero/one/dual/joined]_inner:* Only the inner 24 tiles in the remote stations are used to match the design of the core stations. Other than that, properties of the respective mode apply.

All presented data in this work was observed with the HBA in the *HBAdual* mode.

3.3 Low Frequency Challenges with LOFAR

Low-frequency radio-interferometric observations (metric wavelengths) have their own specific challenge. These are not only present for the ILT, but also other similar telescopes, like the **M**urchison **W**idefield **A**rray; Wayth et al. 2015 (MWA) or the **S**quare **K**ilometre **A**rray (SKA). Some limitations are inherent to the telescope design and cannot be overcome, like the observation frequency and the consequential resolution capabilities or their sensitivity. They define the basic properties of any radio telescope (array) and therefore its performance.

The Resolution in radians of any radio telescope array can be calculated via

$$\theta = 1.22 \cdot \frac{\lambda}{b_{\max}}, \tag{3.1}$$

where λ is the observation wavelength and $b_{\max}$ is the longest baseline between any elements of the array. Here we see that the resolution of a given array layout is inversely proportional to the observation wavelength. This makes low frequency (or long wavelength) radio arrays significantly poorer in resolution compared to higher frequency interferometers. To achieve equivalent resolution to a higher-frequency array, a low-frequency array must therefore have more distant stations - which introduces its own set of challenges.

The Field of view of a radio interferometer array can be calculated via the smallest primary beam of the elements in the array using

$$\theta = 1.22 \cdot \frac{\lambda}{D_{\max}}, \tag{3.2}$$

where $D_{\max}$ is the diameter of the largest array element. As mentioned above, low observation frequencies lead to larger primary beam diameters, increasing the size of the instrument's field of view. While a bigger field of view (up to 1°) can be desirable when performing surveys or using calibrator sources near the target of interest, a field of view that is too large can cause substantial issues in data calibration. Very strong emitters nearby can be picked up by the sidelobes of the array and elevate the overall signal to such an extent that data calibration can become impossible.

Sensitivity is related to the following telescope properties

$$\sigma_S \propto \frac{\nu}{A_{\text{eff}} \cdot \sqrt{\Delta\nu}}, \tag{3.3}$$

where ν is the observation frequency, A_{eff} the effective collection area and $\Delta\nu$ the bandwidth. Finally, the decreased resolution inherent to lower freuqencies can lead to "confusion noise" dominating the sensitivity budget. Where radio interferometers in the cm regime can resolve sources that appear close together, an interferometer operating at meter wavelengths may be unable to distinguish between individual sources due to lower resolution capability, despite having a higher sensitivity.

The ionosphere interacts with electromagnetic radiation via its free electrons. This leads to absorption, Faraday rotation, and refraction at around $10-300\,\text{MHz}$. Above an altitude of about 90 km, the Earth's atmosphere is ionized by UV and X-ray radiation emitted by the Sun. The density of free electrons controls the refractive index, which in turn determines the propagation of electromagnetic waves. The density of free electrons in the ionosphere is subject to periodic variations, such as the day-night cycle, the seasons, and the cycle of solar activity. Additionally, the ionosphere is not uniform over large areas. Elements of larger arrays therefore collect electromagnetic signals passing through different regions of the ionosphere which leads to coherence loss at great enough distances, if left uncorrected (Fig. 3.8).

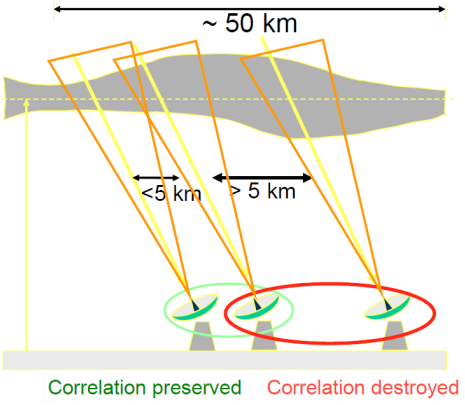

Figure 3.8: Stations that are closer together can have overlapping lines of sight, observing "through" the same patch of ionosphere. This helps to preserve the correlation between these stations. If they are far enough apart that there is no overlap, the correlation between these stations is destroyed.

To deal with this issue, two main approaches are used at the time of writing. One can calculate ionospheric screens which are computed via time-variable Zernike Polynomial phases. For these screens, individual pointings of bright, point-like sources that can be modeled, within in one field, are needed. Extrapolations for any area in-between these pointings can be calculated and used to calibrate any target. This technique is less useful when the array reaches a certain resolution; the screen models need more bright points than there are suitable calibrators in the field (under-sampling).

Another way to deal with the ionospheric distortions is to make use of the **T**otal **E**lectron **C**ontent (TEC) in the ionosphere. For this, **G**lobal **P**ositioning **S**ystem (GPS)

data can be used as a first estimation at the location of the stations. Then, the Faraday rotation, absorption and refraction effects can be calibrated with this value, since they all mainly depend on the electron content of the ionosphere as "seen" by the individual station.

Time/Bandwidth smearing is likely to be experienced when observations have a high fractional bandwidth, meaning the lowest observable frequency and the highest observable frequency by the telescope have significant differences in resolution and the field of view. This is more likely the case for observations at low frequencies. Correlating across the whole dataset and averaging over the whole frequency band will introduce strong bandwidth smearing effects. This becomes apparent in washed-out brightness distributions and even more so in significant decreases of correlated signal moving away from the phase center. Smirnov (2011) has a detailed explanation of the specific calculations. To handle this issue, it is necessary to split the bandwidth into many spectral channels, perform the calibration and imaging procedure on the individual channels, and then re-combine the final data as needed. This may make calibration and imaging more difficult because each spectral channel will have less signal and additionally the computation demands may increase significantly. In such cases it can help to find a strong, well-known source nearby (ideally a bright, non-variable point source), calibrate the dataset on this source with smaller spectral channels, and transfer the solutions to the target.

Radio Frequency Interference (RFI) is usually introduced by human-made emitters, e.g., for tele-communication. These tend to be narrow-band emitters at known frequencies. Shorter baselines are more susceptible to these effects because this signal needs to be present at both stations to not be washed out by the correlator. Longer baselines don't suffer as much from **R**adio **F**requency **I**nterference (RFI). The signatures in the visibilities can usually also be detected rather easily due to their distinct signature and because most of them are already known. Occasionally, RFI remains undetected in the early stages of calibration, but creates issues in the later stages. This can be noticed by inspecting the outputs of every stage of calibration. Usually, software products that are used for calibration, offer inspection plots automatically to go through, or the possibilities to create these.

Non-coplanar arrays are arrays with individual stations positioned in space such that they do not span a single plane. While this is the case for any telescope array with more than three stations, only small variations to a common plane are usually negliga-

ble. The bigger arrays grow in size, the more significant these variations become, until they cannot be neglected anymore, at which point they are referred to as non-coplanar arrays. Especially big interferometers with baselines of several thousand km do not hold to this assumption and are therefore considered. Small fields of view can return us to the domain of validity of the underlying approximation, but observations at low frequencies have large fields of view, compared to higher frequency observations. In order to achieve coherence in our correlation without increasing the complexity of the Fourier Transforms to a computationally unfeasible extent, two approaches can be used.

w-projection is a way to deal with non-coplanar arrays. Firstly one has to find a plane which minimizes the distance of each element to the w-direction. In the next step, all stations which are not in this plane already are projected to the imaginary position in the plane with $w = 0$. This means that corrections with an additional positive or negative time delay, along with diffraction effects, need to be accounted for.Projecting all stations to their respective $(u, v, w = 0)$ coordinates allows us to reduce the convolution problem to two dimensions again (Cornwell et al. 2008).

Faceting is another approach to handle non-coplanar arrays, which involves reducing larger fields of view offered by the interferometer into many smaller facets such that the following equation is satisfied:

$$2\pi \cdot w\left(\sqrt{1-l^2-m^2}-1\right) < 1. \tag{3.4}$$

The resulting field of view of an individual facet allows the Fourier Transforms to neglect the w-terms again. Having divided the field of view, calibration and imaging is performed on the individual facets and then they are re-combined (e.g., Intema et al. 2016). Modern faceting algorithms, like `DDFACET` (Tasse et al. 2018) also apply w-projection within each facet.

3.4 Big Data Challenges

Modern radio interferometer arrays, like the ILT or the SKA, make use of the most recent advancements in signal processing, which resulted in immense improvements for accuracy and sensitivity. However, this comes at the price of drastically increased data volumes that need to be processed and stored. Other fields of astronomy and physics in general also experienced a drastic increase in demand for computational needs (e.g. the **L**arge **H**adron **C**ollider (LHC)). Radio interferometry arrays are amongst the most

data driven, experimental setups; clearly, these instruments need to be treated in the context of Big Data. While this topic is usually discussed in the context of big tech companies like Google, Amazon or Facebook/Meta, decently sized radio observatories require just as much computation as these tech companies do, and sometimes even more.

3.4.1 Data Acquisition

Radio interferometers usually carry out several processes even before the data is stored for further scientific inspection. Individual elements in the array collect a signal with their receivers and transfer it to the correlator, where the signal between all elements is correlated as has been explained in previous chapters. This is the first data stream created by the telescope that needs to be addressed. Because correlation needs to be performed as precisely as possible, no time- or frequency- averaging occurs at this point meaning that this is the most data heavy step in the whole signal processing procedure, and is called the raw data-rate. For instance, the full ILT array collects a total raw data-rate of around 13 Tbit/s and after compression and processing archive data in the order of tenths of Peta Bytes per year (Begeman et al. 2011)! The upcoming Square Kilometer Array low (SKA-low) will exceed that significantly, with planned raw data-rates of about 8 Pbit/s! This means a total data throughput of around 30 ZetaBytes per year, which is in the same magnitude as the current (2020) total yearly throughput of wired and wireless Internet! Dealing with such enormous data rates, it is obvious that the new generation of radio interferometers have to solve a multitude of computational challenges. Boosting the correlation process times often makes use of Field-Programmable Gate Arrays (FPGAs). These devices are less versatile than CPUs but perform faster computation operations, when kept simple.

3.4.2 Data Storage

Unavoidably, the huge data streams create vast amounts of information to be stored. In the process of data handling, there are multiple steps where intermediate data storage is necessary to cache the data for further processing. Here the bandwidth must be very high, but because the data is moved after processing, the total stored volume is not nearly as high as in the final step, where the data is archived for further scientific analysis. The archived data products can have enormous technical demands, not only due to size, but also to make this data accessible to scientists all over the world for further processing.

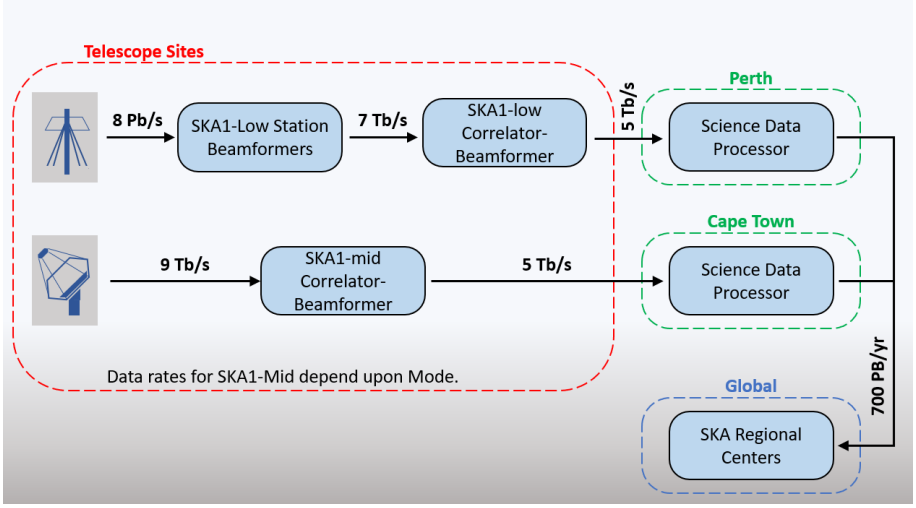

Figure 3.9: Astrophysical observations produce a lot of data. Here the data streams of the SKA are shown as an example. While the ILT has data streams about one order of magnitude smaller, the SKA is the best guide for future interferometry programs.

In the data processing stage, the data is being reduced in size with every step. With every calibration and removal of low-quality data, the observation data shrinks in size drastically. Despite this, even after correlation and compression, SKA has a planned storage demand of around 700 PB per year. The planned minimum operation time for SKA is 50 years which means the archive volume will be well within the exa-scale regime for long term storage.

3.4.3 Data Processing

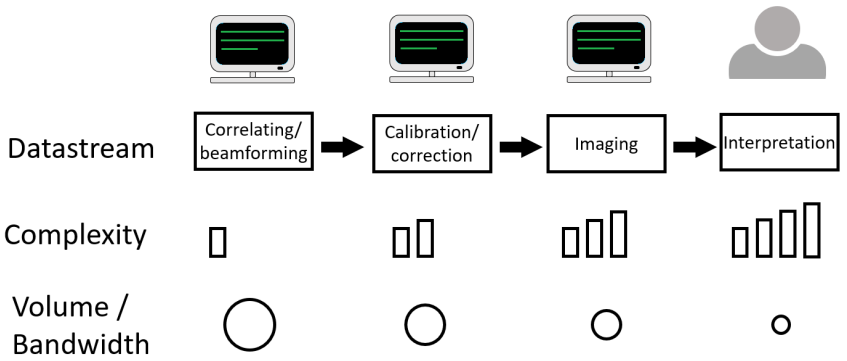

Figure 3.10: An observation produces a large amount of data. Therefore, the reduction of this data is usually done by an algorithm. The scientist does only those steps of the analysis that cannot be done properly by a computer, usually far down in the data stream once its volume has been reduced. The most complex part of the analysis, the interpretation, can only be done by a human.

Working with these amounts of data requires highly automated data processing pipelines. Of course the interactive treatment of the data by a trained operator would lead to the best quality of the data processing but this would be far too time intensive and would thus not be feasible for these amounts of data. Automated processes can reduce the output quality, for example, by removing too many frequency bands during RFI removal. It is important to balance the pros and cons of automating steps with the pros and cons of human involvement. The usual approach here is to perform the easiest steps at the beginning of the data stream and increase the complexity downstream. With increasing complexity, the data volumes decrease, and human involvement should be later in the pipeline where the most complex steps need to be done with the least amount of data. In the best case scenario the pipeline automatically processes data and produces the final images for the scientists to interpret. There are efforts to push that boundary even further and allow machine learned code to classify objects in the images, but it is still necessary for scientists to evaluate the end result to double-check and maintain reliability.

3.5 LOFAR-VLBI Data Calibration and Processing

After many years of operation, calibration processes for the dutch LOFAR stations has become reliable enough to be routine. Now standardized calibration can be provided to achieve maps with $6''$ resolution in a 20 square degree **F**ield **O**f **V**iew (FOV) with the HBA (at around 150 MHz). Calibration and imaging strategies that also implement **D**irection **D**ependent **E**ffects (DDEs) at such low frequencies (van Weeren et al. 2016; Tasse et al. 2018, 2021) allowed for more than 300 published publications presenting LOFAR results. Still only a little fraction of those make use of the full ILT, that currently provides an angular resolution of $0.27''$ at 150 Mhz. Including international stations, also improves sensitivity capabilities, due to the larger HBA fields, that are twice in area compared to the core or remote stations. The larger effective collection area is also beneficial to minimize the FOV of the array, effectively reducing unwanted wide-field effects due to strong emitters in the vicinity to the target of interest. With more upcoming international stations in the future, we can expect yet further improvements in the data quality. Despite the tremendous scientific perspectives of the ILT in contrast to only using dutch stations, most scientific results don't make use of the full potential that the ILT offers. A list of publications demonstrates that the calibration and handling of the amounts of data that the ILT provides are possible (e.g, Moldón et al. 2015; Varenius et al. 2015; Jackson et al. 2016; Varenius et al. 2016; Ramírez-Olivencia et al. 2018; Harris et al. 2019; Kappes et al. 2019), even using the LBA at 54 MHz (Morabito

et al. 2016). The reasons for the low numbers of publications are manifold. The most prominent is due to the fact that the ionosphere plays a crucial role when dealing with observations at low frequencies. Signals originating from astrophysical objects get corrupted when traversing it before detection (Intema et al. 2009). Although this issue can affect measurements made using only the Dutch stations, it is much more significant when the international stations are used.
While LOFAR is technically a connected interferometer via fibre feeds to the correlator, remote and international stations use independet local clocks. These clocks introduce further issues that cause clock offsets and to a lesser extent, clock drifts, which need to be accounted for, for each observation for every time step per station.
Another issue is the present lack of precise models of suitable calibrators. When observed at comparable sensitivity and the presence of accurate models to a scale of the resulting resolution, corruption effects due to instrumental and sky (propagation) effects can be corrected (Smirnov 2011). This sets the absolute flux calibration and removes mentioned direction-independent instrumental effects. The impacts of incomplete sky models was shown in Grobler et al. (2014), where ghost sources were able to be introduced, meeting significance criteria.
From this point on, another calibration is necessary to correct the introduced dispersive delay by the ionosphere:

$$d = \frac{\Delta\Phi}{\Delta\nu}, \tag{3.5}$$

with Φ as the phase and ν as the frequency. At the moment, only an experimental release of **C**ommon **A**stronomy **S**oftware **A**pplication; McMullin et al. 2007; Jaeger 2008 (CASA) and the LOFAR-VLBI pipeline[1] (Morabito et al. 2021) are publicly available to perform such corrections. With the now complete **L**ong **B**aseline **C**alibrator **S**urvey; Jackson et al. 2016, 2022 (LBCS) there exists a set of known, suitable calibrator sources which can be used to solve for the dispersive delays in the northern hemisphere at 150 MHz. With the recent developments these improvements allow the processing of such demanding data even to non-LOFAR experts. In the following we discuss the necessary steps, then using the LOFAR-VLBI pipeline in more detail.

3.5.1 Calibration Strategy for LOFAR-VLBI

The calibration and processing of ILT data involves a multitude of necessary steps and the correct handling of various software. A graphical overview in a block diagram is given in Fig. 3.11. The whole procedure is built to deal with data which has already

[1] https://github.com/lmorabit/lofar-vlbi

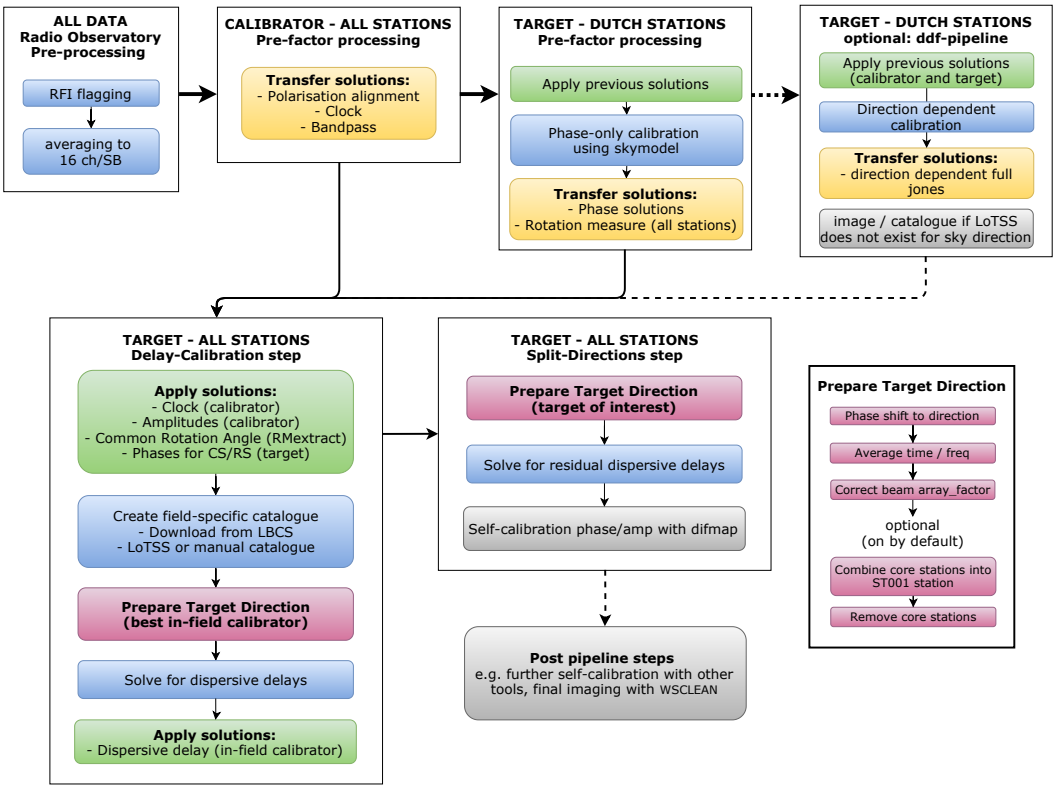

Figure 3.11: The LOFAR-VLBI strategy presented by Morabito et al. (2021). Boxes represent self-contained steps with different sub-steps. The boxes contain information about the data being processed, the stations being considered and the name of the step. Colors indicate the types of calculation (blue), solution transfer (yellow), solution application (green), preparation steps (red) and other (gray). Optional steps are indicated by dashed lines. Credits: Morabito et al. (2021).

been pre-processed by the radio observatory: namely, this means it has passed a first RFI flagging via the use of the AOFLAGGER (Offringa 2010) and following frequency averaging of 16 channels per sub-band. Identifying RFI contamination is most effective at higher frequency resolution. This procedure is the general case for most ILT observations before made accessible through the LOFAR **L**ong **T**erm **A**rchive (LTA), but because this can vary, adjustments to fit other radio observatory pre-processed data can be defined by the end user. Such a standard observation with 8 hours observation time has about 4 TB of data size, 16 TB if no compression is applied (DYSCO, Offringa 2016).

Starting with such data, the whole procedure is basically divided into two major parts. Firstly, the data is processed in a standard fashion, as applied to the **Lo**far **T**wo-metre **S**ky **S**urvey; Shimwell et al. 2017 (LoTSS). The derived solutions in the various steps are transferred to the second part, the LOFAR-VLBI pipeline, which provides a calibrated

dataset alongside various inspection plots. The following sections will present a more in-depth presentation of the individual tasks performed.

3.5.2 LOFAR-VLBI Pre-Processing

In this section, we describe in detail the pre-processing steps which the data undergoes prior to the LOFAR-VLBI pipeline.

Flux Calibrator Processing

The PREFACTOR[2] pipeline is used to solve for, and apply, the gains and set the flux density scaling. The applied calibration is described in de Gasperin et al. (2018). Here the dataset of the flux calibrator observation is at first pre-flagged where poor data is detected and afterwards averaged in time and if necessary in frequency. Complex gain solutions are obtained for XX and YY for polarisation alignment, which is to correct differences between XX and YY, rotation measure which is introduced in the data due to Faraday rotation, bandpass calibration, clock corrections for differences (offsets and drifts) in clock times for individual stations and lastly TEC values for dispersive delays due to the ionosphere. The named effects are being determined and corrected, one after the other, in the listed order. After correction of one effect the corrected dataset is used as input for the correction of the next correction. These corrections are applied to all stations, while it is important to highlight that the gain calibration of the international stations is of utter importance at the earliest stage possible. Because of their significant bigger effective collection area, they are more sensitive than core or remote stations, and provide thus significantly higher gains in the observation data. Any issues in the early stages can affect subsequent calibration steps significantly with the possibility of data degradation to an extent, where no image can be achieved with the full ILT array. Because of that, it is important to check inspection plots in this steps and logs, for possible issues that could lead to e.g. catastrophic flagging. Also, the quality of the available calibrator source model is of significant importance, since this also can lead to poor calibration results if the the model is insufficient.
The obtained solutions which are direction-independent, namely polarisation alignment, clock and bandpass, are exported in a single file in Hierarchical data format version 5 (Anderson et al. 2011; Group 2000-2010), called a *h5parm*.

[2] https://github.com/lofar-astron/prefactor

Direction-Independent Processing of the Dutch Stations

After solving and applying the solutions from the previous flux calibration, further PREFACTOR calibration steps follow, which are important for the later stages, especially when forming a so called 'super' station, usually denoted ST001 in the metadata. This is described in more detail in the Sect. 3.5.3. All sub-steps in this calibration step operate on Dutch stations only (core and remote stations), unless noted otherwise.

Bright off-axis sources that are close enough to influence the target field, are removed from the data via `demixing`. Here the observation data is phase rotated to the position of the bright off-axis source, averaged in time and frequency, and calibrated with a model. With the acquired solutions, the source is removed from the dataset (Van Der Tol et al. 2007).

Following, data from the GPS database are downloaded for the time of observation. The archived information is available for 15 minute steps and is averaged in time and pointing, to match observation time and pointing towards the target of interest in order to calculate the rotation measure for each station (including international stations). This step is making use of the `RMextract` package (Mevius 2018). Due to the extrapolation applied, the inaccuracies are only correcting for bulk changes in the TEC. Solving for differential TEC is applied at a later stage. The obtained corrections are applied for polarisation alignment, bandpass, clock, beam, and rotation measure, in the given order. Usually, the data is also averaged in time and frequency afterwards (by a factor of four). Bright off-axis sources that were not demixed previously but are considered to be harmful, are estimated and clipped from the data.

Finally, with a skymodel created with the **T**IFR **G**MRT **S**ky **S**urvey (TGSS)-ADR1 (Intema et al. 2017), a phase-only calibration is performed on the target of interest. All collected solutions to this point are collected in a *h5parm*.

Direction-Dependent Processing of the Dutch Stations (optional)

Correcting for DDEs is not always necessary. This step allows to further improve the solutions for Dutch stations, collected from previous steps. Additionally, the result comes with a wide field image that can be used for inspection and as a sky model which is necessary in the later steps of the LOFAR-VLBI pipeline. If there already is coverage in the LoTSS, the latter two points mentioned are redundant. The remaining point of improving the solutions acquired so far, might also be not important if no subsequent issues could be noticed in the whole calibration and imaging procedure.

A practical and more detailed overview of this step is given by Shimwell et al. (2019). Generally, time, frequency, antenna, and direction dependent effects are collected in

Jones matrices (Hamaker & Bregman 1996). With `killMS` (Tasse 2014; Smirnov & Tasse 2015) the Jones matrices are calculated and applied during imaging with `DDFACET` (Tasse et al. 2018). In the imaging process, usually also three rounds of self-calibration are performed, alongside to bootstrapping the flux density scale and correcting the astrometry.
Note that if one aim is to create a combined wide-field images, it is necessary to derive those Jones matrices, as explained.

3.5.3 LOFAR-VLBI Pipeline

With the information stored in the *h5parm*, the pipeline as explained in Morabito et al. (2021) is able to process the observation data of the target field of interest. The pipeline is able to return calibrated datasets for one or multiple objects in the field. The first step is to apply the previously obtained solutions, for clock, amplitudes, the common rotation angle and phase corrections for core and remote stations. Two more steps are then taken to improve the calibration yet further. The first run makes use of a bright well known, or point-like calibrator in the vicinity of the target of interest. The derived phase solutions from there are further improved by another phase and amplitude self-calibration for the target of interest.

Create Field Specific Catalog

To pick the best phase calibrator around the target of interest, a catalog of the surrounding area is needed. The information of the LBCS and LoTSS are downloaded for an area with a default radius of 2°, because the long baselines limit the field of view due to time and bandwidth smearing, governed by averaging steps for time and frequency. Usual values for averaging are one second in time and around 10 kHz in frequency. While it showed that most potential calibrators further away than 1° usually lead to poor results, sometimes bright sources, even further away, e.g. 3C sources, are able to perform well as phase calibrators. Both catalogs need to be crossmatched because LBCS does not provide flux density information on these targets. If no catalog provides coverage for the field of interest, a user defined sky model can be used for this step, but must be defined manually in the process. The pipeline picks from the resulting catalog a best delay calibrator following an algorithm described in Morabito et al. (2021). At the time of writing this algorithm has yet to show, the best possible performance and may very well be changed in the future. In the case, that the automatic pipeline did not chose the best possible delay calibrator and the user knows a better pick, a manually defined phase calibrator can be selected by the user. The catalog also helps to

clip data from potential bright sources (≥ 5 Jy) in the field, that might interfere with the calibration process.

Prepare Target Direction

The data needs to be prepared before the phase calibration with the phase calibrator can begin. Firstly, the dataset is shifted to a position such that the calibrator is in the phase center. With the prepared catalog, now any possibly interfering bright sources are clipped from the data. This step is turned off by default by the pipeline, because of the considerate amount of time it takes to be performed. Afterwards, the data is averaged to bands of $\Delta\nu = 1.95$ MHz by default. The option to combine a set of stations into a *super* station is turned on by default and uses all available core stations to form ST001. Other subsets of stations can be defined by the user if needed, but it is recommended to keep the default settings for most of the observations. After creating ST001, all stations that formed it, are being removed from the dataset. Removing the core stations, adds the benefit to drastically decrease the FOV, reducing consequently luminous sources further away, helping to stabilize any self-calibration. Also, the data size gets reduced by around 80% (when observed in *HBAdual* Mode - see Sect. 3.2), which speeds up subsequent steps significantly.
It has to be mentioned, that introducing the super station leads to radially varying decoherence (Bonnassieux et al. 2020) on any baseline that contains ST001. While this effect is always present in these cases, it is negligible in the inner tens of arc-seconds distance to the phase center.

Solve for Dispersive Delay

Alterations of the signals phase information are introduced by frequency and time dependent effects. A first order approximation of the phase error due to these effects is:

$$\Delta\phi_{\nu,t} = \phi_0 + \frac{d\phi}{d\nu}\Delta\nu + \frac{d\phi}{dt}\Delta t, \tag{3.6}$$

where ϕ_0 is the phase offset, $\Delta\nu$ is the frequency bin, Δt is the time bin and ϕ is the phase. The second and third term on the right hand side are called delay and rate term. With a high **S**ignal to **N**oise **R**atio (SNR) the value for $\Delta\phi_{\nu,t}$ can be determined directly, given a small bandwidth and little time averaging. While this works for smaller arrays and higher frequencies, long baselines and low frequencies introduce faster variations in the phases. The interaction with the ionosphere also becomes significant at lower frequencies ($\lesssim 300$ MHz), introducing dispersive delays with the first-order dependence of $\tau_{\text{ion}} = d\phi/d\nu \propto \nu^{-2}$. It is further to mention, that most astrophysical

sources show spatial structure that can be resolved out with increasing baselines due to a decreasing FOV, eventually further decreasing the SNR.
The **delay term** is influenced by offsets in the clocks at different stations, which also drift in time, hence are not constant in time, but in frequency, as well as the aforementioned delays introduced by the ionosphere. The clock offsets and drifts are direction independent instrumental effects, while the ionospheric effects are direction dependent.
The **rate term** is mainly influenced by the coherence time of the signal, that is related to the wavelength. While it should be large in theory (~ 2 Minutes), rapid ionospheric changes can lead to significantly shorter coherence times, as short as 10 seconds.
The clock solutions for clock offsets and drifts are collected from the bright flux calibrator via the **Lo**far **So**ftware **To**ol; de Gasperin et al. 2019 (LoSoTo). The algorithm separates the dispersive from the non-dispersive effects via simultaneously fitting both, effectively extracting clock delays. These solutions are transferred to the phase calibrator and target. Because the algorithm assumes a single median clock offset per antenna, clock drifts are neglected at this point, but mostly of little relevance, because they were observed to be typically $\lesssim 10$ ns. With a bandwidth of $\Delta\nu = 48$ MHz, decorrelation is expected to happen after ~ 20 ns.
To recover the correct phase information, the right description of the dispersive delays is the key challenge. These delays are measured in TEC units and can be acquired by the TEC solving routine implemented in the **D**efault **P**ost **P**rocessing **P**ipeline; van Diepen et al. 2018 (DPPP). In the `gaincal` step the pipeline uses the caltype 'tecphase' and assumes a point source model. By that, the algorithm fits the phases for:

$$\phi = \phi_0 - \frac{c r_e}{4\pi} \frac{\mathrm{TEC}}{\nu}, \tag{3.7}$$

where c is the speed of light and r_e is the electron radius. TEC is given in units of 10^{16} electrons m^{-2}. The default parameters, which over the development time showed best overall results, feature solution intervals of $\Delta t = 16$ s, frequency channels grouped to $\Delta\nu = 195$ kHz and a minimum (u, v)-limit of 50 kλ, which corresponds to ~ 100 km. The latter parameter helps to suppress sources outside of the target field, which otherwise often significantly increase the overall noise.
With the TEC information amongst every station, their difference is given as **d**ifferential **T**otal **E**lectron **C**ontent (dTEC) and a single phase offset. In general, the dTEC describes the phase behaviour as a function of frequency. In order to solve for dTEC, a fitting procedure is applied to the phases along the frequency axis. The procedure works best when applied to the full bandwidth and needs at least a minimum of 10 MHz. When

inspecting the dTEC values for the stations, remote stations should have values close to 0 TEC units, while international stations may have values between ~ 0.1 to 4 TEC units. The remote stations are expected to show only small deviations, because they already were corrected in the `PREFACTOR` routine.
The calculated dTEC solutions are applied by the pipeline to the un-phase-shifted dataset where the `PREFACTOR` solutions are applied already. The corrected data is written to the `CORRECTED_DATA` column, to be picked up for self-calibration and imaging of the science target.

Target Phase and Amplitude Calibration

The following steps are performed in the `Split-Directions` step of the pipeline. Here any previously defined **D**irection **O**f **I**nterest (DOI), stored in the catalog file is processed in parallel. For each entry, a phase-shift is applied, averaging is applied to reduce the FOV, corrections are applied for the primary beam array factor, eventually applying self-calibration.
In detail, a measurement set is created for each defined DOI entry. With the default parameters, the dataset is averaged to 97.64 kHz in frequency and 8 s in time. Subsequently, the beam correction for the array factor is performed, after which the core stations are combined to ST001, then flagged and removed from the dataset. Before combining all bands to one measurement set, the aforementioned steps are performed on bands containing of 10 subbands.
At this point a bulk correction of the dispersive delay is already applied from the `Delay-Calibration` step. Because the DOI is located in another direction, residual effects will present, which is why each DOI is also corrected for the residual dispersive delay. The pipeline assumes the DOI to be a point source when solving for the dTEC and phase offset.
The subsequent self-calibration is performed by `DIFMAP` (Shepherd 1997). A python wrapper converts the measurement set to an *uvfits* file format via `ms2uvfits` with `writesyscal=F`, so the data is readable by `DIFMAP`. In this process, any channels, that were completely flagged previously get identified, to be excluded from loading (Stokes I only) in `DIFMAP`, since they crash the program. The python wrapper further prepares a selfcal script for `DIFMAP` with all gathered information and starts the hybrid mapping procedure that performs the self-calibration. While `DIFMAP` performs better than other approaches, using DPPP and `wsclean` (Offringa et al. 2014; Offringa & Smirnov 2017) it is very hard to alter `DIFMAP` due to its rigid nature. For example, there is no export of corrections data, only corrected data. Also, it self-calibrates amplitudes and phases, but not delays which play a crucial role for LOFAR observations, as seen before. The

pipeline incorporates a modified version of `DIFMAP`, that exports the acquired solutions within the self-calibration process with the `CORPLT` command to a `hdf4` file.

3.5.4 Post-Pipeline Steps

The previously described standard routine provides a result with inspection plots at various stages in the process, solution tables for various effects for the delay calibrator and the DOI, or multiples. While many examples (Morabito et al. 2022; Jackson et al. 2022; Sweijen et al. 2022; Ramírez-Olivencia et al. 2022; Timmerman et al. 2022; Kukreti et al. 2022; Badole et al. 2022; Harwood et al. 2022; Groeneveld et al. 2022; Bonnassieux et al. 2022; Kappes et al. 2022) produce reasonable results, it must be said, that one can improve the results, especially when dealing with weak and/or morphological complex sources, or having bad luck with a field that has no known good LBCS calibrator nearby. To improve the results, manual interaction in different ways may improve the quality. Situational, these improvements can be achieved by:

- Consult the inspection plots at any step available for bad antennas, frequency bands or observation times and flag them additionally.
- Manually selecting a different phase calibrator.
- Providing a source model for the delay calibrator. If no source model is available, imaging the phase calibrator first and using the image as source model is possible.
- Pickup the results from the DOI delay calibration and manually perform further self-calibration.
- If no suitable LBCS source is within reach, identify the brightest nearby source and use this as the delay calibrator, construct an image that one can feed back as model for the delay calibration.
- Additional tweaking of the parameters can improve results, but is hard to generalize, because various factors have to be put into account. Consulting expertise[3] from the long baseline working group is highly recommended, at this point.

3.5.5 Future Work

The pipeline is under permanent development with features not yet implemented. Complex and major changes, that are planned for the future will be discussed in

[3] https://lofar-vlbi.readthedocs.io/en/latest/help.html

Sect. 5. In this section, we want to highlight smaller changes, that are going to improve the pipelines performance and versatility, but will not introduce major new functionalities.

Currently, the calibration strategy performed on LBCS targets are based on dedicated LOFAR tools. Ongoing developments in CASA promise more refined calibration capabilities, in current versions also accounting for dispersive delays. This will allow for successful calibration of fainter sources with more complex morphologies.

Calibrators or targets of interest generally are processed very well, having a distance of $\lesssim 0.5$ deg and overall well at a distance of $\lesssim 0.5$ deg, depending on ionospheric conditions. In any case, this improvement improves the delay calibration especially for observations that suffer from a very active ionosphere or where the targets are far away from the phase center. This will allow to process DOIs that are currently not possible to be calibrated by the pipeline due to decorrelation introduced by poor delay corrections.

Corrections on dTEC are computed simultaneously for all directions. It can be beneficial to tell apart contributions of dispersive and non-dispersive origin to specifically address clock drifts. This is currently not implemented. But, the applied strategies at the moment are performing well in most cases that have been tested to have a contribution of < 10 ns, which does not lead to decorrelation.

The above is of course only a short summary of the upgrades and improvements being developed and implemented, but others largely fall under the incremental or quality-of-life rubric, and are therefore not covered in this work as they are not of significant scientific interest.

4 Resulting First Studies by the ILT

After introducing the necessary topics in the previous chapters, this chapter deals with two studies of distant blazars. The first part discusses the observation, data reduction and interpretation for the source S5 0836+710. The second part does the same for the source GB 1508+5714. The results of both studies have been published in Kappes et al. (2019) and Kappes et al. (2022) respectively. The focus of the data in both cases is on dedicated LOFAR observations, using the HBA antennas of the full ILT array, the highest resolution that LOFAR can achieve. It should be noted that although both studies make the same corrections to the data calibration, they are carried out using different tools in each case. The reason for this is that the standard calibration pipeline for long-baseline observations with LOFAR, as described in Sect. 3.5, was not available until 2021. The detailed calibration process performed on S5 0836+710 is described in Kappes (2017), while GB 1508+5714 was calibrated with the long-baseline calibration pipeline described in Sect. 3.5 of this work.

4.1 Studies of S5 0836+710

To test the first approaches developed for a long baseline pipeline for the ILT, the powerful high redshift ($z = 2.218$) blazar S5 0836+710 was chosen as a promising testbed for the pipeline's capabilities, expecting challenging conditions while providing an information window to an as yet unfulfilled target, allowing multiple scientific questions to be addressed.

In Sect. 1 it was mentioned that radio-loud AGN can form powerful synchrotron-emitting double-sided jets that extend into the **I**ntra**C**luster **M**edium (ICM). These jets can reach distances of megaparsecs, as reported by (Blandford et al. 2019).

4.1.1 Scientific Interest

Based on the Fanaroff-Riley classification (Fanaroff & Riley 1974), the most intense sources among these AGN have an FR-II morphology. In these cases the jets terminate in hotspots with a high surface brightness where they interact with the surrounding environment. FR-II radio galaxies have been extensively studied at centimeter wavelengths using the VLA (e.g. O'Dea et al. 2009). Such studies enable attempts to estimate a number of properties of these sources, such as their age, velocity, magnetic field, total lifetime, ambient gas density, and more. According to the AGN unification scheme (Antonucci 1993; Urry & Padovani 1995), FSRQs are the beamed counterparts of FR-II radio galaxies. Because of relativistic bulk motion of plasma at small inclination angles, the compact (i.e., parsec-scale) emission of blazar jets becomes drastically Doppler boosted and can be observed out to very high redshifts.

There are several additional challenges that must be considered when analyzing large-scale blazar data. Due to the significant projection effects at small inclination angles, the emission from the two lobes associated with the jet and the counterjet can appear to be blended. Additionally, the hotspots of the jet and counterjet are affected by noticeable differential Doppler boosting due to the moderately relativistic speeds of the hotspots in the **I**nter **G**alactic **M**edium (IGM) (O'Dea et al. 2009). As discussed in Sect. 1.2.1, differences in the light travel time between the two jets can also affect the observed arm ratios and lead to differential aging of the hotspot and counter-hotspot.

These challenges can be partially addressed by high-resolution observations at long wavelengths, such as those provided by the ILT. The ILT offers exceptional sensitivity between 40-240 MHz and significantly improved angular resolution compared to previous instruments. Studying the low-energy electron population ($\gamma < 1000$) responsible for blazar lobe emission can provide new insights into the large-scale structures of blazars and reveal some of the oldest observable structures in these powerful sources.

In particular, the counterjets of blazars are typically debeamed and thus undetectable, but the lobe and hotspot emission associated with these counterjets is expected to be less strongly debeamed. Due to their steep radio spectrum and small projected scales, they may be detectable in LOFAR observations even though they have remained undetected in previous high-frequency and/or low-resolution observations.

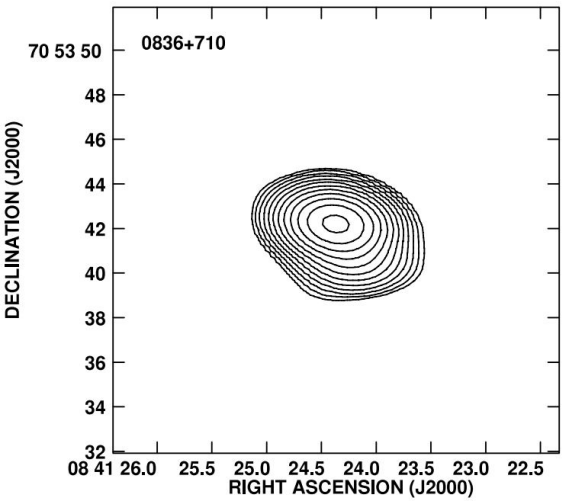

Figure 4.1: Total intensity of S5 0836+710 as observed by the VLA in A configuration at 1.4 GHz, published in Cooper et al. (2007). The image shows contours in successive powers of 2, starting at 12.65 mJy beam^{-1}. The beam size is 2.24'×1.46' with a position angle of 80.9°.

4.1.2 Previous Studies

The blazar S5 0836+710 at a high redshift (z = 2.218) was observed by Cooper et al. (2007) using the VLA at a frequency of 1.4 GHz (see Fig. 4.1). At this moderately low frequency, the VLA in its A configuration was unsuccessful in detecting the large-scale source structure. Higher frequency VLA observations by (e.g. O'Dea et al. 1988) and observations with the **M**ulti-**E**lement **R**adio **L**inked **I**nterferometer **N**etwork; Thomasson 1986 (MERLIN) at 1.6 GHz by (Hummel et al. 1992) revealed a single elongated and polarized emission object located about 1.5 arcseconds south of the jet core. This emission lacked a clear bridge connecting it to the core or a counterpart on the opposite side of the core. With an **E**uropean **V**LBI **N**etwork (EVN)+MERLIN observation (Perucho et al. 2012b), those features were observed at even better resolution (see Fig. 4.2).

In two studies, Perucho et al. (2012a) and Perucho et al. (2012b) proposed that the blazar S5 0836+710 was experiencing a **K**elvin-**H**elmholtz (KH) instability in its jet. This instability was thought to be the cause of the perturbation in the jet observed as extended visibility in previous studies by O'Dea et al. (1988) and Hummel et al. (1992). However, the authors also noted that the location of the perturbation would require intense dissipation of kinetic energy, which was not observed, and that the one-dimensional morphology of the kiloparsec-scale structure was not explained.

This work presents observations from LOFAR that address these issues. The results suggest that the extended-arc structure can be interpreted as a classical two-

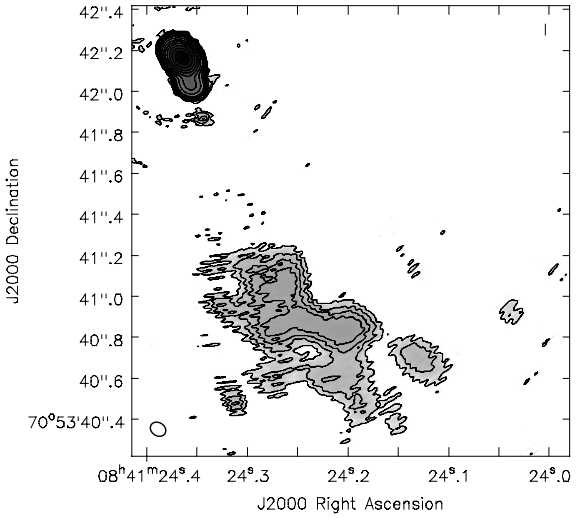

Figure 4.2: The total intensity of S5 0836+710, published in Perucho et al. (2012b), observed with EVN+MERLIN at 1.6 GHz. The contours represent intensity levels from 0.12 to 99% of the image peak intensity of 2.48 Jy/beam. The beam size is 84 mas×68 mas with a position angle of 57°.

dimensional source morphology, with the southern feature being a hotspot associated with an approaching jet, rather than a remnant of a broken jet.

4.1.3 Observation and Data Reduction

The observation of S5 0836+710 took place on June 17, 2015, performed by the ILT. The HBA array covered the full frequency range between 117.5 MHz to 162.6 MHz, over 4 hours. The primary flux calibrator was chosen to be 3C 196, which was observed for 10 minutes at the beginning of the observation. The recording was in 8-bit mode in 231 subbands, each with a bandwidth of 192 kHz. In the later stages of data processing, the subbands were averaged into 14 frequency bands, each with a 3.12 MHz bandwidth. The correlation was performed with the **CO**rrelator and **B**eamforming **A**pplication platform for the **L**ofar **T**elescope; ASTRON 2017 (COBALT) correlator (Broekema et al. 2018). A detailed description of the calibration process is described in Kappes (2017). For the sake of clarity, this section summarizes the important steps made to acquire the final dataset. Considering the previous studies of this source, only the long baselines contribute information about the morphology. Forming a superstation with all core and remote stations, creates a station, that over weighs drastically the international stations. Any inaccuracies in the superstation lead to potentially severe issues in later calibration steps. Because the pipeline was not yet mature at the time of processing, a superstation with only the six most inner core stations (called "the Superterp") was created. The other core and remote stations were flagged. The Superterp and the in-

ternational stations[1] were used to further calibrate the data, using **A**stronomical **I**mage **P**rocessing **S**ystem; Greisen 2003 (AIPS), following the standard methods of VLBI (e.g., Moran & Dhawan 1995). The time resolution was averaged to 16 seconds, effectively limiting the FOV to only the target source and suppressing any sources outside of the area of interest. In the final calibration steps, self-calibration techniques using DIFMAP (Shepherd 1997) were used, resulting in the shown (u, v)-coverage in Fig. 4.3 and the measured visibilities as a function of the (u, v)-radius that is shown in Fig. 4.4. Because of poor data and partially strong RFI, three bands had to be discarded, leading to 11 fully calibrated and imaged frequency bands (Kappes 2017), each with a 3.12 MHz bandwidth.

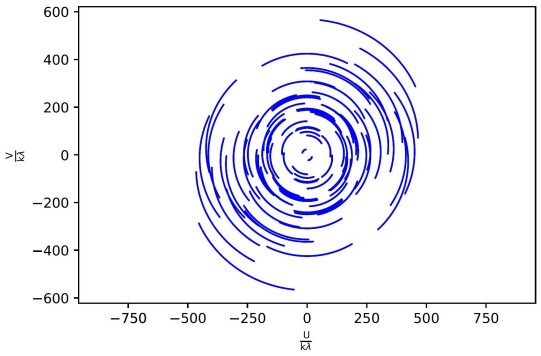

Figure 4.3: The (u, v)-coverage of the ILT data set at 135 MHz generated from the observation of the blazar S5 0836+710.

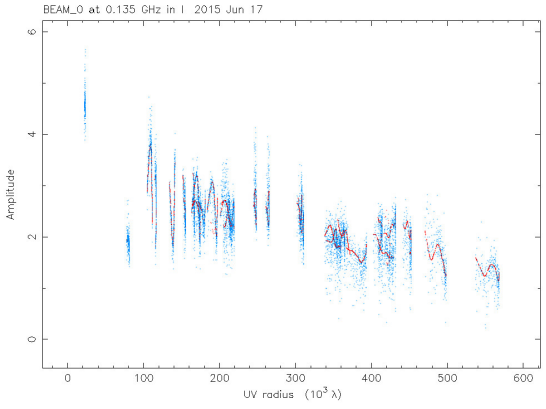

Figure 4.4: Measured visibilities in the 135 MHz ILT data set as a function of (u, v)-radius. The blue dots represent the visibilities, while the red dots show the model developed in the hybrid imaging process.

[1] In June 2015, this included six stations in Germany (DE601-DE605, and DE609), and one station each in Sweden (SE607), France (FR606), and the United Kingdom (UK608).

4.1.4 Results

By stacking the images of the 11 bands generated, an image with the central frequency of 143 MHz and a bandwidth of 34 MHz could be generated, displayed in Fig. 4.5. Comparing the results of previous observations at higher frequencies of S5 0836+710, with similar scales and angular resolution, a general morphological agreement can be found (see especially Fig. 5 and Fig. 1 in Hummel et al. 1992; Perucho et al. 2012b, respectively). Between 1 and 2 arcsec to the southwest of the unresolved compact core, the ILT data shows a resolved emission region. Observations with higher resolution and a smaller FOV (Perucho et al. 2012a) reveal a compact VLBI jet in southward-direction with an extent of about 200 mas (1.5 kpc) and shows signs of growing Kelvin-Helmholtz instabilities. Perucho et al. (2012b) interprets those to be the reason for a full disruption of the jet before it is able to reach arcsecond scales. In such a case, any remaining emission further away in the jet direction, like the observed resolved emission region by the ILT, can be interpreted as a subrelativistic relic of the disrupted jet. This relic is propagating further downstream and interacting with the IGM. In this process, such features usually show steep spectral indices[2] with values of $-2 < \alpha < -1$ (Pandey-Pommier et al. 2016). Using the 11 images for individual frequency bands obtained by the ILT, it is possible to reconstruct all images with the biggest beam (the beam of the lowest frequency band) and fit a powerlaw to each individual pixel position. The fitted powerlaw provides the spectral index for the respective pixel, eventually constructing the whole map as a spectral-index image, shown in Fig. 4.6. In the intra-ILT spectral-index image, the core appears flat to slightly inverted, while the spectral index of the southern component is moderately steep with a value of $\gtrsim -1$,. A resolved steep spectrum halo with a spectral index of about -1 surrounding the nucleus is another distinctive feature of the spectral index image. The halo was unseen in previous higher frequency images of S5 0836+710 and was only revealed by the combination of the ILT's good sensitivity and high angular resolution in the sub-GHz regime.

Intra-ILT spectral maps are particularly difficult to obtain reliably. Firstly, splitting the data into multiple frequency bands reduces the sensitivity in each band. On the other hand, splitting the data into as many bands as possible helps to suppress frequency dependent problems because they only show up in individual bands, but maintaining a significant enough signal to noise ratio limits the number of bands. Even when finding the optimal consensus, the fitting algorithm is left with an increased uncertainty in the flux values. Secondly, because the overall bandwidth is rather narrow, the uncertain-

[2] The notation $S_\nu \propto \nu^\alpha$ is applied, in which a negative spectral index α corresponds to a flux density S_ν that decreases with frequency.

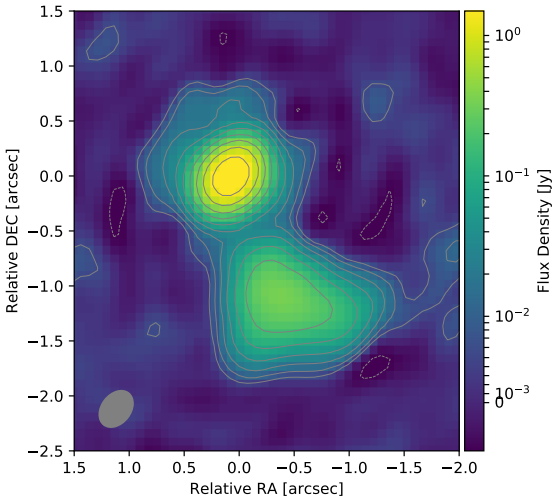

Figure 4.5: LOFAR stacked image (Kappes et al. 2019) of 11 frequency bands resulting in an effective center frequency of 143 MHz and a bandwidth of 34 MHz. The lowest contour level corresponds to 3σ significance. The contour levels are plotted at $(-2, 2, 4, 8, \text{etc.})$ times 2.7 mJy beam^{-1}. The RMS is 3.1 mJy beam^{-1}. The beam size (shown in the lower left corner) is $0.459'' \times 0.308''$ with a position angle of $-39.1°$.

ties in the flux values allow for much wider spectral index values to satisfy the fit. We partially mitigate this problem by considering all 11 bands, rather than just the highest and lowest. While this approach provides a reasonable spectral index map quality, the individual values should be treated with caution. Creating a spectral index map between a ILT band and another previous observation at higher frequencies helps to interpret the spectral results with more caution. In Fig. 4.7 the ILT band with a center frequency of 138 MHz and an observation at 1.6 GHz (from the MERLIN observation on 1 March 2008; see Hummel et al. 1992) was used to calculate the spectral index map. Following the same analysis as before, we find that the core again appears to be roughly flat (note that the core can be prone to short time variability affecting the spectral index, since the observations were not simultaneous - ILT in 2015 and MERLIN in 2008). The southern component shows a spectral index of about -0.7 between 138 MHz and 1.6 GHz. Therefore, there is no significant change in the slope for the intra-ILT data and ILT to MERLIN data within the given accuracy. The steep-spectrum halo is faintly visible and its spectral slope is consistent with the intra-ILT spectral index map.

Comparing both spectral index maps, it is clear that the south-west emission region has a steep spectral index. The central emission region appears as a core-halo structure. Since the ILT provides a higher sensitivity for the halo region, which shows a steep spectrum, it is possible to model the central region with the ILT data as two superimposed Gaussian components in the image domain. The core is modelled with an un-

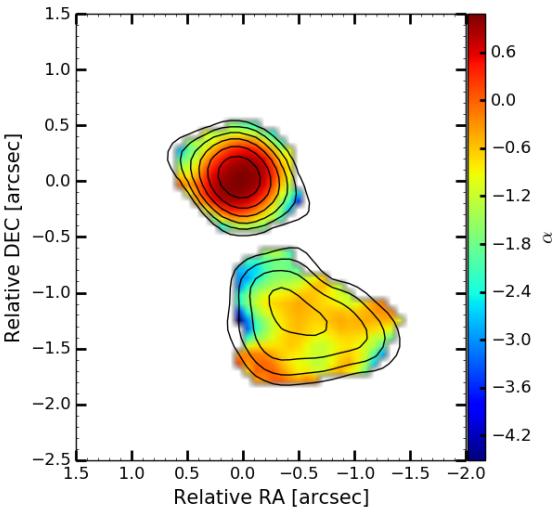

Figure 4.6: Spectral index map (Kappes et al. 2019) of 11 frequency bands fitted to the model pixel by pixel. The contour levels are obtained from the 129 MHz image drawn at (−2, 2, 4, 8, etc.) times 15 mJy beam^{-1}. See the online material for images of the individual bands from which this map was produced.

resolved bright Gaussian component, while the halo has a fainter, broader extension. Subtracting the modelled unresolved core component from the brightness distribution results in Fig. 4.8. This residual image clearly shows a second diffuse emission, otherwise blended by the bright core, with a central offset of about $\lesssim 0.01$ arcsec from the core. It's size is comparable to the diffuse emission region in the southwest and has a flux density of (1.2 ± 0.2) Jy (an intrinsic luminosity of $(4.1 \pm 0.7) \cdot 10^{29}$ W Hz^{-1}).

4.1.5 Discussion

This section presents the evidence that the large-scale morphology of S5 0836+710 can be understood as a classical FR-II radio galaxy seen at a small inclination angle. In this model, the southern component can be understood as a face-on hotspot, hotspot relic or hotspot-lobe structure of the approaching jet, whereas the halo is associated with hotspot and/or lobe emission on the counterjet side. In addition, the observational parameters can be used to derive the jet parameters and to place constraints on the density of the ICM surrounding the radio source S5 0836+710.

Interpretation of the Southern Emission Region

The southern component in S5 0836+710 has a spectral index that is only moderately steep and doesn't reach values expected from a disrupted jet radio relic, as seen in other sources (Pandey-Pommier et al. 2016). At the south-eastern edge, the magnetic field in this region has a circumferential orientation (O'Dea et al. 1988), typical for

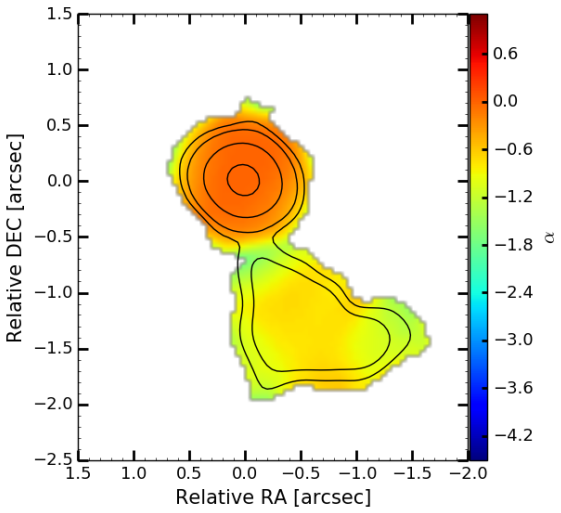

Figure 4.7: Spectral index image (Kappes et al. 2019) between 1.6 GHz (MERLIN) and 138 MHz (LOFAR). The contour levels are obtained from the MERLIN image and are drawn at (−2, 2, 4, 8, etc.) times 30 mJy beam^{-1}.

quasar hotspots (Swarup et al. 1984), and appears to align with the western region of the large-scale structure. This alignment suggests that the emission region is associated with a hotspot and a lobe where the field aligns with the shock to the west, as seen in other FR-II sources (Kharb et al. 2008).

To test whether the size of the southern component is consistent with an active FR-II hotspot region observed face on, a Gaussian component was modelled on the LOFAR data in all 11 bands. The resulting measurements show that the full extent of the emission region is about 9 kpc, with an average flux density of (1.4 ± 0.3) Jy, giving an intrinsic luminosity of $(5 \pm 1) \times 10^{29}$ W Hz^{-1}. Given the distance of 17.88 Mpc, this size is consistent with typical hotspot diameters in powerful FR-II radio galaxies (Jeyakumar & Saikia 2000; Perucho & Martí 2003; Kawakatu & Kino 2006).

An alternative model representation is to model only the brightest peak of the southern component using a Gaussian with a diameter of about 5 kpc and a flux density of (1.2 ± 0.2) Jy. The residual emission at slightly larger spatial scales can be represented by an additional, broader Gaussian or by a hybrid model involving a distribution of CLEAN components. The latter would correspond to a physical scenario of a hotspot surrounded by a lobe, with the high surface brightness feature still consistent in size with typical hotspots in FR-II radio galaxies.

The unusual irregular morphology of the putative hotspot may be due to the high

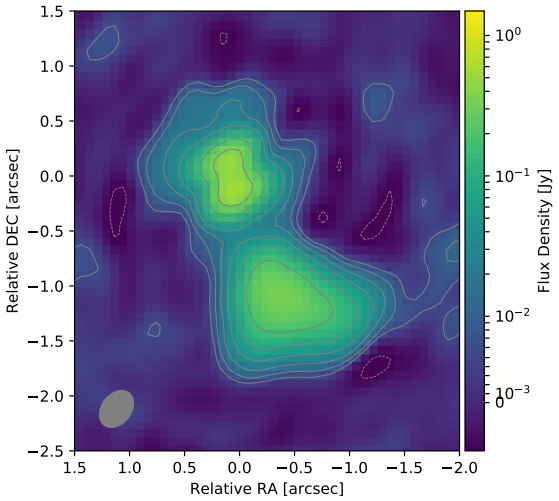

Figure 4.8: LOFAR residual image (Kappes et al. 2019) after subtraction of the 2D Gaussian modelled core component. The lowest contour is at 3σ significance. The contour levels are shown at $(-2, 2, 4, 8, \text{etc.})$ times 2.7 mJy beam^{-1}. The RMS is 3.1 mJy beam^{-1}. The beam size (shown in the lower left corner) is $0.459'' \times 0.308''$ with a position angle of $-39.1°$.

angular resolution and small inclination angle of the AGN. According to Perucho et al. (2012b), if this southern emission component represents the relic of the hotspot after the jet has been transformed into a subrelativistic or mildly relativistic broad flow, the loss of collimation must have occurred quite close to the terminal feature. This is indicated by the fact that the hotspot has not expanded significantly since then.

Interpretation of the Source Morphology

The kiloparsec-scale structure of S5 0836+710 can be characterized as a double-sided source, resembling a highly projected image of a radio galaxy with a strongly radiating, unresolved core component superimposed. This implies that the southern diffuse component is associated with the hotspot region of the approaching jet, while the halo-like diffuse component near the core can be identified as the counter-hotspot region. However, the system cannot be completely symmetric, as the hotspot is further away from the core than the counter-hotspot. Nevertheless, the small inclination angle of the system can increase intrinsically small bends or misalignments to much larger apparent offsets in the projection.

A possible geometry of the system, as introduced in the Sect. 1.2.1, is shown in Fig. 1.3. This interpretation sheds light on the kiloparsec-scale structure of S5 0836+710 and highlights the complex nature of such sources. The results suggest that system geometry and projection effects must be taken into account when analysing the morphology

of radio galaxies to avoid misinterpretation of the data.

By interpreting the southern emission feature as the hotspot region and the halo component near the core as the counter-hotspot region, the brightness ratio of the two regions can be calculated as $F_h/F_{ch} = (1.19 \pm 0.11)$. This ratio is useful in constraining the parameter space for the inclination angle, misalignment and forward velocity β_h of the jet head. This velocity is assumed to be the same for both hotspots and to be slightly relativistic, with values up to 0.1c to 0.5c in FR-II radio galaxies (O'Dea et al. 2009), depending on the deviation from the minimum energy conditions. Differential boosting effects can be seen at such small inclination angles.

Based on the spectral index of $\alpha = -0.7$, the measured brightness ratio of the two hotspot regions, and the estimated viewing angle of $\theta = 3.2°$ from Pushkarev et al. (2009), the allowed parameter space can be determined with Equation (1.10), which is shown in Fig. 4.9. The resulting jet head advance speed is only weakly dependent on the geometry for a given flux ratio. Taking into account the uncertainty range of the flux ratio, the feed rate is restricted to the range 0.010 c to 0.036 c. This is similar to the advance velocities of distant high-power FR-II radio galaxies, although at the lower end of the distribution (O'Dea et al. 2009).

Assuming that hotspot velocities in active FR-II radio galaxies are relatively constant throughout the lifetime of the source, the inferred advance velocity for S5 0836+710 suggests that the source is between 2×10^7 and 8×10^8 years old. However, this exceeds the maximum total source lifetime for such a powerful source by a factor of 2 to 80, as suggested by previous studies (e.g., O'Dea et al. 2009; Perucho et al. 2019). It is therefore likely that the rate of hotspot advance in S5 0836+710 was higher in the past. This is consistent with the idea that the highly relativistic jet has changed to a slightly relativistic flow due to instabilities, as proposed by Perucho et al. (2012b).

The apparent opening angle (core to hotspot) of the hotspot region in S5 0836+710 was determined by modelling each band with a single Gaussian component. The average of all the bands gives a measurement of $(25 \pm 2)°$. From this result it can be concluded that the inclination angle is unlikely to be much larger than 15°, since a larger angle would imply an intrinsic opening angle of $\gtrsim 7°$. Conversely, it is unlikely that the inclination angle is much smaller than 1.5°, since this would result in a deprojected source size larger than the maximum known sizes of radio galaxies (Jeyakumar & Saikia 2000). The preferred inclination angle of $\theta = 3.2°$ (Pushkarev et al. 2009) combined

with the measured apparent opening angle implies an intrinsic opening angle of about 1°, consistent with the results of Hummel et al. (1992).

A constraint on the inclination and misalignment angles can be inferred from the distance of the hotspot and counter-hotspot regions from the core. Specifically, the hotspot region is observed at a distance of about 1.5 arcseconds from the core, while the counter-hotspot region is within about 0.5 arcseconds of the core, beyond which the core and counter-hotspot begin to merge. Based on this, an offset angle of at least 2.5° is required.

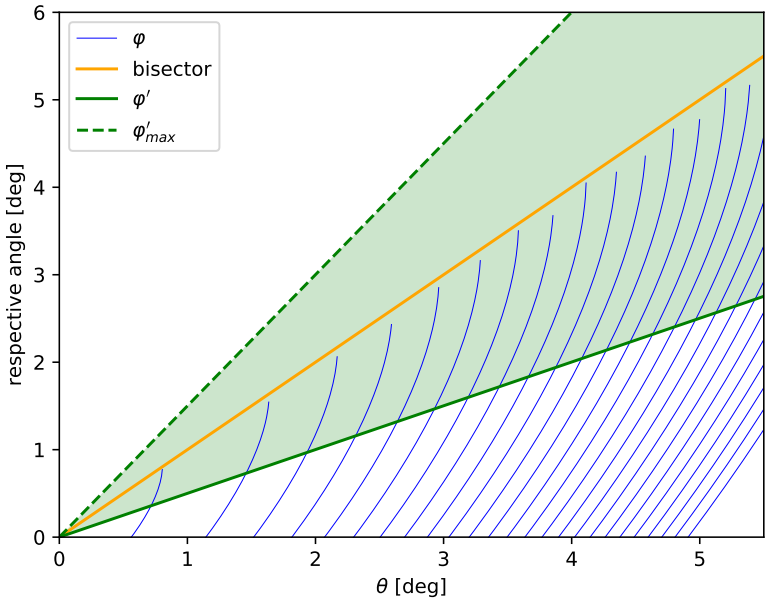

Figure 4.9: The plot published in Kappes et al. (2019) shows the φ lines in the figure, which represent the misalignment angles required to explain the observed flux ratio for a given β value. The β values are shown as arcs ranging from 0.02339 (leftmost arc) to 0.02348 (rightmost arc) in steps of $3.4 \cdot 10^{-6}$. The minimum required misalignment angle is denoted by φ', while φ'_{max} represents the maximum possible misalignment angle based on the geometric argument described in the text. The shaded green region between these two lines represents the possible range of misalignment angles necessary to account for the blending of the counter-hotspot region with the bright core.

The misalignment angle φ required to explain the observed morphology and hotspot region brightness ratio is in the range of 2.5° to 5°. This range is consistent with the typical inclination angles of blazars towards Earth and provides a relatively large parameter space for the particular case of S5 0836+714. In the case of misalignment angeles, such values are common for powerful FR-II radio galaxies, with misalignment angles in 3C sources known to be up to 12° or more (Leahy & Williams 1984). Based on these

considerations the interpretation of the large-scale morphology of S5 0836+710 as an FR-II radio galaxy at a small viewing angle appears to be realistic.

Jet Parameters

According to the estimate provided by Vega-García (2018), the mean magnetic field along the 1.6 GHz jet of S5 0836+710 is limited to $B \lesssim 0.01\,\mathrm{G}$, taking into account the cooling time of the electrons emitting at this frequency and the distance over which the jet is observed. This upper limit on the field strength applies because adiabatic cooling is not significant on the observed scales. Using this value, the radius of the jet at half its extension, and the Lorentz factor for the VLBI jet ($\Gamma_\mathrm{j} = 12$), Vega-García (2018) derived a jet Poynting flux $L_p = \frac{(B^\phi)^2}{4\pi} v_\mathrm{j} \pi R_\mathrm{j}^2 \simeq 2.8 \times 10^{45}\,\mathrm{erg/s}$, assuming the dominant field is toroidal.

Alternatively, the estimate of the jet kinetic power is based on the intrinsic hotspot plus counter hotspot luminosities at 150 MHz ($9.0 \times 10^{29}\,\mathrm{W\,Hz^{-1}}$) and the relation given by Daly et al. (2012) between the source luminosity at 178 MHz and the jet kinetic power. This gives $L_\mathrm{j} \simeq 10^{47}\,\mathrm{erg/s}$, although this value is subject to considerable uncertainty. Nevertheless, it is consistent with the expected kinetic power for powerful FR-II jets such as this bright and distant quasar. By comparing the total energy flux with the Poynting flux, it can be inferred that the jet is likely to be kinetically dominated at these scales. Furthermore, a stability analysis of the jet confirms that its Mach number is large, indicating that it is in the cold regime ($h_\mathrm{j} \simeq c^2$ and implying $\gamma_\mathrm{j} \simeq 5/3$, Vega-García et al. 2019) but is kinetically relativistic at VLBI scales. With the jet being kinetically dominated and in the cold regime (i.e. its magnetosonic Mach number is high), whereas the measured advance speed as measured by LOFAR is so slow that the velocity of the bulk plasma flowing into the hotspot can be assumed to be at most mildly relativistic. Under these conditions, the magnetic and pressure terms can be neglected and Equation (1.11) is simplified to

$$L_\mathrm{j} = \frac{1}{2} v_\mathrm{j}^3 \rho_\mathrm{j} A_\mathrm{j}. \tag{4.1}$$

The hotspot pressure (e.g., Landau & Lifshitz 1987) across a strong shock is

$$P_\mathrm{h} \simeq \frac{4 L_\mathrm{j}}{(\gamma_\mathrm{j} + 1) v_\mathrm{j} A_\mathrm{j}}. \tag{4.2}$$

To define the jet radius at the hotspot in this equation, it must be approximated as the radius of the hotspot. It is uncertain whether the southern radio structure includes the hotspot and part of the lobe, or whether it is the hotspot. Half of the whole

Table 4.1: The parameters of the jet at the hotspot are shown, with the intervals corresponding to the values obtained for $r_h = 4.5$ and 2.5 kpc.

β_h	$\beta_{j,h}$	$\rho_{j,h}$	$B^{\phi}_{j,h}$	P_h	B^{ϕ}_h	ρ_a
[1]	[2]	[3]	[4]	[5]	[6]	[7]
0.01	0.23	$1.2-3.8\times10^{-27}$	0.04 – 0.08	$0.4-1.3\times10^{-7}$	1.0 – 1.8	$0.5-1.5\times10^{-24}$
0.036	0.54	$0.9-2.9\times10^{-28}$	0.04 – 0.08	$1.8-5.7\times10^{-8}$	0.7 – 1.2	$1.5-5\times10^{-26}$

Col. [1]: hotspot advance speed in units of c; Col. [2]: jet speed in units of c; Col. [3]: density before the reverse shock in units of g cm^{-3}; Col. [4]: magnetic field before the reverse shock in units of mG; Col. [5]: hotspot pressure in units of dyn/cm^2; Col. [6]: magnetic field in the hotspot in units of mG; Col. [7]: density of the environment in units of g cm^{-3}.

region was considered as the jet radius (4.5 kpc) and half of the fitted component corresponding to the brightest region within the hypothetical lobe (2.5 kpc). Both cases have been investigated, although the polarisation seems to favour the latter interpretation. Moreover, an estimate for v_j at the hotspot, $v_{j,h}$, was required. The following paragraphs demonstrate an iterative method to derive its convergence value. Once the hotspot pressure is obtained, the equipartition between the non-thermal particles and the magnetic field can be used to determine the value of the magnetic field at the interaction site, as reported for FR-II hotspots (see e.g. Hardcastle & Worrall 2000).

Assuming conservation of magnetic flux from the 1.6 GHz jet to the interaction site, one can constrain the value of the magnetic field before the reverse shock $B^{\phi}_{j,h}$. This assumption is reasonable for conically expanding jets on the kiloparsec scale (see e.g. Komissarov 2012). Applying the **M**agneto**H**ydro**D**ynamics (MHD) jump conditions to the reverse shock that gives rise to the hotspot,

$$v_{j,h} B^{\phi}_{j,h} = v_h B^{\phi}_h, \tag{4.3}$$

enables the derivation of a new estimate for $v_{j,h}$. By setting a convergence criterion for this parameter to an accuracy of 10^{-3}, the relevant parameters of the problem can be determined.

Four different sets of hotspot velocity and radius were analysed using this method: the possible combinations of $v_h = 0.01 - 0.036\,c$ and $R_{j,h} = 2.5 - 4.5$ kpc. The resulting values are given in Table 4.1. The parameter ranges given correspond to the values obtained for $r_h = 4.5$ and 2.5 kpc, and the smaller values of pressure, magnetic field and density correspond to the wider hotspot.

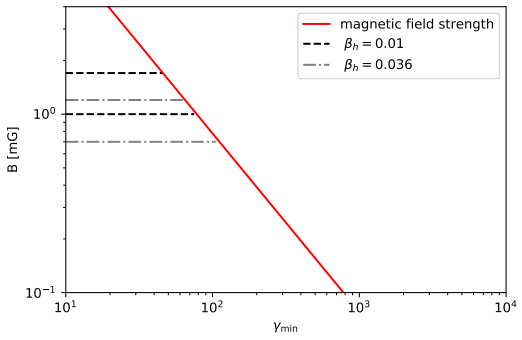

Figure 4.10: The magnetic field strengths presented in Kappes et al. (2019) of the southern hotspot are in the range of $0.7 \leq \frac{B}{\mathrm{mG}} \leq 1.8$ based on the minimum energy assumption as described in Pyrzas et al. (2015).

The analysis suggests that the velocity of the jet at the interaction site is significantly lower than that of the VLBI jet. This can be attributed to kinetic energy dissipation caused by growth of the KH modes and/or integrated entrainment along the jet (e.g., Perucho et al. 2012a,b). The extreme value of $\beta_{\mathrm{j,h}} = 0.54$, obtained for $\beta_{\mathrm{h}} = 0.036$, supports the assumption of a mildly relativistic flow, since possible relativistic corrections are limited by the Lorentz factor $\Gamma_{\mathrm{j,h}} \lesssim 1.2$.

The magnetic field values obtained from our spectral analysis using basic synchrotron theory are shown in Fig. 4.10 as a function of the minimum electron Lorentz factor, derived using Equation (6) in Pyrzas et al. (2015). The magnetic field derived from the equipartition assumption in the hotspot region gives a value of $\gamma_{\mathrm{min}} \leq 100$, which is within the expected range (Meisenheimer et al. 1989, 1997).

Comparing the parameters listed in Table 4.1 with those obtained by Meisenheimer et al. (1989) for various classical FR-II hotspots using spectral analysis, it is observed that the hotspot region values for pressure and magnetic fields are around or slightly above their maximum values ($B_{\mathrm{h}} \sim 0.1-1\,\mathrm{mG}$ $P_{\mathrm{h}} \sim 0.1-1\times10^{-8}\,\mathrm{dyn/cm^2}$ in their case). Considering that S50836+710 is a powerful jet that is likely to interact with a dense ICM, it can be concluded that the derived parameters are consistent with the typical values obtained by Meisenheimer et al. (1989) using a different methodology.

Using the derived parameters from Table 4.1, we can estimate the jet density prior to the reverse shock using Equation (1.12). The results are also shown in Table 4.1. The jet number density within the hotspot region ranges from $n_{\mathrm{j,h}} = 0.1-4.0,\mathrm{cm^{-3}}$ if the mass flux is dominated by pairs, or $n_{\mathrm{j,h}} = 0.05-2.3\times10^{-3},\mathrm{cm^{-3}}$ if it is dominated by protons.

Assuming a leptonic jet, the total number of particles flowing through the hotspot can be estimated using the formula $N_{\mathrm{j,e}} = \Gamma_{\mathrm{j,h}} v_{\mathrm{j,h}} n_{\mathrm{j,h}} \pi R_{\mathrm{j,h}}^2 \simeq 1.2 - 5.5 \times 10^{54}$ pairs/s at the hotspot. However, such a pair jet can be ruled out by energetic considerations, since the relativistic jet at VLBI scales must have altered the energy flux in terms of rest mass energy. As a result, proton contamination must have occurred along the jet, indicating that the jet is likely to be proton-dominated at large scales. The flux is reduced to $0.6 - 3.0 \times 10^{51}, \mathrm{s}^{-1}$ in the case of a proton-dominated jet at these scales.

Intracluster Medium Implications

Using ram pressure confinement, a lower limit of $\rho_{\mathrm{a}} = P_{\mathrm{h}} / v_h^2 \simeq 1.5 \times 10^{-26}\,\mathrm{g\,cm^{-3}}$ and an upper limit of $1.5 \times 10^{-24}\,\mathrm{g\,cm^{-3}}$ are obtained for the density of the environment, depending on the range of R_j and v_{h}. The highest derived value corresponds to the lowest hotspot advance speed and implies proton number densities of $\sim 1\,\mathrm{cm^{-3}}$, which is unrealistically high for the ICM at 240 kpc from the active nucleus. However, increasing the hotspot advance speed to 0.036 c yields values as low as $\sim 0.01\,\mathrm{cm^{-3}}$. The results favour hotspot advance speeds in the upper part of the interval given by the brightness asymmetry. Nevertheless, the results are still one to two orders of magnitude higher than those found by O'Dea et al. (2009). Although S5 0836+710 probes the ICM density at an earlier stage in the evolution of the Universe, the study of a single source does not allow any conclusions to be drawn about possible systematic cosmological effects. It is possible that S5 0836+710 is located within a particularly overdense cluster such as Cygnus A. However, the method employed can potentially be applied to large samples of powerful blazars and has the potential to reach even higher redshifts.

4.1.6 Conclusion

The sensitivity and angular resolution of the ILT in the 100 MHz regime is unprecedented. The international LOFAR stations can be used as an effective VLBI array when dealing with compact sources that have structure only on angular scales of arcseconds or less. Improved calibration techniques can lead to further improvements in image fidelity with the inclusion of the Dutch core array stations and future observations from the new international stations in Poland, Ireland and Italy, providing a maximum baseline of about 1900 km. The unique capabilities of LOFAR are crucial for blazar observations due to their small angular scales and the dominance of the emitted core over the extended structure at higher frequencies. Future studies of blazar samples with LOFAR will help to resolve open questions about the unification of blazars and

radio galaxies. These questions include the occurrence of morphological features in BL Lac objects that are typical of FR-II galaxies, as reported by Cooper et al. (2007) and Kharb et al. (2010).

This study shows that blazar observations with LOFAR can be used to probe the density of the intergalactic medium at cosmological distances. The results suggest that the density around the distant blazar S5 0836+710 is higher than in less distant FR-II radio galaxies, but the study is limited to a single source, and generalising to a systematic redshift dependence requires taking into account source-specific peculiarities and systematic uncertainties. The method can be extended to larger samples of blazars to derive statistically relevant samples of ICM density as a function of redshift, complementing classical observational methods applied to radio galaxies. Blazars can be found at higher redshifts, making the method potentially important for studying the early universe. However, detecting weakly radiating components such as hotspots and lobes at redshifts beyond $z = 2$ will be challenging and may require the capabilities of the SKA.

4.2 Studies of GB 1508+5714

While the previous study, discussed in Sect. 4.1, used an early version of a calibration pipeline for a distant blzar, with the aim of demonstrating the ability to study distant blazar populations, test their connection to radio galaxies, and examine their environment. This section demonstrates the use of a much more mature calibration pipeline, as described in Sect. 3.5.3. Here the high redshift blazar GB 1508+5714 ($z = 4.30$) should be subject to the interaction with CMB photons, as introduced in Sect. 1.3.

4.2.1 Scientific Interest

Radio-jetted AGN have remarkable luminosities, making them observable at extreme redshifts and allowing their properties to be used as observational probes of cosmological principles (Wang et al. 2021). Blazars in particular have boosted apparent luminosities due to relativistic boosting effects (Cohen et al. 2007b), allowing them to be detected over a wide range of the electromagnetic spectrum. However, they are observationally compact objects with small angles between their jets and the line of sight. AGN with radio jets at larger angles to the line of sight, known as radio galaxies, become more difficult to detect with increasing distance. These AGN can be observed over a wide range of redshifts, providing a unique insight into cosmology, galaxy

evolution and the evolution of AGN (Dunlop & Peacock 1990; Georgakakis et al. 2017). It is not enough to observe targets at different redshifts; one must also consider their evolutionary stage, the environment in which they are embedded at that time, and their interactions with that environment.

Several radio surveys have examined radio-loud AGN populations, including those by Becker et al. (1995), Condon et al. (1998), Cohen et al. (2007a), and Intema et al. (2017), which have found consistent relative number ratios of radio galaxies and blazars up to a redshift of about 3 (Volonteri et al. 2011). Beyond this redshift, however, there are uncertainties due to density evolution and the formation of large black hole masses in the early universe (Blundell et al. 1999; Shankar et al. 2008). Nevertheless, there appears to be a deficit of higher redshift radio galaxies, even taking into account evolutionary effects and detection limits (e.g. Wu et al. 2017; Hodges-Kluck et al. 2021, and references therein). The cause of this deficit is not fully understood. One explanation, proposed by Ghisellini et al. (2015), is that the extended radio emission interacts with the CMB to efficiently reduce the brightness of the extended radio lobes. Morabito & Harwood (2018) have found evidence for this model by comparing simulations and observational data.

According to this model (see Sect. 1.3), at very high redshifts the energy density of the CMB is higher than the magnetic energy density, so that the electrons in the jet are cooled by inverse Compton scattering of CMB photons. This leads to a suppression of the synchrotron radiation. However, the isotropic radiation from the extended structures with steep spectra can still be detected by telescopes operating in the long-wavelength radio regime. These observations can be used to test and refine theoretical models.

4.2.2 Previous Studies

The study by Ghisellini et al. (2015) identified a list of blazars that can be used to investigate the suppression of extended radio emission at high redshifts, and provided predictions for radio fluxes under different model parameters. In particular, it was shown that the ILT is capable of detecting the extended emission from these blazars and investigating the possible suppression of the emission. From the list presented, the high redshift blazar GB 1508+5714 at $z = 4.30$ (Hook et al. 1995), which is one of the most distant quasars with a detected X-ray jet (Yuan et al. 2003; Siemiginowska et al. 2003), was selected for this work.

Cheung (2004) reports the successful detection of faint radio emission from an X-ray jet in the quasar GB 1508+5714 using archival VLA data. The X-ray emission, detected by Chandra (Yuan et al. 2003; Siemiginowska et al. 2003), is interpreted as IC emission from the CMB, and the high X-ray to radio monochromatic luminosity ratio is attributed to the high redshift of the quasar. The author suggests that this discovery may provide important insights into the physics of jet formation and evolution in high-redshift quasars.

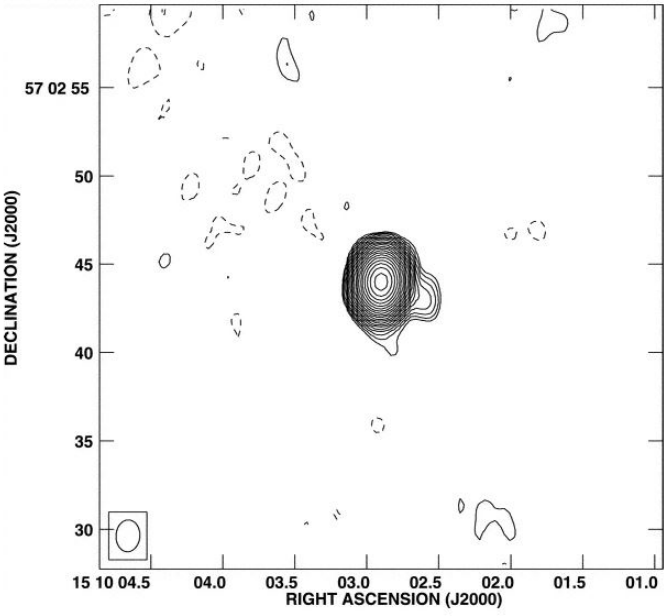

Figure 4.11: This image is a naturally weighted snapshot taken from VLA archive data at 1.4 GHz, showing quasar GB 1508+5714 at its center. A ~ 2.5 arcsecond long radio jet extending to the south and west of the quasar is visible in the image. The contours start at 0.25 mJy beam^{-1}, which is twice the measured **R**oot **M**ean **S**quare (RMS) in the image. Positive values are represented by solid contours spaced by factors of $\sqrt{2}$, with an image peak at 224 mJy beam^{-1}. The restoring beam is shown in the lower left corner of the image and has dimensions of 1.8 × 1.35 arcseconds at a position angle of −3.61°. Credit: Cheung (2004).

4.2.3 Observation and Data Reduction

On 15 June 2015, the HBA array of the ILT observed GB,1508+5714 in dual outer mode, with the target positioned in the phase center. The observation included nine international stations, namely DE601HBA, DE602HBA, DE603HBA, DE604HBA, DE605HBA, DE609HBA, FR606HBA, SE607HBA and UK608HBA. The observation time was 4 hours, covering 110 MHz to 190 MHz with a time averaging of 16 s and a frequency channel width of 12.2 kHz. A flux density calibrator, 3C196, was used with a ten minute calibration observation prior to the target observation. The data retrieved

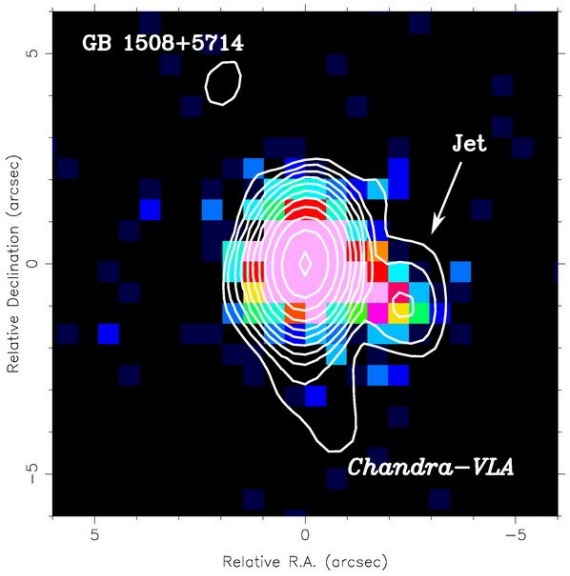

Figure 4.12: This image is a Chandra X-ray image of the quasar GB 1508+5714 (shown in color), overlaid with a VLA 1.4 GHz image. The data used for the X-ray image are from the archive data published in Yuan et al. (2003) and Siemiginowska et al. (2003). The radio image is from the same data shown in 4.11, but restored with a uniformly weighted beam (1.52 × 1.03 arcseconds at a position angle of −4.44°). The blazar is located at the origin of the image, with the jet feature indicated. The lowest plotted contour is 0.2 mJy beam^{-1}, and subsequent contours are spaced by a factor of 2. Credit: Cheung (2004).

from the LTA were processed with PREFACTOR[3] version 3.0 (de Gasperin et al. 2019) to obtain calibration solutions for all stations, including polarisation alignment, clock, bandpass and rotation measurements using the calibrator. Phase solutions were obtained for the core and remote stations in the target field. This step is necessary before proceeding with the LOFAR-VLBI pipeline[4], which uses these solutions to initiate the phase calibration of the international stations. The final frequency coverage ranged from 128 MHz to 160 MHz in four sub-bands of 8 MHz bandwidth due to the presence of strong RFI in the data. The final full-band image was centered on a frequency of 144 MHz and the data was time-averaged over 16 s.

A virtual superstation has been created by combining all the core stations, resulting in a reduction in data size and simplified data handling, as well as a significant reduction in I/O (for more detailed information on the LOFAR-VLBI pipeline, see Morabito et al. 2021). Due to poor visibility data quality, the remote stations RS503HBA, RS407HBA, RS406HBA and the international stations FR606HBA and SE607HBA were removed from the dataset. The poor quality may have been due to problems at the station

[3] Github repository https://github.com/lofar-astron/factor
[4] Github repository https://github.com/lmorabit/lofar-vlbi

level or with the model of 3C196 used in the initial calibration. Diagnostic plots indicated good ionospheric conditions overall, suggesting that the problems were due to the quality of the calibrator models at the time of reduction. It is expected that this issue will be resolved in the future as better models become available. The final (u, v)-coverage is shown in Fig. 4.13.

The imaging process was carried out by three independent parties with no prior knowledge of the expected structure to test the robustness of the results. They also started the self-calibration process with different starting models to ensure that the final image was independent of the starting model. To verify the reality of the structure in the eastern direction, it was excluded from the model supplied to the self-calibration step and it was found that the structure persisted despite this exclusion. In all cases, further self-calibration and imaging was done using DIFMAP (Shepherd 1997). Time and bandwidth smearing do not have a major effect on the final image as the target is in the phase center. A more in-depth analysis to this can be found in Bonnassieux et al. (2020). The loss of intensity was calculated as a function of distance from the phase center using equations 18–43 for time smearing and 18–24 for bandwidth smearing from Bridle & Schwab (1999). Smearing remains below 5% at a radial distance of about 6”, corresponding to the full extent of the source, indicating that this effect can be considered negligible in the subsequent analysis.

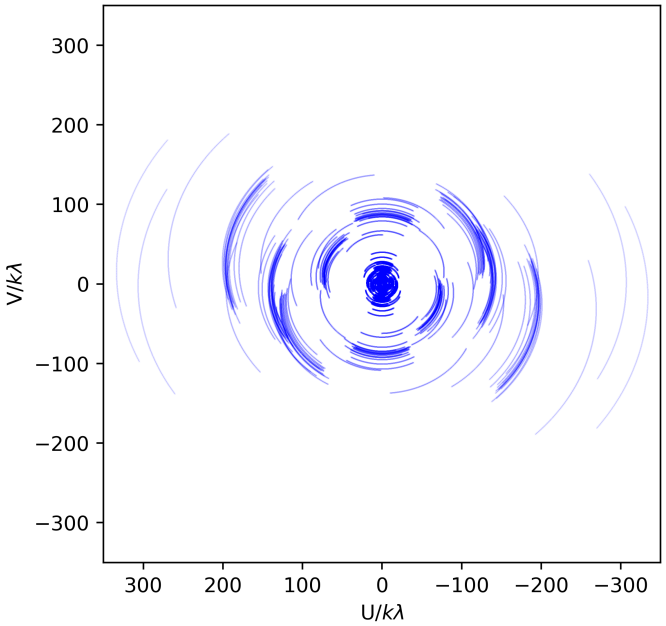

Figure 4.13: (u, v)-coverage for the ILT dataset at 144 MHz with the target GB 1508+5714 located in the phase center, observed on 15 June 2015 for 4 hours, presented in Kappes et al. (2022).

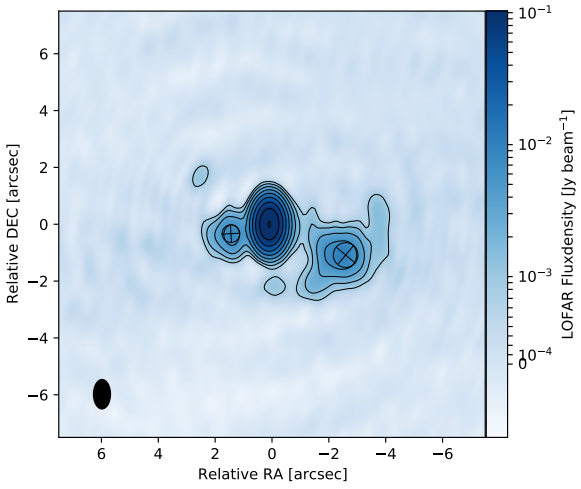

Figure 4.14: The ILT image presented in Kappes et al. (2022) of GB 1508+5714 at 144 MHz. The source brightness is color coded by flux density, with the contour lines superimposed. The crossed circles indicate the modelled Gaussian components as hotspots. The contour levels are drawn at $(-1, 1, 2, 4, 8, \ldots)$ times 0.78 mJy beam^{-1}. The RMS is 0.13 mJy beam^{-1}. The restoring beam size (shown in the bottom left) is $1.08'' \times 0.643''$ with a position angle of $-0.27°$.

4.2.4 Results

After following the described calibration and imaging steps, a final image (shown in Fig. 4.14) is obtained. The core component in the center of the image contributes most of the flux density ($\sim 86\%$). Significant bright and resolved emission is observed to the east and west of the core, with the western component appearing brighter than the eastern. The largest extension of the whole structure is about 6" (~ 41 kpc).

Previous observations with the VLA (Cheung 2004) are in good agreement with the LOFAR image. For a direct comparison, Fig. 4.15 shows the contour lines from the VLA observation at 1.43 GHz superimposed on the LOFAR brightness distribution. The calibrated archival VLA data[5] came from a single five-minute snapshot observation in the A configuration. This yielded a 10σ detection of the western component containing about 1.2 mJy. The core flux density is (224 ± 11) mJy at 1.43 GHz at the time of the VLA observation.

Despite the longer wavelength, the ILT image has a better angular resolution than the VLA. The eastern component has a steep spectrum and is therefore much fainter and appears unresolved at 1.43 GHz. The eastern component seen by LOFAR is not clearly detected by the VLA (see Cheung 2004). This component is also not seen in the

[5] https://hea-www.harvard.edu/XJET/img-data.cgi?1508_vla_2ghz_1995jul.txt

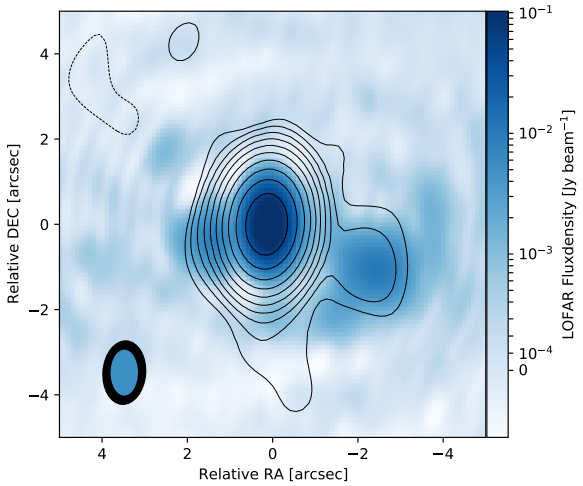

Figure 4.15: The image (Kappes et al. 2022) shows GB 1508+5714 observed at 144 MHz using the ILT, accompanied by the 1.43 GHz VLA contours from Cheung (2004). The restoring beams for the ILT and VLA are depicted as blue and black ellipses respectively, situated in the bottom left corner. VLA contour levels are plotted at multiples of 0.23 mJy beam^{-1}, starting from −1 and increasing (e.g., $-1, 1, 2, 4, 8, ...$). The RMS in the VLA data is measured at 0.20 mJy beam^{-1}. The restoring beam size is $1.52'' \times 1.03''$ with a position angle of −4.44° for the VLA, and $1.08'' \times 0.643''$ with a position angle of −0.27° for the ILT.

Chandra X-ray image, although the resolution is comparable to that of the ILT image (McKeough et al. 2016).

The LOFAR observation (with a beam size of $1.08'' \times 0.643''$ at a position angle of −0.27°) has been reconvolved with the beam parameters of the VLA observation (with a beam size of $1.52'' \times 1.03''$ at a position angle of −4.44°), as shown by the contours in Fig. 4.16. A very good visual match is seen, with the reconvolved LOFAR observation still showing a prominent resolved emission component to the east of the bright core. In comparison, the VLA observation shows only marginal evidence of an extension in this direction. This is consistent with the component having a steep spectral index.

By combining the reconvolved LOFAR data with the VLA data, performing an alignment correction, and fitting a power law for each pixel with a flux value above a 2σ threshold (σ being 0.13 mJy beam^{-1} for the ILT image and 0.20 mJy beam^{-1} for the VLA image), the spectral index[6] map shown in Fig. 4.16 was calculated. Pixels for which the 2σ threshold is not met in either image are shown in white. The core region shows a flat spectrum, suggesting that the variable flat-spectrum core was in a similar emission state during the LOFAR and VLA observations.A steep spectral index with a median of -1.2 (min = −1.4, max = −0.84) was measured for the western component.

[6] the spectral index α is defined via $S_\nu \propto \nu^\alpha$, with S_ν as the radiative flux density.

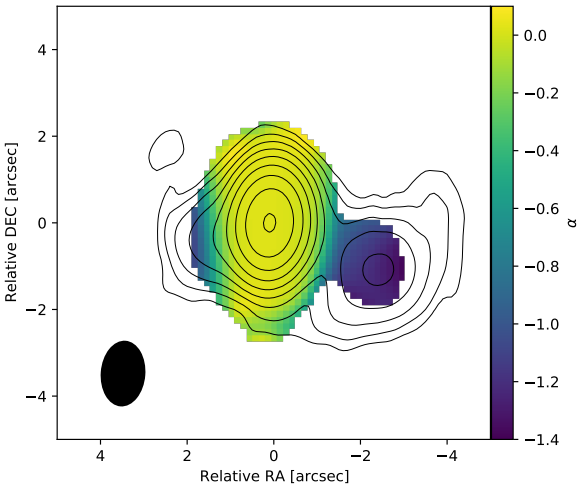

Figure 4.16: Color coded spectral index image between 144 MHz and 1.43 GHz. The contour levels show the flux-density distribution at 144 MHz with $(-1, 1, 2, 4, 8, \ldots)$ times 0.78 mJy beam^{-1}.The joint beam (shown lower left) used to restore both the LOFAR and VLA images is $1.52'' \times 1.03''$ with a position angle of $-4.44°$. Credit: Kappes et al. (2022).

Cheung et al. (2005) reported a spectral index of (-1.4 ± 0.2) between 1.4 GHz and 5 GHz, indicating no significant spectral break between 144 MHz and 5 GHz.

While the measured flux density of the eastern component in the VLA data is not significant enough to meet the flux threshold requirements, there is a trend of the same steepness, reaching $\alpha \lesssim -1.1$ at the easternmost edge of the spectral index image. This value is an upper limit due to non-detection by the VLA. Comparable values have already been discussed in the first study in Sect. 4.1, which also involved a blazar at a higher redshift, where subarcsecond emission features close to the core were identified as hotspots. Considering that powerful quasars resemble rotated FR-II radio galaxies, in the unification model (Urry & Padovani 1995) observations of nearby FR-II radio galaxies at higher frequencies (taking into account the K correction) can be compared with the measurements. Here flatter spectral indices were observed for hotspot regions (Ishwara-Chandra & Saikia 2000; Harwood et al. 2015).

The LOFAR observation shows a total flux density of $F_{\nu,\mathrm{T}} = (254 \pm 33)$ mJy. To determine the parameters of both components (eastern and western), a one-Gaussian (major axis equal to minor axis) component was used in each corresponding region to model the emission (see crossed circles in Fig. 4.14). The flux density for the western component is $F_{\nu,\mathrm{W}} = (20.5 \pm 2.6)$ mJy, with a diameter of about 0. 87" (~ 6 kpc), and the flux density for the eastern component is $F_{\nu,\mathrm{E}} = (12.7 \pm 1.6)$,mJy, with a diameter of about 0.62" (~ 4 kpc). Similarly, the flux density for the unresolved core component

is $F_{\nu,\mathrm{core}} = (218 \pm 28)$ mJy. The residual flux density of $F_{\nu,\mathrm{R}} = (2.8 \pm 0.3)$ mJy remains unattributed in the model components. The uncertainty in the residual flux density was calculated by considering the RMS in the residual image about 20" from the source, in a box with an area of about 200 beams. This RMS was normalized by the square root of the number of pixels and then converted from mJy beam^{-1} to mJy. The total extended flux density is the sum of the three non-core emission contributions: $F_{\nu,\mathrm{ext}} = (36.0 \pm 3.1)$ mJy.

Modelling

Subsequently, the physical modelling is presented with the obtained data as a reference. This modelling is necessary to determine the observational properties that would be expected from a source with the same physical parameters, but observed in the local Universe, where the CMB energy density is much lower. In the following discussion, these observational properties are plotted as 'no CMB' in Figs. 4.17, 4.18, 4.19 and 4.20. Section 1.3 introduces this effect and describes the underlying emission models. The focus in the following analysis is on the flux density of the extended emission regions. In Ghisellini et al. (2015) these regions were ad hoc assumed to emit between 1% and 10% of the total jet power. The measured value is $\log_{10}(\nu F_{\nu,\mathrm{ext}}) = -16.30^{+0.06}_{-0.05}$ in cgs units. If the spectral index α and the flux density of a given region are known, the corresponding specific luminosity can be determined using the Equation (4.4) from Condon (1988).

$$L_{\mathrm{region}} = \frac{F_{\mathrm{region}} \cdot 4\pi \cdot (c \cdot z)^2}{H_0^2 \cdot (1+z)^{1-\alpha_{\mathrm{region}}}}. \tag{4.4}$$

Assuming a α value of 0 for the core, the intrinsic luminosity $\log_{10}(L_{144,\mathrm{MHz,core}})$ is derived to be 27.2 (in cgs units). Using the minimum (-1.4) and maximum (-0.84) spectral index values for extended regions, we calculate the intrinsic luminosity range with the K-correction, which gives $\log_{10}(L_{144,\mathrm{MHz,ext}})$ between 25.4 and 25.8 (in cgs units), corresponding to 1.6% to 4.0% of the core luminosity. According to Fanaroff & Riley (1974) GB,1508+5714 would be classified as a FR-II radio galaxy (Owen & Ledlow 1994). It should be noted that the K-correction must be taken into account for a proper comparison, since the measurements were made at 1.4 GHz for nearby sources. The observation frequency of about 144 MHz corresponds to an emitted frequency of about 760 MHz, which is below 1.4 GHz. Therefore the FR-II classification for GB 1508+5714 remains valid. GB 1508+5714 belongs to the class of FSRQs, which are considered to be the rotated counterparts of FR-II radio galaxies

within the AGN unification scheme. Recent studies have shown that FR-II radio galaxies can be up to three orders of magnitude below the traditional Fanaroff-Riley break, suggesting that GB 1508+5714 is more appropriately classified as an FR-II object than an FR-I (Mingo et al. 2019). The broadband SED of FSRQs is characterized by thermal emission (i.e. an accretion disk in the optical to UV regime, a torus in the **I**nfra-**R**ed (IR) regime, and possibly a hot corona in the X-ray regime) and non-thermal emission produced by a jet directed at a small angle to the line of sight and thus strongly boosted by relativistic beaming. FSRQs are typically strongly variable at different wavelengths, and simultaneous variations are not uncommon (Meyer et al. 2019; Shukla & Mannheim 2020; Collaboration et al. 2020; Kramarenko et al. 2021; Acciari et al. 2021). The emission is therefore typically modelled as coming from a single region. In single-zone models, the emitting region must not be too close to the accretion disc, to avoid being too compact and thus absorbing all the γ-ray emission in the γ–$\gamma \rightarrow e^+ e^-$ process. Similarly, it cannot be too far away from the accretion disk to explain the observed rapid variability. This gives constraints on the location of the emission source at about $\sim 10^3 - 10^4$ Schwarzschild radii from the black hole (Liu & Bai 2006). All blazars, visible in their SEDs, show two humps: one at low energies, due to synchrotron emission, and another at high energies, due to IC processes (although some hadronic processes may also contribute). For very powerful sources, such as GB 1508+5714, the first hump peaks in the sub-millimeter band and the second hump peaks in the ~,MeV band, for high-energy sources. The last observable quantity is generally the accretion disk emission, which peaks in the UV. For these sources, the disk emission can be modelled to obtain estimates of its luminosity (and hence the accretion rate) and its black hole mass, independently of other methods such as emission line widths and luminosities. The top data points in Fig. 4.17 show the SED produced by the accretion disk, the molecular torus, and the emission from the part of the jet thought to produce most of the non-thermal radiation observed. Unfortunately, measurements in the appropriate IR band are not available to constrain the emission properties of the torus. The model labelled 'no CMB' shows the expected SED in the absence of the CMB interaction at this high redshift. It can be seen that in this case the radio flux density would be enhanced and the X-ray emission strongly suppressed. This shows how a source with the same parameters would appear if it were nearby, where the CMB energy density is much lower (i.e. by a factor of $(1+z)^4 \sim 790$) and therefore does not provide a viable interaction channel for the electrons to cool off.

The flat core-dominated radio spectrum (dashed blue line in Fig. 4.17) extends down to 50 MHz (de Gasperin et al. 2021). This emission is thought to result from the

combination of fluxes produced by progressively larger jet-emitting regions, which are characterized by a self-absorption frequency ν_t inversely proportional to their size (Blandford & Königl 1979). For a conical jet it can be approximated that $\nu_t \propto 1/R_j$, where R_j is the distance from the black hole. Since the Doppler boosting varies significantly with the viewing angle, it can be concluded that the jet does not bend significantly, at least not up to the regions responsible for producing the 50 MHz flux, otherwise the 50 MHz flux would not lie on the ν^0 line.

This implies that $R_j(50\,\mathrm{MHz}) \sim 1.3\,\mathrm{kpc}$, assuming that the flux at 300 GHz originates from the jet region that emits the rest of the jet spectrum. All the jet parameters, listed in Table 4.2 for convenience, are very similar to the blazars detected by the **L**arge **A**rea **T**elescope (LAT) on board the *Fermi* satellite (Atwood et al. 2009) and analysed in Ghisellini & Tavecchio (2015). The power of the jet ($P_{\mathrm{jet}} \sim 3 \times 10^{47}\,\mathrm{erg\,s^{-1}}$) is mainly dominated by the bulk motion of cold protons (assuming that the number of emitting electrons is equal to the number of cold protons, i.e. assuming no significant contribution from electron-positron pairs). The lower bound for P_{jet} is $10^{46}\,\mathrm{serg\,s^{-1}}$, which is the total power in radiation emitted by the jet.

It is important to note that the jet–hotspot–lobe models are a simplified representation of what is likely to be a complex reality. In particular, the lobes and hotspots are idealized as spheres homogeneously filled with tangled magnetic fields and relativistic particles, with no internal gradients. When dealing with extended sources at high redshifts, the contribution of the CMB becomes important, as it can be the dominant source of seed photons to be scattered to high energies. Relativistic electrons can inverse Compton scatter their own synchrotron photons, called SSC, as well as the CMB photons. The latter is called the external Compton process. The energy density of the CMB increases with redshift as $(1+z)^4$, and there is an equipartition between the magnetic (U_B) and CMB (U_{CMB}) energy densities for a magnetic field value B_{eq} given by

$$B_{\mathrm{eq}} = 3.26 \times 10^{-6}(1+z)^2\,\mathrm{G} = 9.2 \times 10^{-5}\left[\frac{(1+z)}{1+4.309}\right]^2\,\mathrm{G}. \tag{4.5}$$

When magnetic fields are weaker than B_{eq}, the high-energy luminosity produced by the external Compton is greater than the synchrotron luminosity due to $U_{\mathrm{CMB}} > U_B$. X-ray measurements from Chandra have detected a diffuse extended component (butterfly spectrum in Fig. 4.17) (Siemiginowska et al. 2003; Yuan et al. 2003). Assuming the external Compton process is responsible for this X-ray component, we can use the ratio of its luminosity to the extended radio luminosity to estimate the ratio U_{CMB}/U_B. The

ratio ranges between two and three orders of magnitude, which allows an upper limit to be placed on the value of the magnetic field of the extended components (hotspots and/or lobes), denoted as $B_{\rm ext}$, using Equation (4.6).

$$\frac{L_{\rm X,ext}}{L_{\rm syn}} \sim \frac{U_{\rm CMB}}{U_B} \rightarrow B_{\rm ext} \lesssim \left[\frac{8\pi U_{\rm CMB}}{L_{\rm X,ext}/L_{\rm syn}}\right]^{1/2}, \tag{4.6}$$

This gives $B_{\rm ext} \lesssim 3\ \mu$G for $L_{\rm X,ext}/L_{\rm syn} = 10^3$. This estimate is independent of the volume of the region emitting the diffuse X-rays and can be applied to both the lobe and the hotspots, depending on which structure is responsible for the diffuse X-ray flux.

The power in relativistic electrons $P_{\rm e}$ injected into the hotspots and lobes is determined by ensuring that they produce the observed X-ray luminosity $L_{\rm X,ext}$. If the CMB dominates the radiative cooling, the volume of the lobe is irrelevant and $P_{\rm e}$ remains independent of it. The particle distribution is self-consistent, rather than fixed, by a continuity equation that takes into account the cooling terms (synchrotron, SSC, external Compton, adiabatic). To determine the effects of the CMB, the total power injected into the relativistic electron population and its shape (a broken power law, very hard at low energies and steeper after a break) are given, allowing to determine the emission distribution. Above the energy cooling break $E_{\rm cool}$, corresponding to the synchrotron frequency $\nu_{\rm cool}$, the CMB dominates the radiative cooling and the particle distribution becomes steeper, suppressing the synchrotron emission above this frequency. A more detailed description is given in Sect. 1.3, based on the studies of Ghisellini et al. (2014) and Ghisellini et al. (2015).

4.2.5 Discussion

The results of the previous sections allow a comparison of the observations with predictions from the literature regarding the suggested CMB quenching mechanism that has been presented to explain the apparent rarity of high redshift ($z \gtrsim 4$) misaligned jetted AGN in radio surveys. In this context, four models have been elaborated, of which models B, C and D are omitted in favour of model A. All physical scenarios for GB 1508+5714 involve a FR-II-like source structure (oriented at a small angle to the line of sight) with varying lobe and hotspot contributions to the observed radio and X-ray data. While the core of the source is easily identifiable, the two components observed to the east and west of the core are considered to be extended lobes. The physical sizes of the hotspots may be smaller than the beam size in the observation, and it is unclear what fraction of the emission should be attributed to lobe emission

versus hotspots. They could be interpreted as two individual hotspots, as in the previous study presented in this paper in Sect. 4.1, but the situation was clearer in that case than for GB 1508+5714. The additional residual radio flux density measured by LOFAR is estimated from the difference between the total flux density and the flux densities of the resolved components. This may be due to artefacts introduced during calibration or to non-Gaussian extensions of the lobes or hotspots. Therefore, this diffuse contribution may not be real and is only considered for models B, C and D. The model in which the non-Gaussian extensions are rejected as not being real features is referred to as model A.

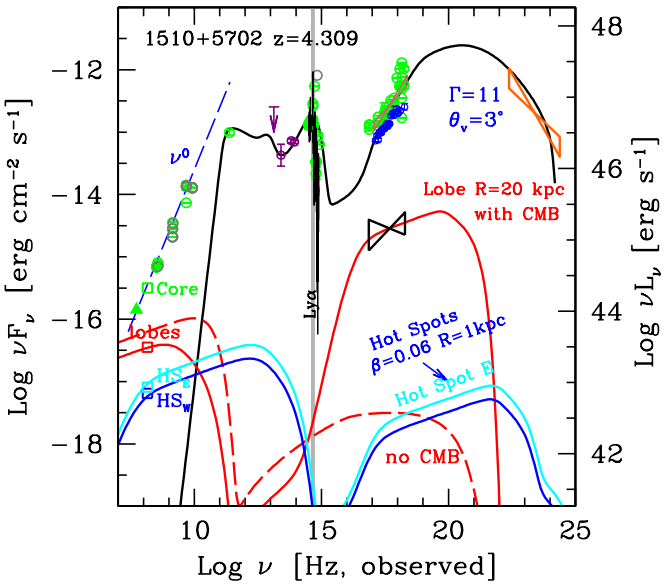

Figure 4.17: SED presented in Kappes et al. (2022) of 1510+5702, from radio to γ-rays. The model shown (see parameters in Table 4.2) describes the non-thermal jet emission, the accretion disk and the molecular torus contributions (upper black solid). All data are archived (https://tools.ssdc.asi.it/). For the hotspots and lobes (as labelled; see corresponding model parameters in Table 4.3) this figure corresponds to model A. The lobe with a radius of 20 kpc is responsible for the diffuse X-ray emission observed by Chandra (black butterfly spectrum). The dashed red line is the lobe emission if there were no CMB. The vertical gray line gives the position of the Lyα line. The dashed blue line is not a fit to the radio spectrum of the core, but has been drawn as a guide. The labelled data points at 144 MHz are the LOFAR determinations from this work.

Model A — The dominant lobes in GB 1508+5714 each contain an unresolved hotspot, with the maximum possible brightness limited to $\lesssim$ 4.3 mJy and $\lesssim$ 5.3 mJy respectively, to avoid exceeding the local surface brightness of their respective lobes. The

combined flux density of the lobes is 23.6 mJy, with the X-ray emission dominated by the two strong lobes, although the Chandra image indicates more efficient X-ray production associated with the western lobe. The SED for this model is shown in Fig. 4.17, with the calculated equipartition for the lobes ($E_e/E_B \sim 89$) and the power required to excite this structure is 5×10^{46} erg s^{-1}. The hotspots are also in a state of equipartition.

Although model A is preferred as a self-consistent and physically motivated representation of the observed properties of GB 1508+5714, it does not allow the tightest constraints on hotspot luminosities or hotspot advance velocities, which depend on differences in Doppler amplification. Therefore, for the sake of completeness, models B, C and D are also discussed below, but the constraints require higher quality interferometric images than the available data could provide. These models are not currently considered to have any scientific value. However, CMB quenching is present, as expected, to explain the observations.

The three models that were discarded during the scientific analysis of the data are presented in the following without any a priori assumptions about whether the hotspots or the lobes dominate the observed X-ray emission. The results for the individual models B, C and D are presented with parameters derived from the individual morphological interpretations and modelling of the accretion disc, jet, hotspots and lobes.

Model B — Assuming that the remaining 2.8 mJy radio flux density is produced by two lobes, each with a radius of 20 kpc, it is further assumed that these lobes produce the diffuse Chandra X-ray emission. The resolved components in the east and west are interpreted as hotspots. It follows from this assumption that this model excludes the possibility that the hotspots contribute to the diffuse X-ray flux. The corresponding SED and model are shown in Fig. 4.18. As discussed above (Equation (4.6)), the magnetic field strength must be less than the order of one ~microGauss, regardless of the size of the lobes. This very small value, together with the requirement to produce a large diffuse X-ray luminosity, leads to best-fit models that can only be far from equipartition. In this case $E_e/E_B \sim 630$. The effect of the CMB can be seen by examining the lobe in the SED in the absence of the CMB. The first effect is a huge reduction in the X-ray flux due to the absence of CMB seed photons. The radio spectrum is also drastically different, because the particle distribution would have a radiative cooling break at much higher energies. Therefore, the emission slope in the radio band would remain flat down to the sub-millimeter range.

The two hotspots have similar but not identical fluxes. Model B allows this to be explained by the different Doppler boost due to the bulk velocity of the hotspots, which are assumed to be the same in all respects except the viewing angle. They

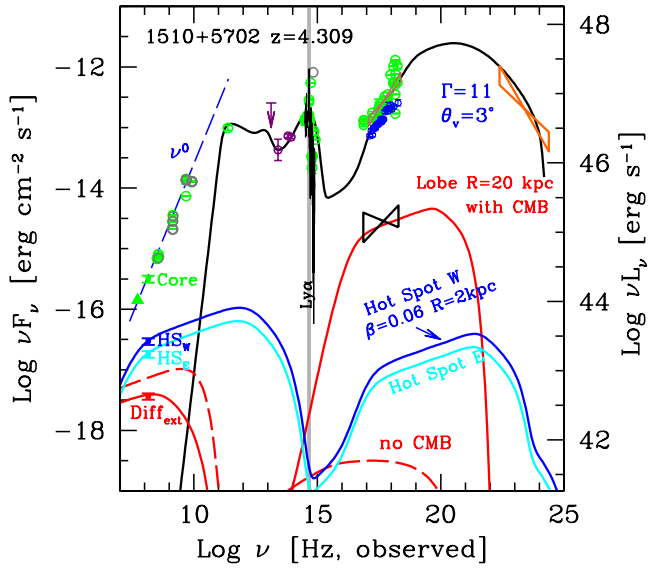

Figure 4.18: As Fig. 4.17, but for model B. The hotspots are 2 kpc in size and have a weaker magnetic field. All the parameters are given in Table 4.3, together with those assumed for the lobes. Credit: Kappes et al. (2022).

are therefore modelled as having a physical radius of 2 kpc. If the hotspots do not contribute significantly to the diffuse X-ray flux, no unique solution can be found. This strengthens the hypothesis made in model A that there should be an equipartition between the relativistic electron and the total magnetic field energy in the hotspot. This constraint, listed in Table 4.3, is also a strong enough constraint to fix the value of the power injected into each lobe, which is ~1/65 of the total jet power (the emitted synchrotron radiation in our respective radio band). For consistency with the viewing angle of the jet, a viewing angle of $\theta = 3°$ and $\theta = 180° - 3°$ is assumed for the western and eastern hotspots, respectively (Ghisellini et al. 2015).

Model C — Assuming that the lobes do not contribute to the observed radio emission, the diffuse X-ray flux is entirely produced by the eastern and western hotspots.

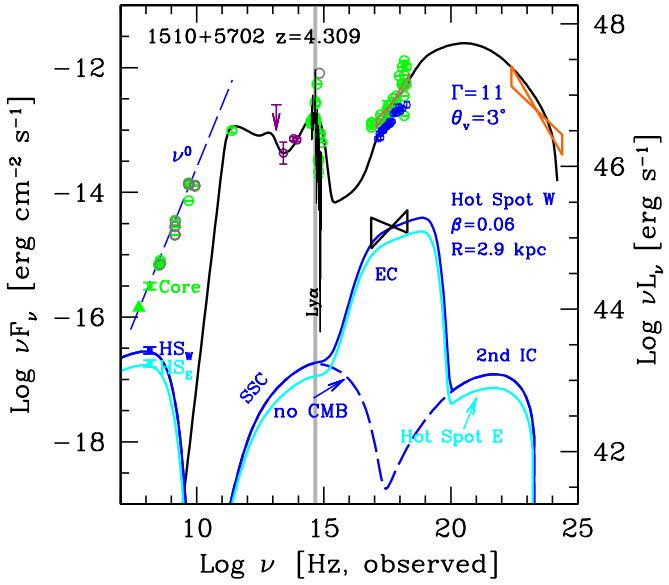

Figure 4.19: As Fig. 4.17, but for model C. The diffuse X-ray emission observed by Chandra is produced by the hotspots and there are no lobes. We also show what the flux from the western hotspot would look like if there were no CMB. This shows that most of the diffuse X-ray flux is the result of the external Compton process with the CMB photons, while the SSC component is very weak. At high energies the flux is dominated by the second order Compton scattering (second IC). The parameters assumed for the hotspots are given in Table 4.3. Credit: Kappes et al. (2022).

The remaining emission in the image is then unphysical. It is worth noting that the western hotspot is resolved in the Chandra image (Siemiginowska et al. 2003; Yuan et al. 2003), while there is no corresponding counterpart in the east. This discrepancy may be due to the mixing of the X-ray emission from the eastern hotspot with the dominant core emission. The SED for this model is shown in Fig. 4.19. The magnetic field strength of the hotspots is 7 μG. This means that the magnetic field is far from equipartition: $E_e/E_B \sim 4 \times 10^4$. The power that the jet has to deliver to the hotspot in the form of relativistic electrons is substantial, amounting to $P_e \sim 6 \times 10^{47}\,\mathrm{erg\,s^{-1}}$. This power is even larger than P_{jet}. The emission process is inefficient because even the most energetic electrons cannot cool radiatively on a timescale shorter than the adiabatic timescale $\sim R/c$. Consequently, a large number of relativistic electrons (and hence a large injected power) is required, leading to a scenario that is far from equipartition.

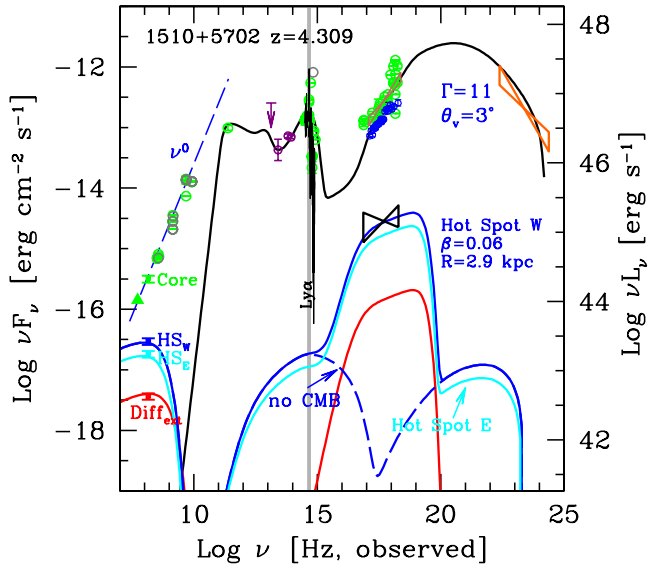

Figure 4.20: As Fig. 4.17, but for model D. The diffuse X-ray emission observed by Chandra is produced by the hotspots, but we assume that the lobes exist and emit 2.8 mJy flux density at 144 MHz. We then study the parameters that a 20 kpc lobe must have to produce the radio, but not the observed X-rays. The hotspots have the same parameters as in Fig. 4.19 and are given in Table 4.3, together with the parameters assumed for the lobes. Credit: Kappes et al. (2022).

Model D — The lobes are assumed to be responsible for the residual flux density of 2.8 mJy, while the extended radio emission is attributed to two strong hotspots. In contrast to model B, the lobes are not assumed to contribute significantly to the diffuse X-ray emission, which is assumed to be dominated by the hotspots. The SED for this model is shown in Fig. 4.20. This allows the model to be close to equipartition, but the problems associated with the hotspot properties of model B remain. In conclusion, model A is the only one that satisfies the equipartition condition for both the hotspots and the lobes close to them. It is also by far the least energetically demanding model. Model B only achieves equipartition within the hotspots, but not in the lobes, and models C and D do not achieve equipartition anywhere. Therefore, all three models B, C and D are rejected in favour of model A.

Hotspot Advance Speeds

Although models B, C and D have to be discarded because they do not satisfy the equipartition conditions, they have the very attractive ability (if applicable) to use their distinction between hotspot and lobe emission to estimate the advance speed of the hotspot components. To illustrate what might be possible if future observations provide data of sufficient quality to constrain these models without relying on equipartition conditions, the current results of such an analysis are described below. Using the simplified model of a symmetric two-sided jet, parameters such as the hotspot velocity and the jet inclination angle can be constrained using the ratio of the hotspot flux densities as introduced previously in Equation (1.10):

$$R = \frac{F_{\nu,\mathrm{W}}}{F_{\nu,\mathrm{E}}} = \left(\frac{1+\beta\cos(\theta)}{1-\beta\cos(\theta)}\right)^{3-\alpha} \quad . \tag{4.7}$$

Here $v = \beta c$ is the speed of two symmetric blobs, where θ is the viewing angle of the approaching blob. From the flux density of the hotspot components in models B, C and D, the value of R is $1.65^{+0.03}_{-0.05}$. For illustrative purposes, a wide inclination angle between $0° \leq \theta \leq 25°$ is first considered, and three representative cases for hotspot velocities, β_{HS}= 0.053, 0.060 and 0.067, color-coded in Fig. 4.21, are taken into account. The spectral index in the range obtained from Fig. 4.16 is encoded in the opacity of each color, where a more saturated tone indicates a steeper α ($\alpha_{min} = -1.4$; $\alpha_{max} = -0.84$). A lower limit of $\theta_{\mathrm{min}} \gtrsim 2°$ is obtained by comparing the measured projected size of the source with the largest known radio galaxies (~ 1 Mpc; Jeyakumar & Saikia 2000), assuming that these represent an upper limit on the physical size a radio galaxy can have. The SED of the core then suggests that the inclination angle of the inner jet is about $\theta_{\mathrm{SED}} \approx 3°$. While the inclination angle may vary further along the jet due to various effects (e.g. jet bending or precession), it is observed that the estimates of the hotspot velocities within this model are only weakly dependent on the orientation angle, and thus cannot vary much from about 0.06 c.

Jet Age

The evolutionary stage of a jet, which determines its age, is an important characteristic that can be estimated from its size. Assuming that the estimates of the hotspot advance speed derived from SED modelling are accurate and that this speed is constant in time, the age of the jet can be estimated from its size. Despite the failures of the models B, C and D it is noted that the estimates of the hotspot advance speed should be correct to within an order of magnitude (Scheuer 1995). The results of the following derivation

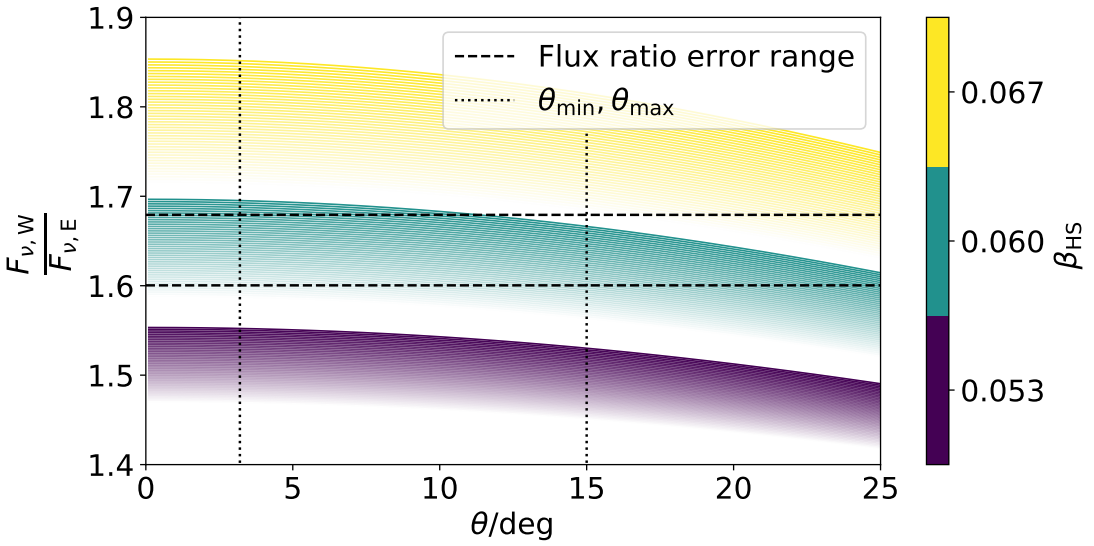

Figure 4.21: Ratio of the flux of the western to the eastern component, R, as a function of the inclination angle, θ, and the hotspot velocity, β_{HS}. The different hotspot velocities are color coded; the spectral index is given by the opacity of the different regions (a more saturated tone is a steeper $-0.84 > \alpha > -1.4$). The dashed horizontal lines constrain the parameter space with R within its error (see Equation (4.7)).The $\theta_{\rm min}$ value is determined by comparing the measured projected size with large radio galaxies. The $\theta_{\rm SED}$ value shows the tilt angle of the inner jet suggested by the SED. Credit: Kappes et al. (2022).

are linearly dependent on the velocity and are therefore also expected to be within an order of magnitude. According to numerical simulations (Perucho et al. 2019) of jet evolution in hot galactic atmospheres, jets can accelerate down the pressure gradient of the galactic halo, and they also undergo deceleration as the dentist's drill effect develops (Scheuer 1974), implying that the constant velocity assumption is not entirely valid. However, it can still provide a good first order estimate. In this case the age of the jet can be given by

$$t_{\rm jet} \simeq 7.3 \times 10^6 \left(\frac{L_{\rm jet}}{135\,{\rm kpc}}\right)\left(\frac{0.06}{\beta_{\rm HS}}\right) {\rm yr}, \tag{4.8}$$

where $L_{\rm jet}$ is the jet length.

The lobe pressure can be estimated from the power and age of the jet, as well as the volume of the lobe, using the following expression derived from dimensional arguments (see Begelman & Cioffi 1989; Perucho et al. 2017), given that powerful relativistic jets inject a significant fraction of their energy into the lobe pressure (see Perucho et al. 2017),

$$p_{\rm lobe} = \kappa \frac{P_{\rm jet}\, t_{\rm jet}}{V_{\rm lobe}}, \tag{4.9}$$

with $\kappa \simeq 0.4$ for relativistic jets (see Perucho et al. 2017). Assuming a lobe radius of 20, kpc and approximating the lobe volume as that of a cylinder of length L, we can

estimate the lobe pressure using the expression above and taking $P_{\rm jet} \simeq 10^{47}$, erg/s and the age of the jet derived from the previous equation. Approximating the lobe volume to that of a cylinder of length L and an estimated lobe radius of 20 kpc, taking $P_{\rm jet} \simeq 10^{47}$ erg/s, and using the previous expression for the age of the jet, we obtain for the lobe pressure

$$p_{\rm lobe} \simeq 1.8 \times 10^{-9} \left(\frac{\kappa}{0.4}\right) \left(\frac{P_{\rm jet}}{10^{47}\,{\rm erg/s}}\right) \left(\frac{\beta_{\rm HS}}{0.06}\right)^{-1} \left(\frac{R_{\rm lobe}}{20\,{\rm kpc}}\right)^{-2} {\rm erg/cm^3}. \tag{4.10}$$

The expression for the lobe pressure is independent of jet length, since the contributions from jet age and lobe volume are cancelled out. The estimated lobe pressure is much higher, by two orders of magnitude, than the magnetic pressure estimated from the modelled magnetic field strengths ($\simeq 2 \times 10^{-12}$ erg/cm^3). This discrepancy may be due to the inclusion of the thermal population in the lobe pressure estimate in this study, which can dominate both electron and magnetic pressures (Croston et al. 2005). However, Hardcastle (2015) provides evidence that the magnetic field in hotspots and lobes of different FR-II sources should be around equipartition with the emitting electrons, which contradicts the above result. Assuming that the jet power cannot be significantly less than $P_{\rm jet} \simeq 10^{47}\,{\rm erg, s^{-1}}$, and that the kinematic estimate of the jet age is within an order of magnitude, it appears that both approaches can only be reconciled if either $\kappa \ll 1$ or the total lobe pressure is significantly greater than the magnetic field pressure (i.e. if the lobes are dominated by the thermal population). Perucho et al. (2017) suggest that it is unlikely that $\kappa \ll 1$, even for non-relativistic jets. However, it is possible that the thermal population dominates the lobes. Further high quality data are needed to test this hypothesis.

4.2.6 Conclusion

New high-resolution images of the high-redshift blazar GB 1508+5714 observed with the ILT reveal a previously unseen component in the eastern direction. By reconvolving the ILT data with the VLA beam, a spectral index map has been produced that provides constraints on the spectral indices of individual components: $-1.2^{+0.4}_{-0.2}$ for the western component, steeper than -1.1 for the eastern region, and 0.023 ± 0.007 for the core.

A model was considered where the hotspots in the detected components are unresolved and mixed by the lobe emission, with the X-ray emission originating from the lobes and partially mixed by the bright core region. The results of the preferred model are consistent with hotspots in a state of equipartition and lobes almost so. The CMB quenching processes proposed by Ghisellini et al. (2015) were necessary in all models.

Table 4.2: Adopted parameters for the jet model shown in Figs. 4.17–4.20.

Comp	z	M	$L_{\rm d}$	$R_{\rm diss}$	$R_{\rm BLR}$	$P'_{\rm e,jet,45}$	B	Γ	$\theta_{\rm V}$	$P_{\rm jet,45}$
[1]	[2]	[3]	[4]	[5]	[6]	[7]	[8]	[9]	[10]	[11]
jet	4.309	1.5e9	32	630	560	0.03	1.9	11	3	360

Col. [1]: Component; Col. [2]: redshift; Col. [3]: black hole mass in units of solar masses; Col. [4]: disc luminosity in units of 10^{45} erg s^{-1}; Col. [5]: distance of the dissipation region from the black hole in units of 10^{15} cm; Col. [6]: size of the broad line region in units of 10^{15} cm; Col. [7]: power injected in the jet in relativistic electrons, calculated in the comoving frame, in units of 10^{45} erg s^{-1}; Col. [8]: magnetic field in G; Col. [9]: bulk Lorentz factor; Col. [10]: viewing angle in degrees; Col. [11]: total kinetic plus magnetic jet power in units of 10^{45} erg s^{-1}. The power and energy values refer to a single jet. We assume that $Q(\gamma)$ relativistic electrons with a broken power law distribution are injected throughout the source, i.e. $Q(\gamma) \propto \gamma^{-1.5}$ below $\gamma = 200$ and $Q(\gamma) \propto \gamma^{-3}$ between $\gamma = 200$ and $\gamma = 4000$.

Table 4.3: Adopted parameters for the hotspot and lobe models shown in Figs. 4.17–4.20.

Model	Comp.	R	$\theta_{\rm v}$	β	$P_{\rm e,45}$	B	$\gamma_{\rm b}$	$\gamma_{\rm max}$	$\log E_{\rm e}$	$\log E_{\rm B}$	$E_{\rm e}/E_{\rm B}$
[1]	[2]	[3]	[4]	[5]	[6]	[7]	[8]	[9]	[10]	[11]	[12]
A	HS	1	3°, −177°	0.06	2.3	180	600	1e6	56.2	56.2	0.9
A	lobe	20	–	0	50	7	300	1e5	59.2	57.3	89
B	HS	2	3°, −177°	0.06	5.4	140	600	1e6	56.9	56.9	1
B	lobe	20	–	0	50	2.4	300	1.e5	59.2	56.4	630
C	HS	2.9	3°, −177°	0.06	600	7	400	1.e4	59.4	54.8	4e4
D	HS	2.9	3°, −177°	0.06	600	7	400	1.e4	59.4	54.8	4e4
D	lobe	20	–	0	1	12	400	1e4	57.8	57.7	1.2

Col. [1]: Type of model Col. [2]: component (HS = hotspot); Col. [3]: size in kpc; Col. [4]: viewing angle; Col. [5]: bulk velocity; Col. [6]: Power injected in relativistic electrons in units of 10^{45} erg s^{-1}; Col. [7]: magnetic field in μG; Col. [8] and Col. [9]: break and maximum Lorenz factor of the injected electron distribution; Col. [10]: logarithm of the total energy in relativistic electrons, in erg; Col. [11]: logarithm of the total energy in magnetic field, in erg. Col. [12]: Total energy in relativistic electrons over total energy in magnetic field. The values of powers and energetics refer to *each* hotspot and lobe. The lobe flux shown in the figures corresponds to *two* lobes. We assume to inject relativistic electrons $Q(\gamma)$ with a broken power law distribution throughout the source, i.e. $Q(\gamma) \propto \gamma$ below $\gamma = \gamma_{\rm b}$ and $Q(\gamma) \propto \gamma^{-2.7}$ between $\gamma_{\rm b}$ and $\gamma_{\rm max}$.

While the current ILT configuration has more international stations, resulting in an overall more sensitive and stable instrument, higher quality data are still needed for a full investigation and characterisation of the models discussed. However, this study shows that high-z blazars can be studied with the 2015 ILT configuration, and any observations made afterwards can only provide better observational constraints. Expanding the sample of high-z blazars resolved at multiple frequencies will allow a statistical study of the population.

5 Final Remarks and Outlook

This work reflects on the current understanding of the properties of high redshift blazars and their environments, the challenges of modern sub-GHz interferometry, and handling the resulting data and computational challenges. Nevertheless, this paper presents a complete analysis of two high redshift blazars, relying mainly on ILT data, but also using multi-frequency information to provide insights into the full picture. It also shows that high resolution ILT data can add crucial information to studies that rely on multi-frequency information.

Several issues still need to be dealt with, in particular present shortcomings in the LOFAR-VLBI pipeline. While reducing the data and imaging a single observation for a single target works in most cases, some sources require extra work, usually if they are not very bright, or on the contrary are extremely bright, or have a very complex structure that has not yet been resolved. This can lead to additional months of work, which is not feasible for large sample studies or even sky surveys. So it is clear that the ultimate goal is to eventually provide a pipeline that is computationally capable of reducing and imaging a full sky survey in reasonable time and quality at the highest ILT resolution. This also poses challenges in terms of infrastructure, provision of sufficient computational resources, and archiving capabilities. For example, observing the entire northern sky with the ILT with 8 hours of integration time for each pointing and a standard averaging of 1 s in time and a frequency resolution of 16 channels per 195.3 kHz sub-band results in raw archival data in the order of 200 petabytes (each pointing is about 15 TB).

Another major improvement will be the ability to process LBA data in the same way, pushing accessibility for any researcher down to the 50 MHz regime. The general capability has been demonstrated in a few individual works (e.g. Groeneveld et al. 2022; Morabito et al. 2016). However, the pipeline has not yet been extensively tested with such data. The current focus is on the HBA data, mainly to produce accurate sky models at the highest resolution available. These models can then be used to calibrate the LBA data. Without these models the whole process is excessively labour intensive.

To address the scientific questions raised in this work, the next step is to repeat the analysis shown on a larger sample, preferably with a wide range of redshifts. This will

allow us to infer sample-based properties of blazars, in particular their inner workings, their environments and how they interact with it, and their evolution. While such studies were possible before access to ILT data, it provides important information about the spectral behaviour of the synchrotron bump in the SED. In addition, the ability to assign the detected radio flux to their morphological origin in the target, as shown in this paper, is a significant aid to model tuning. For the foreseeable future, the ILT will be the only telescope operating at these frequencies with subarcsecond resolution capabilities covering the northern sky. Finally, any results obtained with the ILT will ultimately be an important contribution to the SKA–Low in Australia, which is planned to be operational by 2029. Together, the ILT and SKA will provide a unique window for modern astronomy with the highest resolutions at the lowest frequencies across the full sky.

Bibliography

Acciari, V. A., Ansoldi, S., Antonelli, L. A., et al. 2021, MNRAS, 504, 1427

Anderson, K., Alexov, A., Bähren, L., et al. 2011, in Astronomical Society of the Pacific Conference Series, Vol. 442, Astronomical Data Analysis Software and Systems XX, ed. I. N. Evans, A. Accomazzi, D. J. Mink, & A. H. Rots, 53

Antonucci, R. 1993, Annual review of astronomy and astrophysics, 31, 473

ASTRON. 2017, COBALT: correlator and beamforming application platform for the lofar telescope

Atwood, W. B., Abdo, A. A., Ackermann, M., et al. 2009, The Astrophysical Journal, 697, 1071–1102

Badole, S., Venkattu, D., Jackson, N., et al. 2022, A&A, 658, A7

Bass, M., Van Stryland, E. W., Williams, D. R., & Wolfe, W. L. 2001, Handbook of optics, Vol. 2 (McGraw-Hill New York)

Becker, R. H., White, R. L., & Helfand, D. J. 1995, ApJ, 450, 559

Begelman, M. C. & Cioffi, D. F. 1989, ApJ, 345, L21

Begeman, K., Belikov, A., Boxhoorn, D., et al. 2011, Future Generation Computer Systems, 27, 319

Bhatnagar, S. & Cornwell, T. J. 2004, A&A, 426, 747

Blandford, R., Meier, D., & Readhead, A. 2019, Annual Review of Astronomy and Astrophysics, 57, 467

Blandford, R. D. & Königl, A. 1979, ApJ, 232, 34

Blandford, R. D. & Payne, D. G. 1982, 199, 883

Blandford, R. D. & Znajek, R. L. 1977, 179, 433

Blundell, K. M., Rawlings, S., & Willott, C. J. 1999, The Astronomical Journal, 117, 677

Bonnassieux, E., Edge, A., Morabito, L., & Bonafede, A. 2020, Astronomy and Astrophysics, 637, A51

Bonnassieux, E., Sweijen, F., Brienza, M., et al. 2022, A&A, 658, A10

Bridle, A. H. & Schwab, F. R. 1999, in Astronomical Society of the Pacific Conference Series, Vol. 180, Synthesis Imaging in Radio Astronomy II, ed. G. B. Taylor, C. L. Carilli, & R. A. Perley, 371

Broekema, P. C., Mol, J. J. D., Nijboer, R., et al. 2018, Astronomy and Computing, 23, 180

Burd, P. R., Mannheim, K., März, T., et al. 2018, Astronomische Nachrichten, 339, 358

Celotti, A. & Fabian, A. C. 2004, Monthly Notices of the Royal Astronomical Society, 353, 523

Cheung, C., Wardle, J., & Lee, N. 2005, 22nd Texas Symp. on Relativistic Astrophysics ed P. Chen et al (Palo Alto, CA: SLAC) 480

Cheung, C. C. 2004, ApJ, 600, L23

Cohen, A. S., Lane, W. M., Cotton, W. D., et al. 2007a, AJ, 134, 1245

Cohen, M. H., Lister, M. L., Homan, D. C., et al. 2007b, ApJ, 658, 232

Collaboration, A., Adrián-Martínez, S., Albert, A., et al. 2015, A&A, 576, L8

Collaboration, M., Acciari, V. A., Ansoldi, S., et al. 2020, A&A, 637, A86

Condon, J. J. 1988, Radio Sources and Cosmology (New York, NY: Springer New York), 641–678

Condon, J. J., Cotton, W. D., Greisen, E. W., et al. 1998, AJ, 115, 1693

Cooper, N. J., Lister, M. L., & Kochanczyk, M. D. 2007, The Astrophysical Journal Supplement Series, 171, 376

Cornwell, T. & Fomalont, E. B. 1999, in Synthesis imaging in radio astronomy II, Vol. 180, 187

Cornwell, T. J. & Evans, K. F. 1985, A&A, 143, 77

Cornwell, T. J., Golap, K., & Bhatnagar, S. 2008, IEEE Journal of Selected Topics in Signal Processing, 2, 647

Cornwell, T. J. & Wilkinson, P. N. 1981, MNRAS, 196, 1067

Croston, J. H., Hardcastle, M. J., Harris, D. E., et al. 2005, The Astrophysical Journal, 626, 733

Daly, R. A., Sprinkle, T. B., O'Dea, C. P., Kharb, P., & Baum, S. A. 2012, MNRAS, 423, 2498

de Gasperin, F., Dijkema, T. J., Drabent, A., et al. 2019, A&A, 622, A5

de Gasperin, F., Mevius, M., Rafferty, D. A., Intema, H. T., & Fallows, R. A. 2018, Astronomy and Astrophysics, 615, A179

de Gasperin, F., Williams, W. L., Best, P., et al. 2021, A&A, 648, A104

de Vries, W. H., Becker, R. H., & White, R. L. 2006, AJ, 131, 666

Dunlop, J. S. & Peacock, J. A. 1990, MNRAS, 247, 19

Fanaroff, B. & Riley, J. 1974, Monthly Notices of the Royal Astronomical Society, 167, 31P

Georgakakis, A., Aird, J., Schulze, A., et al. 2017, Monthly Notices of the Royal Astronomical Society, 471, 1976

Ghisellini, G., Celotti, A., Tavecchio, F., Haardt, F., & Sbarrato, T. 2014, Monthly Notices of the Royal Astronomical Society, 438, 2694

Ghisellini, G., Haardt, F., Ciardi, B., et al. 2015, MNRAS, 452, 3457

Ghisellini, G. & Tavecchio, F. 2009, MNRAS, 397, 985

Ghisellini, G. & Tavecchio, F. 2015, Monthly Notices of the Royal Astronomical Society, 448, 1060

Greisen, E. W. 2003, in Astrophysics and Space Science Library, Vol. 285, Information Handling in Astronomy - Historical Vistas, ed. A. Heck, 109

Grobler, T. L., Nunhokee, C. D., Smirnov, O. M., van Zyl, A. J., & de Bruyn, A. G. 2014, MNRAS, 439, 4030

Groeneveld, C., van Weeren, R. J., Miley, G. K., et al. 2022, A&A, 658, A9

Group, T. H. 2000-2010, Hierarchical data format version 5, http://www.hdfgroup.org/HDF5, visited 01. April 2022

Hamaker, J. P. & Bregman, J. D. 1996, A&AS, 117, 161

Hardcastle, M. 2015, Kiloparsec-Scale AGN Jets, Vol. 414 (Springer), 83

Hardcastle, M. J. & Worrall, D. M. 2000, MNRAS, 319, 562

Harris, D. E., Moldón, J., Oonk, J. R. R., et al. 2019, The Astrophysical Journal, 873, 21

Harwood, J. J., Hardcastle, M. J., & Croston, J. H. 2015, MNRAS, 454, 3403

Harwood, J. J., Mooney, S., Morabito, L. K., et al. 2022, A&A, 658, A8

Hewitt, E. & Hewitt, R. E. 1979, Archive for history of Exact Sciences, 129

Hodges-Kluck, E., Gallo, E., Ghisellini, G., et al. 2021, MNRAS, 505, 1543

Högbom, J. A. 1974, A&AS, 15, 417

Hook, I. M., McMahon, R. G., Patnaik, A. R., et al. 1995, Monthly Notices of the Royal Astronomical Society, 273, L63

Hummel, C., Muxlow, T., Krichbaum, T., et al. 1992, Astronomy and Astrophysics, 266, 93

Intema, H., Jagannathan, P., Mooley, K., & Frail, D. 2016, Astronomy & Astrophysics

Intema, H. T., Jagannathan, P., Mooley, K. P., & Frail, D. A. 2017, A&A, 598, A78

Intema, H. T., van der Tol, S., Cotton, W. D., et al. 2009, A&A, 501, 1185

Ishwara-Chandra, C. H. & Saikia, D. J. 2000, Monthly Notices of the Royal Astronomical Society, 317, 658

Jackson, J. D. 1975, Electrodynamics (Wiley Online Library)

Jackson, N., Badole, S., Morgan, J., et al. 2022, A&A, 658, A2

Jackson, N., Tagore, A., Deller, A., et al. 2016, Astronomy & astrophysics, 595, A86

Jaeger, S. 2008, in Astronomical Data Analysis Software and Systems XVII, Vol. 394, 623

Jeyakumar, S. & Saikia, D. 2000, Monthly Notices of the Royal Astronomical Society, 311, 397

Junklewitz, H., Bell, M. R., & Enßlin, T. 2015, A&A, 581, A59

Kadler, M., Krauß, F., Mannheim, K., et al. 2016, Nat Phys, advance online publication, article

Kappes, A. 2017, Master's thesis, Julius-Maximilians-Universität Würzburg, Germany

Kappes, A., Burd, P. R., Kadler, M., et al. 2022, A&A, 663, A44

Kappes, A., Perucho, M., Kadler, M., et al. 2019, Astronomy & Astrophysics, 631, A49

Kawakatu, N. & Kino, M. 2006, Monthly Notices of the Royal Astronomical Society, 370, 1513

Kellermann, K. I. & Pauliny-Toth, I. I. K. 1969, ApJ, 155, L71

Kharb, P., Lister, M., & Cooper, N. 2010, The Astrophysical Journal, 710, 764

Kharb, P., O'Dea, C. P., Baum, S. A., et al. 2008, ApJS, 174, 74

Komissarov, S. 2012, Central Engines: Acceleration, Collimation and Confinement of Jets (John Wiley and Sons), 81–114

Kramarenko, I. G., Pushkarev, A. B., Kovalev, Y. Y., et al. 2021, arXiv e-prints, arXiv:2106.08416

Krauß, F., Kadler, M., Mannheim, K., et al. 2014, A&A, 566, L7

Krolik, J. 1999, Nature, 398, 678

Kukreti, P., Morganti, R., Shimwell, T. W., et al. 2022, A&A, 658, A6

Landau, L. D. & Lifshitz, E. M. 1987, Fluid Mechanics, Second Edition: Volume 6 (Course of Theoretical Physics), 2nd edn., Course of theoretical physics / by L. D. Landau and E. M. Lifshitz, Vol. 6 (Butterworth-Heinemann)

Lara, L., Cotton, W. D., Feretti, L., et al. 1997, ApJ, 474, 179

Leahy, J. & Williams, A. 1984, Monthly Notices of the Royal Astronomical Society, 210, 929

Liu, H. T. & Bai, J. M. 2006, The Astrophysical Journal, 653, 1089

McKeough, K., Siemiginowska, A., Cheung, C. C., et al. 2016, The Astrophysical Journal, 833, 123

McMullin, J. P., Waters, B., Schiebel, D., Young, W., & Golap, K. 2007, in Astronomical Society of the Pacific Conference Series, Vol. 376, Astronomical Data Analysis Software and Systems XVI, ed. R. A. Shaw, F. Hill, & D. J. Bell, 127

Meisenheimer, K., Roser, H.-J., Hiltner, P., et al. 1989, Astronomy and Astrophysics, 219, 63

Meisenheimer, K., Yates, M. G., & Roeser, H. J. 1997, A&A, 325, 57

Mevius, M. 2018, RMextract: Ionospheric Faraday Rotation calculator

Meyer, M., Scargle, J. D., & Blandford, R. D. 2019, ApJ, 877, 39

Mingo, B., Croston, J. H., Hardcastle, M. J., et al. 2019, Monthly Notices of the Royal Astronomical Society, 488, 2701–2721

Moldón, J., Deller, A. T., Wucknitz, O., et al. 2015, A&A, 574, A73

Morabito, L. K., Deller, A. T., Röttgering, H., et al. 2016, Monthly Notices of the Royal Astronomical Society, 461, 2676

Morabito, L. K. & Harwood, J. J. 2018, Monthly Notices of the Royal Astronomical Society, 480, 2726–2732

Morabito, L. K., Jackson, N. J., Mooney, S., et al. 2021, Astronomy & astrophysics.

Morabito, L. K., Jackson, N. J., Mooney, S., et al. 2022, A&A, 658, A1

Moran, J. M. & Dhawan, V. 1995, in Astronomical Society of the Pacific Conference Series, Vol. 82, Very Long Baseline Interferometry and the VLBA, ed. J. A. Zensus, P. J. Diamond, & P. J. Napier, 161

Muse. 2006, Supermassive Black Hole, Black Holes and Revelations, Warner Bros., Helium-3

Nemmen, R. S., Georganopoulos, M., Guiriec, S., et al. 2012, Science, 338, 1445

O'Dea, C. P., Barvainis, R., & Challis, P. M. 1988, The Astronomical Journal, 96, 435

O'Dea, C. P., Daly, R. A., Kharb, P., Freeman, K. A., & Baum, S. A. 2009, A&A, 494, 471

Offringa, A. R. 2010, AOFlagger: RFI Software, Astrophysics Source Code Library, record ascl:1010.017

Offringa, A. R. 2016, A&A, 595, A99

Offringa, A. R., McKinley, B., Hurley-Walker, et al. 2014, MNRAS, 444, 606

Offringa, A. R. & Smirnov, O. 2017, MNRAS, 471, 301

Osterbrock, D. E. & Ferland, G. J. 2006, Astrophysics of gaseous nebulae and active galactic nuclei (University science books)

Owen, F. N. & Ledlow, M. J. 1994, in Astronomical Society of the Pacific Conference Series, Vol. 54, The Physics of Active Galaxies, ed. G. V. Bicknell, M. A. Dopita, & P. J. Quinn, 319

Pandey-Pommier, M., Intema, H., & Heald, G. 2016, in SF2A-2016: Proceedings of the Annual meeting of the French Society of Astronomy and Astrophysics, ed. C. Reylé, J. Richard, L. Cambrésy, M. Deleuil, E. Pécontal, L. Tresse, & I. Vauglin, 379–383

Perley, R. A., Dreher, J. W., & Cowan, J. J. 1984, ApJ, 285, L35

Perucho, M., Kovalev, Y. Y., Lobanov, A. P., Hardee, P. E., & Agudo, I. 2012a, The Astrophysical Journal, 749, 55

Perucho, M. & Martí, J. M. 2003, PASA, 20, 94

Perucho, M., Martí, J.-M., & Quilis, V. 2019, MNRAS, 482, 3718

Perucho, M., Martí, J.-M., Quilis, V., & Borja-Lloret, M. 2017, MNRAS, 471, L120

Perucho, M., Marti-Vidal, I., Lobanov, A. P., & Hardee, P. E. 2012b, Astronomy & Astrophysics, 545, A65

Peterson, B. M. 1997, An Introduction to Active Galactic Nuclei (Cambridge, New York Cambridge University Press)

Peterson, B. M., Ferrarese, L., Gilbert, K., et al. 2004, The Astrophysical Journal, 613, 682

Pushkarev, A., Kovalev, Y., Lister, M., & Savolainen, T. 2009, Astronomy & Astrophysics, 507, L33

Pyrzas, S., Steenbrugge, K., & Blundell, K. 2015, Astronomy & Astrophysics, 574, A30

Ramírez-Olivencia, N., Varenius, E., Pérez-Torres, M., et al. 2022, A&A, 658, A4

Ramírez-Olivencia, N., Varenius, E., Pérez-Torres, M., et al. 2018, A&A, 610, L18

Readhead, A. C. S. & Wilkinson, P. N. 1978, ApJ, 223, 25

Ryle, M. & Vonberg, D. 1946, in Classics in Radio Astronomy (Springer), 184–187

Scheuer, P. 1995, Monthly Notices of the Royal Astronomical Society, 277, 331

Scheuer, P. A. G. 1974, Monthly Notices of the Royal Astronomical Society, 166, 513

Schneider, P. 2008, Einführung in die extragalaktische Astronomie und Kosmologie (Springer Berlin)

Schoenmakers, A. P., Mack, K. H., de Bruyn, A. G., et al. 2000, A&AS, 146, 293

Shakura, N. I. & Sunyaev, R. A. 1973, A&A, 24, 337

Shankar, F., Weinberg, D. H., & Miralda-Escudé, J. 2008, The Astrophysical Journal, 690, 20

Shepherd, M. C. 1997, in Astronomical Society of the Pacific Conference Series, Vol. 125, Astronomical Data Analysis Software and Systems VI, ed. G. Hunt & H. Payne, 77

Shimwell, T. W., Röttgering, H. J. A., Best, P. N., et al. 2017, Astronomy and Astrophysics, 598, A104

Shimwell, T. W., Tasse, C., Hardcastle, M. J., et al. 2019, Astronomy and Astrophysics, 622, A1

Shukla, A. & Mannheim, K. 2020, Nature Communications, 11, 4176

Siemiginowska, A., Smith, R. K., Aldcroft, T. L., et al. 2003, The Astrophysical Journal, 598, L15

Smirnov, O. M. 2011, A&A, 527, A106

Smirnov, O. M. & Tasse, C. 2015, \mnras, 449, 2668

Swarup, G., Sinha, R. P., & Hilldrup, K. 1984, MNRAS, 208, 813

Sweijen, F., Morabito, L. K., Harwood, J., et al. 2022, A&A, 658, A3

Tasse, C. 2014, arXiv e-prints, 1410, arXiv:1410.8706

Tasse, C., Hugo, B., Mirmont, M., et al. 2018, A&A, 611, A87

Tasse, C., Shimwell, T., Hardcastle, M. J., et al. 2021, A&A, 648, A1

Thomasson, P. 1986, Quarterly Journal of the Royal Astronomical Society, 27, 413

Thompson, A. R., Clark, B., Wade, C., & Napier, P. J. 1980, The Astrophysical Journal Supplement Series, 44, 151

Thompson, A. R., Moran, J. M., & Swenson, Jr., G. W. 2001, Interferometry and Synthesis in Radio Astronomy, 2nd Edition (New York : Wiley)

Timmerman, R., van Weeren, R. J., Callingham, J. R., et al. 2022, A&A, 658, A5

Urry, C. M. & Padovani, P. 1995, Publications of the Astronomical Society of the Pacific, 107, 803

Van Der Tol, S., Jeffs, B. D., & van der Veen, A.-J. 2007, IEEE Transactions on Signal Processing, 55, 4497

van Diepen, G., Dijkema, T. J., & Offringa, A. 2018, DPPP: Default Pre-Processing Pipeline

van Haarlem, M. P., Wise, M. W., Gunst, A. W., et al. 2013, A&A, 556, A2

van Weeren, R. J., Williams, W. L., Hardcastle, M. J., et al. 2016, ApJS, 223, 2

Varenius, E., Conway, J. E., Martí-Vidal, I., et al. 2016, A&A, 593, A86

Varenius, E., Conway, J. E., Martí-Vidal, I., et al. 2015, A&A, 574, A114

Vega-García, L. 2018, PhD thesis, University of Cologne

Vega-García, L., Perucho, M., & Lobanov, A. P. 2019, A&A, 627, A79

Vestergaard, M. & Peterson, B. M. 2006, The Astrophysical Journal, 641, 689

Volonteri, M., Haardt, F., Ghisellini, G., & Ceca, R. D. 2011, Monthly Notices of the Royal Astronomical Society, 416, 216

Wang, F., Yang, J., Fan, X., et al. 2021, The Astrophysical Journal, 907, L1

Wayth, R. B., Lenc, E., Bell, M. E., et al. 2015, PASA, 32, e025

Weedman, D. W. 1977, Annual Review of Astronomy and Astrophysics, 15, 69

Wilson, A. S., Young, A. J., & Shopbell, P. L. 2000, ApJ, 544, L27

Wu, J., Ghisellini, G., Hodges-Kluck, E., et al. 2017, MNRAS, 468, 109

Yuan, W., Fabian, A. C., Celotti, A., & Jonker, P. G. 2003, Monthly Notices of the Royal Astronomical Society, 346, L7

Zensus, J. A. 1997, Annual Review of Astronomy and Astrophysics, 35, 607

6 Appendix

6.1 Refereed Publications

Kappes et al. (2022): **Subarcsecond view on the high-redshift blazar GB 1508+5714 by the International LOFAR Telescope**
This paper presents ILT results on the high redshift blazar GB 1508+5714. By demonstrating the capabilities of the LOFAR-VLBI pipeline presented in Morabito et al. (2021), and by providing a multi-frequency analysis of the blazar, this work provides a blueprint for further such studies, enabling sample studies. Using high resolution X-ray information from Chandra and VLA data at 1.4 GHz, four SED models have been developed, one of which has been identified as the preferred model by equipartition considerations. As the main author of this paper, in addition to leading the collaboration and writing, I contributed to all the dos. The reduction of the ILT data was the main work done by me.

Bonnassieux et al. (2022): **Spectral analysis of spatially resolved 3C295 (subarcsecond resolution) with the International LOFAR Telescope:**
In this paper we use the ILT to study the spectral properties of 3C 295 at a low frequency of 132 MHz, where we find evidence for low-frequency flattening in the hotspot spectral properties and consistent spectral aging in the lobes. We fit low-frequency absorption models to the hotspots, with both free-free and synchrotron self-absorption models providing a better fit than a standard power law. The challenging dataset was calibrated and processed using the LOFAR-VLBI pipeline presented in Morabito et al. (2021). I provided checks and bug fixes within the pipeline, helping to enable the results obtained in the paper, besides actively developing parts of the pipeline.

Groeneveld et al. (2022): **Pushing sub-arcsecond resolution imaging down to 30 MHz with the trans-European International LOFAR Telescope**
In this paper we have carried out a pilot project to investigate the potential of the ILT to produce subarcsecond resolution images at very low radio frequencies (below 50 MHz). Our study successfully produced subarcsecond resolution images for six

bright radio sources (3C 196, 3C 225, 3C 273, 3C 295, 3C 298, and 3C 380) at frequencies down to 30 MHz, an improvement of more than an order of magnitude over pre-ILT observations. We have investigated the spatially resolved radio spectral properties of two sources (3C 196 and 3C 273) by comparing the data with observations at higher frequencies. This work demonstrates that subarcsecond imaging is possible with the ILT using the LOFAR-VLBI pipeline (presented in Morabito et al. 2021) at frequencies down to 30 MHz. My contribution to this project was mainly to support the error handling within the pipeline and to develop parts of the pipeline.

Morabito et al. (2022): **Sub-arcsecond imaging with the International LOFAR Telescope. I. Foundational calibration strategy and pipeline**
In this paper we present a calibration strategy for achieving sub-arcsecond resolution with the ILT at frequencies below 200 MHz. We discuss the challenges of high resolution imaging with the ILT and describe the LOFAR-VLBI pipeline we have developed, which is publicly available. We demonstrate the calibration strategy and performance of the pipeline on P205+55. We estimate that we should be able to image about 900 sources per LOFAR Two Meter Sky Survey pointing, which will allow the imaging of ~ 3 million sources in the northern sky over the next few years. I contributed to this work with astrometry and cross-referencing with other telescope catalogs, such as the **G**iant **M**etrewave **R**adio **T**elescope (GMRT). I was also part of the group that extensively tested the pipeline, identifying and fixing bugs throughout the process. My work also included cross-checking the image output using different strategies and software, and working on early containerisation using Docker before we moved everything to Singularity containers.

Harwood et al. (2022): **The resolved jet of 3C 273 at 150 MHz. Sub-arcsecond imaging with the LOFAR international baselines**
In this paper we have used the LOFAR international baselines to obtain for the first time high quality images of complex sources at low declination. We analysed the main structures of 3C 273 and found evidence for absorption in the observed emission. We also determined the kinetic power of the jet and derived lower bounds for its bulk velocity and Lorentz factor. In addition, the study placed a limit on the peak brightness of the counterjet. In this work, I mainly contributed to debugging the LOFAR-VLBI pipeline (presented in Morabito et al. 2021), which was the main data processing tool, and ultimately helped to realize the conclusions of this study.

Kappes et al. (2019): **LOFAR measures the hotspot advance speed of the high-redshift blazar S5 0836+710**
In this paper we have shown that observations of blazars with the ILT can be used to study the ICM at cosmological distances. We found that the density of ICM around the distant blazar S5 0836+710 can be substantially higher than that found in less distant radio galaxies. However, we caution that no general statement about a systematic redshift dependence can be derived from such a single-source study. We suggest that our method can be applied to a larger number of suitable blazars to obtain statistically relevant samples of the density of the ICM as a function of redshift, complementing classical observational methods applied to radio galaxies. Our analysis highlights the potential of blazars for studies of the young Universe, although the faint components of interest may be difficult to detect at redshifts much higher than $z = 2$. As the author of this paper, I have contributed significantly to all the work done in this paper.

Burd et al. (2018): **Detecting radio frequency interference in radio-antenna arrays with the recurrent neural network algorithm**
In this paper we have implemented a **R**ecurrent **N**euronal **N**etwork (RNN) with **L**ong **S**hort-**T**erm **M**emory (LSTM) cells to automatically detect RFI in interferometric radio telescope data obtained with the GMRT at 610 MHz. We used a discrete model to distinguish RFI from non-RFI data and evaluated the performance of the RNN with a confusion matrix. The true positive and true negative rates of the network were high, but the overall efficiency was low due to a large amount of non-RFI data being classified as contaminated by RFI. We found that the Matthews correlation coefficient suggested that a more refined training model was needed. In this paper, I double-checked the presented probability calculations, leading to the central final statements in this work.

Kadler et al. (2016): **Coincidence of a high-fluence blazar outburst with a PeV-energy neutrino event**
In this paper we report the discovery of a large outburst from the blazar PKS B1424-418 in time and position coincidence with the third PeV-energy neutrino event detected by IceCube. We analyse the complete sample of gamma-ray blazars in the field and show that the long-term average gamma-ray emission of blazars as a class is consistent with both the measured all-sky flux of PeV neutrinos and the spectral slope of the IceCube signal. Our results suggest a direct physical link between the outburst of PKS B1424-418 and the observed PeV event. My previous work on quantifying measurement uncertainties in **T**racking **A**ctive Galactic **N**uclei with **A**ustral **M**illiarcsecond

Interferometry (TANAMI) VLBI experiments was helpful in interpreting the radio data used. I was also part of the TANAMI collaboration at the time.

Collaboration et al. (2015): **ANTARES constrains a blazar origin of two IceCube PeV neutrino events**
In this study we aimed to test the hypothesis that the first two PeV neutrino events observed by IceCube are of blazar origin. We used six years of **A**stronomy with a **N**eutrino **T**elescope and **A**byss environmental **RES**earch (ANTARES) data to perform a candidate list search for an excess muon neutrino flux from six suggested blazars. The study did not confirm or rule out a blazar origin for the events, but it did place constraints on the range of source spectra that could have produced them. Maximum likelihood analysis found two ANTARES events that were more signal-like than background, but the result was within the expected background fluctuations. Finally, we suggest that TANAMI candidate blazars should be included in all future analyses. My previous work on quantifying measurement uncertainties in TANAMI VLBI experiments was helpful in interpreting the radio data used. I was also part of the TANAMI collaboration at the time.

Krauß et al. (2014): **TANAMI blazars in the IceCube PeV-neutrino fields**
We conducted a study focusing on six blazars from the TANAMI sample and estimated the expected number of electron neutrino events from these sources using theoretical predictions. Our results showed that the predicted number of events was very close to the actual number of events observed, indicating that the six TANAMI sources alone could explain the observed PeV neutrino flux. We also identified three TANAMI blazars in the E14 field as the most promising candidate sources, with the highest predicted neutrino rates. We found that the low flux neutrino detection statistics followed a Poisson distribution, and the predicted neutrino fluence was well within the Poisson uncertainty bounds. My previous work on quantifying measurement uncertainties in TANAMI VLBI experiments was helpful in interpreting the radio data used. I was also part of the TANAMI collaboration at the time.

6.2 List of Acronyms

AGN **A**ctive **G**alactic **N**uclei. I, III, IV, 1–10, 97, 98, 106, 113, 114, 122, 124

AIPS **A**stronomical **I**mage **P**rocessing **S**ystem; Greisen 2003. 101

ANTARES **A**stronomy with a **N**eutrino **T**elescope and **A**byss environmental **RES**earch. 150

ASTRON **ASTR**onomisch **O**nderzoek in **N**ederland. 74

BL Lac **BL Lac**ertae. 5, 6, 113

BLR **B**road **L**ine **R**egion. 12, 15

BLRG **B**road **L**ine **R**adio **G**alaxies. 6, 7

CASA **C**ommon **A**stronomy **S**oftware **A**pplication; McMullin et al. 2007; Jaeger 2008. 86, 95

CMB **C**osmic **M**icrowave **B**ackground. II, 10, 11, 13–15, 113–115, 121–124, 126, 128, 132

COBALT **CO**rrelator and **B**eamforming **A**pplication platform for the **L**ofar **T**elescope; ASTRON 2017. 100

CXC **C**handra **X**-ray **C**enter. 3

DDE **D**irection **D**ependent **E**ffect. 85, 89

DOI **D**irection **O**f **I**nterest. 93–95

DPPP **D**efault **P**ost **P**rocessing **P**ipeline; van Diepen et al. 2018. 92, 93

dTEC **d**ifferential **T**otal **E**lectron **C**ontent. 92, 93, 95

EM **E**lectro**M**agnetic. 10, 75

EVN **E**uropean **V**LBI **N**etwork. 99, 100

FOV **F**ield **O**f **V**iew. 85, 91–93, 101, 102

FR-I **F**anaroff-**R**iley Class I. 4–7, 122

FR-II **F**anaroff-**R**iley Class II. I, III, 4–7, 98, 104, 105, 107–111, 113, 120–122, 124, 132

FSRQ **F**lat **S**pectrum **R**adio **Q**uasar. I, III, 5, 6, 98, 121, 122

GMRT **G**iant **M**etrewave **R**adio **T**elescope. 148, 149

GPS **G**lobal **P**ositioning **S**ystem. 80, 89

HBA **H**igh **B**and **A**ntenna. 71, 72, 74–76, 78, 85, 97, 100, 115, 135

HPBW **H**alf **P**ower **B**eam **W**idth. 28, 61

IC **I**nverse **C**ompton. 10, 12–14, 115, 122, 128

ICM **I**ntra**C**luster **M**edium. 97, 104, 111–113, 149

IGM **I**nter **G**alactic **M**edium. 98, 102

ILT **I**nternational **L**OFAR **T**elescope. I–IV, 1, 2, 4, 11, 73–77, 79, 82–88, 97, 98, 100–103, 112, 114, 115, 117–119, 132, 134–136, 147–149

IR **I**nfra-**R**ed. 122

KH **K**elvin-**H**elmholtz. 99, 111

LAT **L**arge **A**rea **T**elescope. 123

LBA **L**ow **B**and **A**ntenna. 74–77, 85, 135

LBCS **L**ong **B**aseline **C**alibrator **S**urvey; Jackson et al. 2016, 2022. 86, 90, 94, 95

LHC **L**arge **H**adron **C**ollider. 82

LOFAR **LO**w-**F**requency **AR**ray. I–IV

LOFAR **LO**w-**F**requency **AR**ray. 1

LOFAR **LO**w-**F**requency **AR**ray; van Haarlem et al. 2013. 14, 71, 72, 74, 76, 77, 85–87, 93, 95, 97, 99, 109, 112, 113, 118–120, 125, 135, 147, 148

LoSoTo **Lo**far **So**ftware **To**ol; de Gasperin et al. 2019. 92

LoTSS **Lo**far **T**wo-metre **S**ky **S**urvey; Shimwell et al. 2017. 87, 89, 90

LSTM **L**ong **S**hort-**T**erm **M**emory. 149

LTA **L**ong **T**erm **A**rchive. 87, 116

MERLIN **M**ulti-**E**lement **R**adio **L**inked **I**nterferometer **N**etwork; Thomasson 1986. 99, 100, 103

MHD **M**agneto**H**ydro**D**ynamics. 110

MWA **M**urchison **W**idefield **A**rray; Wayth et al. 2015. 79

NASA **N**ational **A**eronautics and **S**pace **A**dministration. 3

NLRG **N**arrow **L**ine **R**adio **G**alaxies. 6, 7

PVC **P**oly**V**inyl**C**hlorid. 75

QSO **Q**uasi **S**tellar **O**bject. 4, 6

RCU **R**e**C**eiver **U**nit. 75

RFI **R**adio **F**requency **I**nterference. 81, 85, 87, 101, 116, 149

RMS **R**oot **M**ean **S**quare. 115, 119, 121

RNN **R**ecurrent **N**euronal **N**etwork. 149

SDSS **S**loan **D**igital **S**ky **S**urvey. 4

SED **S**pectral **E**nergy **D**istribution. 10, 12, 14, 122, 125, 126, 128–131, 136, 147

SKA **S**quare **K**ilometre **A**rray. II, IV, V, 79, 82, 84, 113, 136

SMBH **S**uper-**M**assive **B**lack **H**ole. 1–4, 8

SNR **S**ignal to **N**oise **R**atio. 91, 92

SSC **S**ynchrotron **S**elf-**C**ompton. 12, 13, 123, 124, 128

TANAMI **T**racking **A**ctive Galactic **N**uclei with **A**ustral **M**illiarcsecond **I**nterferometry. 149, 150

TEC **T**otal **E**lectron **C**ontent. 80, 88, 89, 92, 93

TGSS **T**IFR **G**MRT **S**ky **S**urvey. 89

UV **U**ltra **V**iolet. 54, 80, 122

VLA Karl G. Jansky **V**ery **L**arge **A**rray. II, IV

VLA Karl G. Jansky **V**ery **L**arge **A**rray; Thompson et al. 1980. 4, 5, 98, 99, 115, 116, 118–120, 132, 147

VLBI **V**ery **L**ong **B**aseline **I**nterferometry. I–IV

VLBI **V**ery **L**ong **B**aseline **I**nterferometry; Readhead & Wilkinson 1978. 6, 101, 102, 109, 111, 112, 116, 135, 147, 148, 150

6.3 Acknowledgements/Danksagung

In the academic journey, where caffeine flows like a mighty river and sleep is all too often a distant myth, it's time to shine the spotlight on the real heroes of this grand journey - in the Acknowledgements section. Much like the sidekicks in a superhero movie, these are the people whose endless support, sometimes questionable humour (and perhaps a few too many fast food deliveries) have kept this thesis going. So grab your popcorn and prepare to meet the cast of characters who have turned this rollercoaster of a PhD into a comedy of errors, lessons learned and, ultimately, a grand achievement.

First of all, I would like to express my deepest gratitude to my supervisor, Matthias Kadler: for your respectful guidance while allowing me to make my own decisions, for the invaluable insights you have given me while always being happy to discuss (also opposing) ideas, and for your unwavering support throughout my academic career. Thanks to your dedication to helping me navigate the academic waters, I have been able to visit places, interact with colleagues and continue to push my own boundaries, without losing sight of the final goal.
To this day, I remember the very first astrophysics course I took at university, which was taught by you. Although I had chosen to study physics, and astronomy in particular, out of sheer curiosity, attending your lecture made me realize from the very start that this was the area of research I was truly passionate about. This very passion, I will continue embracing and sharing with others.

I would like to express my sincere thanks to Karl Mannheim, Chair of Astronomy at the University of Würzburg. Our many engaging discussions on a wide range of topics are of great value to me. Among the many fond memories of my time in Würzburg, I'll miss these discussions very much. Your passion for engaging people from all backgrounds - colleagues, university and school students as well as the general public - has inspired me to share my own passion in a similar way. I'm deeply grateful for the foundations you've laid to enable remarkable projects to take shape, not just through resources, but through your personal involvement and ongoing support. All of which I could be a part of. Your role as mentor and guide has been marked by kindness, respect and a genuine goodwill for which I'm truly grateful.

I would now like to turn the spotlight on my exceptional office mates, Paul Ray Burd and Jonas Trüstedt, who deserve a resounding tribute. You two have been at the heart of both the challenges and the triumphs. Our shared experiences, whether

in times of difficulty or moments of success, have bound us together in a unique camaraderie. Not only have you supported my work, but you have also supported me personally, which I have always been able to rely on. You have generously shared your knowledge, enriched me with your experiences and, most importantly, blossomed a friendship. Sharing our workspace has been an immense joy and I couldn't have asked for better companions to navigate these waters. Here's to the memories we've made!

I am very grateful to Manel Perucho for his outstanding role in helping to shape my research progress. Your insights, discussions and constructive feedback have greatly enriched our exploration of extragalactic jets. The success of our work highlights the harmonious blend of observational and theoretical astrophysics. In addition to your professional excellence, I appreciate your kindness and understanding nature. Working with you has been both productive and enjoyable, whether immersed in research or relaxing with colleagues at the Main.

I wish to extend my heartfelt tribute to my esteemed colleagues at the Chair of Astronomy. Your unwavering camaraderie, engaging discourse, and shared dedication to explore the universe have been nothing short of invaluable during my time among you. Our collective endeavors have not only enriched my research but have also contributed to develop a dynamic and supportive academic environment, for which I am profoundly thankful to have been a part of. From the very beginning, you embraced me as a full-fledged member, encompassing me in both social gatherings and professional responsibilities. This inclusive approach fostered an environment in which I truly found my place. While the list of names that I've encountered over the years is extensive, I refrain from enumerating them individually; however, please know that this tribute is directed to each and every one of you who has shared this remarkable journey.

To my esteemed university commerades, I must give a hearty shout-out for the wild camaraderie and shared escapades that made our academic journey a thrilling rollercoaster ride. A special nod goes to Josh, Laura, Manuel, Mingo, Nina, Schorsch and Tobi - our dynamic crew who dealt with every exercise sheet the university threw at us. As we danced along deadlines and wrestled with equations, I always took comfort in the fact that I wasn't alone in this intellectual rodeo. Whether it was a helping hand or just a sympathetic "I'm drowning too" look, you made every challenge feel like a shared conquest. Now for the alphabetical acknowledgements, because even gratitude can use a little organisation: Jonas, Laura, Manuel, Mingo, Nina, Nora,

Paul, Rosamunde, Schorsch, Sebbo, Simon and Tobi - you wonderful wanderers of the academic realm brought joy to even the dullest of tasks. From those heart-pounding exams to those "oh no" moments in the lab, your boundless enthusiasm was the spice that made this academic stew truly palatable. So, a big hug to all of you for turning this lump of time into a rollicking adventure, complete with plot twists and lots of laughs, spiced up with very, very spontaneous road trips with Sebbo.

I would like to express my sincere gratitude to the extraordinary members of the LOFAR Long-Baseline Group, whose diligent efforts in developing the long baseline pipeline and providing invaluable assistance in data reduction have been critical to the progress of my research. Special thanks go to Leah and Neal for their outstanding leadership in guiding the group to remarkable success over the years. To the entire group, your unwavering support and expertise have not only contributed to the success of my work, but have also enriched the broader scientific community's understanding of our field and provided access to the necessary tools. It has been an honor to be a member in this group and work with all of you.

Bedanken möchte ich mich von ganzem Herzen bei meinen lieben Eltern, meiner Mutter Alwina und meinem Vater Waldemar, sowie meinen beiden Brüdern Eugen und Andreas. Eure bedingungslose Unterstützung, euer Glaube an mich und eure Liebe haben mir stets den Rücken gestärkt und mir erlaubt mich auf mein Studium und meine Entwicklung zu fokussieren. Eure stetige Ermutigung und stolze Unterstützung waren ein ständiger Antrieb. Eure Werte und eure Nähe waren der Grundstein meiner Erziehung und Entwicklung, und ich bin zutiefst dankbar für jedes Opfer und jede freudige Erinnerung, die unseren gemeinsamen Weg geprägt haben. Eure Unterstützung ist der wahre Schatz, den ich in mir trage und der mich immer begleiten wird.

To my cherished friends, I want to extend my heartfelt gratitude. Your friendship has been a precious gift that has enriched my life's journey in countless ways. Your uplifting words, encouraging actions, and constant presence have illuminated the highs and softened the lows of this expedition. Through our shared adventures, laughter, and heartfelt conversations, you've been a steadfast source of joy, support, and camaraderie. Your unwavering companionship, and the memories we've crafted together have been the pillars of strength that have guided me through challenges and celebrated triumphs. Thank you for being the incredible friends that you are, and for filling my life with warmth, positivity, and unforgettable moments.

A big thanks to my proofreading pals, Chris and Etienne! Your sharp eyes and word-wrangling wizardry have transformed my writing into a work of art. You've caught typos and rescued syntax, turning chaos into clarity. Your meticulous efforts have added that extra sparkle to my words. Cheers for making my work shine!

Lastly, a resounding shout-out to Muse for the cosmic resonance they brought into my research journey with "Supermassive Black Hole" (Muse 2006).

As this phase of my journey draws to a close, I'm compelled to express my heartfelt gratitude to my supervisor, colleagues, peers, friends, and family. Each of you has contributed a vital note to this symphony of achievements. The combined influence of everyone I've encountered along this path has not only shaped my professional growth but has also significantly contributed to the person I've become. Your support has been instrumental in helping me reach ambitious goals, nurturing my growth as a friend, colleague, sibling, and son. Looking ahead, I'm excited about the prospect of composing the next chapters not only in my own journey but also in yours, with the same sense of wonder, excitement and accomplishment.